JAEA-Research
2007-052

Studies on Representative Disruption Scenarios, Associated Electromagnetic and Heat Loads and Operation Window in ITER

Hirobumi FUJIEDA, Masayoshi SUGIHARA*, Michiya SHIMADA
Yuri GRIBOV*, Kimihiro IOKI*, Yasunori KAWANO, Rustan KHAYRUTDINOV*
Victor LUKASH*, Junji OHMORI and Yuzuru NEYATANI

ITER Diagnostics Group
Fusion Research and Development Directorate

July 2007
Japan Atomic Energy Agency
日本原子力研究開発機構

JAEA-Research

〒319-1195　茨城県那珂郡東海村白方白根 2 番地 4
日本原子力研究開発機構　研究技術情報部　研究技術情報課
電話 029-282-6387, Fax 029-282-5920

*〒319-1195　茨城県那珂郡東海村白方白根 2 番地 4　日本原子力研究開発機構内

JAEA-Research 2007-052

Studies on Representative Disruption Scenarios, Associated Electromagnetic and Heat Loads and Operation Window in ITER

Hirobumi FUJIEDA※, Masayoshi SUGIHARA[*1], Michiya SHIMADA,
Yuri GRIBOV[*1], Kimihiro IOKI[*1], Yasunori KAWANO, Rustan KHAYRUTDINOV[*2],
Victor LUKASH[*3], Junji OHMORI and Yuzuru NEYATANI

ITER Project Unit
Fusion Research and Development Directorate
Japan Atomic Energy Agency
Naka-shi, Ibaraki-ken

(Received April 20, 2007)

The impacts of plasma disruptions on ITER have been investigated in detail to confirm the robustness of the design of the machine to the potential consequential loads. The loads include both electromagnetic (EM) and heat loads on the in-vessel components and the vacuum vessel (VV). Several representative disruption scenarios are specified based on newly derived physics guidelines for the shortest current quench time as well as the maximum product of halo current fraction and toroidal peaking factor arising from disruptions in ITER. Disruption simulations with the DINA code and EM load analyses with a 3D finite element method (FEM) code are performed for these scenarios. Some margins are confirmed in the EM load on in-vessel components due to induced eddy and halo currents for these representative scenarios. However, the margins are not very large. The heat load on various parts of the first wall due to the vertical movement and the thermal quench (TQ) is calculated with a 2D heat conduction code based on the database of heat deposition during disruptions and simulation results with the DINA code. It is found that the beryllium (*Be*) wall will not melt during the vertical movement. Significant melting is anticipated for the upper *Be* wall and tungsten divertor baffle due to the TQ after the vertical movement. However, its impact could be substantially mitigated by implementing a reliable detection system of the vertical movement and a mitigation system, e.g., massive noble gas injection (MGI). Some melting of the upper *Be* wall is anticipated at major disruptions (MD). At least several tens of unmitigated disruptions must be considered even if an advanced prediction/mitigation system is implemented. With these unmitigated disruptions, the loss of *Be* layer is expected to be within ≈ *30-100 μm*/event out of *10 mm* thick *Be* first wall. Various post processing programs of the results simulated with the DINA code, which are developed for the design work, are explained in the appendix.

Keywords: Disruption, Current Quench, Electromagnetic Load, Thermal Load, Mitigation, Tokamak, ITER

※ *Research Staff on Loan*
[*1] *ITER Organization, Cadarache JWS, France*
[*2] *TRINITI, Russian Federation*
[*3] *Kurchatov Institute, Russian Federation*

ITERの代表的ディスラプションシナリオ、付随する電磁力と熱負荷および運転領域に関する研究

日本原子力研究開発機構
核融合研究開発部門　ITERプロジェクトユニット
藤枝　浩文※、杉原　正芳*1、嶋田　道也、
Yuri GRIBOV*1、伊尾木　公裕*1、河野　康則、Rustan KHAYRUTDINOV*2、
Victor LUKASH*3、大森　順次、閨谷　譲

（2007年4月20日受理）

ITERがプラズマディスラプションに対して堅牢に設計されていることを確認するために、ディスラプション時に炉内構造物や真空容器に働く電磁力や熱負荷などの影響を調べた。最短電流クエンチ時間やハロー電流のトロイダルピーキングなどに関する最新の物理ガイドラインに基づき、DINAコードによるシミュレーションにより、幾つかの代表的ディスラプションシナリオを設定した。これらのシナリオに対して、3次元有限要素法により電磁力評価を行った。その結果、炉内構造物の電磁力は許容範囲にあることが確認されたが、しかしそのマージンはそれほど大きくない。次に垂直位置移動現象（VDE）時や熱クエンチ時の炉内構造物の各部への熱負荷を実験データベースおよびDINAコードによるシミュレーションにより求めた。更に、この結果に基づき2次元熱伝導コードを用いてベリリウム第一壁およびタングステンダイバータバッフルの侵食量（溶融量および蒸発量）を求めた。この結果、VDE発生時の侵食量は小さく、熱クエンチ時の侵食量は上方VDE発生時で≈170 μm/event（Be）、下方VDE発生時で≈240 μm/event（W）となり相当に大きいことがわかった。ITERでは、これらVDEは移動時間に0.5秒程度を要するため、その間に大量ガス注入（MGI）などの影響緩和手段を講じることが十分に期待できる。一方、中心位置ディスラプション（MD）では、ディスラプション発生予測と緩和に失敗する確率をゼロにすることができないため、上部ベリリウム第一壁の侵食は大きな問題となる可能性がある。この場合は≈(30-100)　μm/eventの侵食量となり、MDの発生予測・緩和の失敗回数を数十回程度に抑える必要がある。

最後にDINAコードの結果を設計に使いやすくするために開発した種々の後処理プログラムの使用方法をアペンディックスにまとめた。

那珂核融合研究所（駐在）：　〒311-0193　茨城県那珂市向山　801-1
※　*出向職員*
*1 *ITER Organization, Cadarache JWS, France*
*2 *TRINITI, Russian Federation*
*3 *Kurchatov Institute, Russian Federation*

Contents

目　次

1. Introduction

Detailed examinations of EM and heat loads under various disruption conditions expected in ITER are essential to check the robustness of the design against the potential consequential loads. Robustness of the VV and large in-vessel components, such as the blanket modules (BM) and divertor cassette, are particularly important since they are directly linked with the protection of the machine against mechanical damage. Robustness for the heat load during the TQ and vertical displacement event (VDEs), which may cause a possible damage of the plasma facing components (PFCs), is another important point.

Some margin against both loads must be reserved for the representative scenarios. In particular, a reasonable margin against the mechanical stress is of primary importance for the protection of the machine. This requirement is stressed, since, even if any disruption prediction/mitigation system is implemented, the system cannot be expected to be 100% reliable and some disruptions will unavoidably occur. On the other hand, the heat load on PFCs mainly affects its lifetime and the prediction/mitigation system will be very effective for prolonging its lifetime by reducing the damage of the PFCs due to the thermal load during the TQ and VDEs. Nevertheless, it is also essential to reserve a reasonable duty cycle by avoiding frequent replacement of PFCs.

In order to check the robustness, a proper specification of representative disruption scenarios based on detailed assessment of the database is essential, since such loads strongly depend on the detailed plasma behaviour [1]. Of particular importance for the assessment of EM loads on the in-vessel components is the shortest current quench time [2, 3], and the maximum product of halo current fraction ($I_{h,max}/I_{p0}$) and toroidal peaking factor (TPF), $f_h \equiv (I_{h,max}/I_{p0}) \times TPF$ [4-8]. As for the VV, the EM load induced by the halo current is important, and, thus, disruptions with largest halo current, which are generated during downward VDEs with slow current quench, must be examined. Details of the plasma behaviour are also important in order to evaluate the effect of the heat load on PFCs due to the TQ and plasma contact with the PFCs during VDEs. To these plasmas, it is necessary to properly apply the database on the thermal energy content at the TQ, the energy deposition width and time duration during the TQ, though it is still limited [9-12].

Recent progress of the disruption prediction/mitigation systems is remarkable. It is important to examine how the robustness of ITER is improved with implementing the most advanced system so far developed. Among the mitigation techniques so far proposed, the

MGI technique seems to be the most promising [13-16]. This technique provides a sound basis for the mitigation of the damage due to heat loads. It is important to assess the mitigation success or missed rate in ITER with this technique, since the effectiveness of such a mitigation system strongly depends on the disruption prediction. Here, mitigation success rates are defined as the ratio of the number of disruptive discharges which are successfully mitigated to the total number of disruptive discharges. This assessment can be performed by using sophisticated disruption prediction methods recently developed, such as a neural network system [17-23], applied to the possible mitigation scenarios. The success rate strongly depends on the response time, which is closely linked to the propagation time of the gas through the gas-inlet pipe with its sound speed, and the plasma response time before the occurrence of the radiation collapse after the gas reaching to the plasma edge.

In this paper, we first simulate representative disruption scenarios (both downward and upward VDEs and MDs) with the disruption simulation code DINA based on the recently derived guideline for the shortest current quench time. As for downward VDEs, two representative cases of safety factor q are simulated (i.e., $q=1.5$ and ≈ 2.8), since magnitude of the induced halo current differs significantly for different values of q value (larger poloidal halo current for lower q value). We then evaluate the EM load on BMs and VV due to the induced eddy and halo currents using the 3D FEM code and the maximum f_h expected in ITER from database analyses. Among the in-vessel components, BMs are examined, since, compared with divertor cassette, they are larger in size (larger induced eddy current) and support of the module is comparatively difficult. The heat loads on various parts of the BMs and divertor during VDEs and the TQ are evaluated for these scenarios. Erosion thickness of each PFC is calculated for these cases with a 2D heat conduction code. A neural network prediction technique coupled with the mitigation system by MGI is applied to assess the resulting lifetime of the first wall based on the expected mitigation success rate of the neural network system. We will also identify further physics research needs to improve the assessment of the impacts of disruptions and the performance of the prediction/mitigation system for each area.

In Sec. 2, representative disruption scenarios calculated with the DINA code are presented. In Sec. 3, EM loads on BMs and the VV calculated with the 3D FEM code are presented. In Sec. 4, Heat loads on various parts of PFCs are evaluated for these disruption scenarios. Resulting erosion of PFCs calculated with the 2D heat conduction code is presented. In Sec. 5, possible reduction of erosion by disruption prediction and mitigation systems is examined. In Sec. 6, conclusions are drawn.

2. Representative Disruption Scenarios

The origin of the most critical EM load is different for different components. For the VV, the vertical force due to the induced halo current is the most critical. VDEs with a slow current quench, where the halo current is expected to be the largest, are of major concern for the VV. As for the BMs, the EM load due to the induced eddy current is dominant, while the halo current also contributes to some extent. Thus, the MDs and VDEs with the fastest current quench are the most important for BMs. In this way, the guidelines for the fastest current quench and the halo current are most important for the evaluation of EM loads on BMs and VV.

Since the previous International Disruption Database (IDD) prepared for the ITER physics basis (IPB) [1], a new IDD has been initiated with a particular emphasis on the fastest current quench for each machine [2, 3]. In contrast to the previous evaluation, the quench time Δt is evaluated from the average quench rate between *80%* and *20%* of the initial plasma current I_{p0} for all machines. From this database, it is recommended to use $1\ ms/m^2$ as the guideline for the fastest current quench time normalized by the poloidal cross-section area ($\Delta t/S$) for *60 %* current quench [3]. This corresponds to the full current quench (*100-0*%) time of *36* ms for ITER when a linear waveform is assumed as the simplest choice. It is difficult to specify a particular waveform in ITER, since the underlying physics to determine the waveform has not been well identified. Detailed examinations of the waveform performed for the fastest current quench disruptions in JET and JT-60U show that the waveform can be well fitted by an exponential curve in many of the disruptions with the shortest quench time [28-30]. Enhancement of the generation of runaway electrons due to large electric field induced by fast current quench is considered to be the main mechanism for this waveform [29, 30]. Thus, for the purpose of the EM load analysis, we also employ the exponential waveform of the current quench as in our previous papers [31, 32]. Namely, we use the exponential curve, which passes through *80%* and *20%* of I_{p0} for the shortest linear waveform expected in ITER. This provides a time constant of $\tau \approx 16\ ms$ in ITER. Fortunately, as shown later, EM loads on BMs are more or less similar for both linear and exponential waveforms. However, examinations of the exponential waveform are especially important for smaller components such as the ICRF antenna and the first wall with time constants shorter than that of BMs. These analyses are not discussed in this paper, since we will concentrate on relatively large components, which are critical for the protection of the machine.

Experimental data for *TPF* as a function of maximum poloidal halo current fraction $I_{h,max}/I_{p0}$ were summarized in IPB [1]. Data have been updated with addition of further experimental data from MAST, JET and JT-60U [6-8]. This database indicates that the maximum $f_h \approx 0.7$. A large poloidal halo current is driven when the plasma current decays slowly, since the edge safety factor reduces significantly under this condition. In the ITER application, the maximum $I_{h,max}/I_{p0}$ is evaluated to be ≈ 0.44 in downward VDE (toward the X-point) with a slow current quench with a simulation code, as shown later. Then, the *TPF* is evaluated as $0.7/(I_{h,max}/I_{p0}) = 1.6$. This *TPF* ($\approx 1.6$) is also applied to MDs and VDEs with fast current quench. The halo current with this TPF contributes to the total EM load on BMs to some extent. Smaller f_h than 0.7 when current quench becomes faster has been indicated in JET experiments [8, 33]. More systematic investigation of this tendency in the existing machines is fairly important for the accurate assessment of EM load.

Based on these guidelines, several representative disruption scenarios have been prepared for the EM load analyses. They include MDs with fast current quench, upward and downward VDEs with fast and slow current quenches. Numerical simulations are performed with the DINA code [34] for these representative scenarios to simulate detailed plasma behaviors during disruptions. The DINA code solves the evolution of 2D plasma equilibrium on closed and open magnetic surfaces together with external circuits (PF coils and surrounding conducting structures). The PF coils are short-circuited and the vacuum vessel is modelled by small sized passive toroidal conductors. Each toroidal row of BMs is modelled by two pairs of toroidally connected plates (inside/outside, top/bottom). They are also connected poloidally with each other at one toroidal location to form a twin-loop, so that the net toroidal current is forced to be zero. Divertor modules are not modelled in the calculation. Details of ITER modelling with the DINA code are described in [31]. Major assumptions for the simulations are summarized in Table 1. Initial plasma equilibrium configuration before VDEs and MDs is taken from the reference inductive scenario ($\beta_p=0.7$, $\ell_i=0.85$ and $I_p=15$ MA with $q_{95}=3$, $\kappa_{95}=1.7$, $\delta_{95}=0.33$).

Figure 1.1 (a) shows time evolutions of the plasma current, the vertical position and the poloidal halo current for a downward VDE for the linear quench waveform with *36 ms* current quench time. Figure 1.1 (b) shows four time slices of Last Closed Flux Surface

(LCFS; bold line) and halo boundaries (thin line) for this case at (a), (b), (c) and (d) in Fig. 1.1 (a). Figure 1.2 (a) and (b) show the case of downward VDE for the exponential quench waveform with a time constant of *16 ms*. A small downward kick is provided at $t = 0$ and the vertical position control is turned off at that point. The plasma moves downward and a TQ occurs when the vertical position of the current centre reaches $\approx$*-1 m* at $t = 645$ *ms*. The surface q value at the occurrence of the TQ is assumed to be *1.5,* since this q value is expected to be minimum based on the database analysis in JT-60U [35]. The poloidal halo current is expected to be the largest when the TQ occurs at the possible minimum q value. Figure 1.3 (a) and (b) show the case of upward VDE for the linear quench waveform with *36 ms* current quench time. Figures 1.4 (a) and (b) show the case of upward VDE for the exponential quench waveform with a time constant of *16 ms*. A small upward kick is provided at $t = 0$ and a TQ occurs when the vertical position of the current center reaches +*2 m* (surface q value reaches *1.5*) at $t = 870$ *ms*. Figure 1.5 (a) and (b) show the case of MDs for the linear quench waveform with *36 ms* current quench time. Figures 1.6 (a) and (b) show the case of MDs for the exponential quench waveform with a time constant of *16 ms*. In this case, a TQ is triggered at $t = 7$ *ms* when the plasma stays at the initial vertical position (Z=*0.5 m*). For the present specification of fast current quench and moderate change of internal inductance ℓ_i during the TQ, the plasma moves upward after the TQ. An initial Z position of *0.5 m* has been specified to realize the upward movement of plasma after the TQ for the majority of the MD cases, since the induced halo current is smaller in the upward movement than in the downward movement. For larger change of ℓ_i and/or slower current quench, however, the plasma can move downward after the TQ, which has been investigated in detail in Ref. [36]. Next, downward VDEs, in which the TQ occurs at larger q value (q=*2.86*), are simulated. Figure 1.7 (a) and (b) show the case of downward VDE for the linear quench waveform with *36 ms* current quench time. Figure 1.8 (a) and (b) show the case of downward VDE with a time constant of *16 ms*. In these downward VDEs scenarios, the maximum halo current is $\approx$*60 %* of the VDE scenarios shown in Fig. 1.1.

It is naturally expected that the induced halo current is larger for downward VDE than upward VDE due to larger destabilizing force of the vertical instability for the former than the latter. This feature originates from the asymmetry of the equilibrium magnetic field configuration, where the local radial curvature of the vertical magnetic field is larger in the lower region than the upper region of the plasma due to the existence of the X-point in the former. Thus, simulation studies have been performed for downward VDEs with various electron temperatures after the TQ, which directly determine the current quench time. Figure 1.9 shows the maximum induced poloidal halo current during downward VDEs with various current quench times. It is seen from this figure that the induced halo current increases as the current quench time increases and it tends to saturate, and its maximum value is $\approx 6.4MA$. Figure 1.10 (a) shows time evolutions of the plasma current, the vertical position and the poloidal halo current for this case (maximum halo current $\approx 6.4MA$). Figure 1.10 (b) shows four time slices of Last Closed Flux Surface (LCFS; bold line) and halo boundaries (thin line) for this case at (a), (b), (c) and (d) in Fig. 1.10 (a).

Finally poloidal magnetic energies inside the plasma (solid line) as well as inside the VV (dashed line including plasma) before the TQ are shown in Fig. 1.11 for MD case. These energies are converted into the radiation energy on the first wall via joule heating process during the current quench phase, and thus are important to assess the energy load on the first wall during this phase. Note that part of the magnetic energy inside the VV is dissipated within the in-vessel components. Melting of *Be* will not occur even if whole of the poloidal magnetic energy inside the VV is converted into radiation energy, whereas thermal fatigue needs to be assessed. Sudden drop of the magnetic energy at the moment of the current flattening (ℓ_i drop) during the TQ might attribute to the employed model of the TQ in the DINA code, and thus might be unphysical.

3. EM Load due to Induced Eddy and Halo Currents

3.1 EM Load on Blanket Module

Induced eddy currents on the surrounding structures are calculated with the 3D finite element method (FEM) code using the time behaviour of the toroidal current density of the plasma column including halo region evaluated with the DINA code. EM load analyses have been performed using these induced eddy currents. The BMs are connected to the VV through key structures and flexible supports. Supporting structures of a typical BM are shown in Fig. 2.1. The key structure restrains the displacement of the module parallel to the VV wall, reacting to the poloidal and toroidal forces originating from the radial moment (*Mr*) generated by the coupling of the induced eddy current j_r in radial direction with the toroidal magnetic field B_t (see Fig. 2.2). The flexible support reacts to the loads in the radial direction originating from the poloidal and toroidal moment (*Mp, Mt*) generated by the coupling of the induced eddy current in poloidal direction j_p with B_t and in toroidal direction j_t with the poloidal magnetic field B_p while being compliant in the other directions. Consequently, vertical (poloidal) forces (*Fp*) both due to eddy and halo currents are superimposed on the key. Actually, this force is the most difficult to resist because of space limitation at the key structure. Thus, in this paper, we will discuss the EM load on the key structure for various representative scenarios. For the robustness of the VV itself, the maximum value of the total vertical force due to the induced halo current is the most important. Thus, we will discuss this force using the downward VDE with slow current quench, which provides the largest halo current.

Figures 2.3 and 2.4 show the maximum poloidal (vertical) forces *Fp* due to the induced eddy and halo currents on #1-10 BMs (Fig. 2.3) and #11-18 BMs (Fig. 2.4) for representative scenarios of MDs (MD_lin and MD_exp) and upward/downward VDEs (VDE_UP_lin, VDE_UP_exp, VDE_DW_lin and VDE_DW_exp) with a fast current quench (*36 ms* quench time for the linear waveform and *16 ms* time constant for the exponential waveform), respectively. The *TPF=1.6* is used to evaluate the local maximum force due to the halo current. The time evolution of the halo current path is obtained by the DINA code calculation, and the possible maximum fraction of the halo current flowing into each BM is assumed. For instance, fraction of halo current flowing into the *No.1* blanket module f_1, $f_1 \equiv I_{halo}(No.1)/I_{halo,total}=0.5$ is assumed during the whole current quench phase to keep some margin against the uncertainty of the plasma behaviour. The numbers of BMs are shown in Figs 1.1 (b) and 1.3 (b). In Figs 2.3 and 2.4, the numbers of BMs with particularly large *Fp* are indicated. The solid line shows the allowable *Fp* due to the induced eddy current as a function of *Fp* due to the induced halo current. This includes the effect of a dynamic factor of *1.5* due to the motion of the BM at the onset of *Fp*. The dashed line shows the allowable *Fp* when the event is very rare (1-2 during the whole life), which is *20%* higher than the solid line. This is a standard ASME criterion. Note that the size of BMs in the inboard region (#1-#10) is larger than those in the outboard region (#11-#18), and thus, the size of the key structure in the former can be larger than the latter due to relaxed space limitation. For this reason, the allowable force *Fp* is larger in the former than the latter as is seen in Figs 2.3 and 2.4. However, the induced force itself is also larger in the former due to larger size as is also seen in the figures. It is seen from Figs 2.3 and 2.4 that EM loads on all BMs are within the allowable limit for the representative disruption scenarios investigated. Since the present margins are not large, further efforts to estimate the margins more credibly from the physics side and to increase the margins from the engineering side are highly desirable to further increase the robustness of the machine. Of particular importance from the physics side is further development of the models of plasma behaviours including the halo fraction, toroidal peaking factor and width of halo current region. Further developed models must be validated by the existing machines as well as by the ITER itself. For this purpose, during the hydrogen phase of ITER operation, the plasma current will be increased slowly and at each level of plasma current, assessment will be made on the disruption forces. Schemes of disruption prediction and mitigation will be also assessed. For MDs, as will be discussed later, prediction of disruption cannot be *100%* reliable, so that at least several tens of MDs must be expected to occur during the whole life of ITER operation. As for VDEs, it appears to be feasible to decrease the number of unmitigated VDEs to a few shots during the whole life of ITER by constructing a reliable position detection system and disruption mitigation system, since the plasma vertical movement is very slow during a VDE due to the long time constant of the VV in ITER. However, similar levels of EM load must be anticipated for both mitigated and unmitigated disruption according to the recent experimental studies, in which the current quench time for the mitigated disruption by the MGI is in the same range of the unmitigated disruptions with fastest current quench [14, 16]. Thus, in any case, the criterion with 20% higher allowable force by ASME cannot be applied for the EM loads. Expected numbers of mitigated and unmitigated shots by the MGI and prediction system will be discussed in Sec. 5 in more detail.

3.2 Vertical Force on Vacuum Vessel

For the evaluation of the largest total vertical force on the VV, the simulation result shown in Fig. 1.10 is used. Simulation results for the induced (toroidal eddy) currents on the VV are also used, since they also contribute to the total vertical force. Figure 2.5 shows the time evolutions of the vertical forces due to halo (dashed line) and eddy (dotted line) currents as well as the total force (solid line). Although the vertical force due to the eddy current shifts the time point at which the force reaches its maximum, the maximum force itself only slightly increases (in absolute value). The maximum total vertical force is marginally within the presently imposed design limit (*80-85 MN*).

Another important issue is a possible trade-off between fast current quench and runaway electron generation. The efficiency of runaway electron generation can be fairly high due to an avalanche effect in large tokamaks [37, 38]. In fact, disruptions in JET and JT-60U have already indicated such characteristics [39, 40]. If runaway electron generation is always associated with a fast current quench, EM loads could be substantially reduced. In this case, however, possible damage of the first wall by runaway electrons must be carefully examined. This examination is beyond the scope of this paper and will be performed elsewhere. In any case, complete exclusion of fast current quench due to the runaway generation is unrealistic, and thus proper robust design against the EM loads due to fast current quench is necessary. In addition, runaway electrons are not generated in many of the VDEs, since the induced MHD activity probably enhances the loss of runaway electrons as the edge safety factor decreases during the vertical movement [41].

3.3 Halo Current into Port

Halo current during upward VDEs on the recessed component, particularly port plug (PP) installed at #10 BM, is evaluated with the DINA code as a function of recessed distance. This evaluation is important to compromise the recessed distance and the EM load on the port plug. Both fast and slow current decay cases are analyzed. Figs 2.6 and 2.7 show the time behaviors of plasma current, vertical position of plasma current center and total poloidal halo current for these two cases, respectively.

Figure 2.8 shows the geometry of the PP. In this analysis, however, the PP simplified geometry as shown in Fig. 2.9 for simplicity. Since toroidal length of both lower and upper part of the PP are assumed *60 cm* (actual length are *60 cm* for lower and 30cm for upper part), the evaluated values of this analysis include some redundancy. Poloidal length of the PP used in the analysis is same as that of the real geometry. Figure 2.10 shows the configuration of the first wall, #10 BM and PP on the poloidal cross-section. Figure 2.11 shows the halo current path flowing to the PP. In this analysis, poloidal magnetic field on the position of the first wall is used to trace the field line beyond the first wall, for simplicity. This simplification may contain another redundancy in the evaluated halo current.

3.3.1 Halo current into PP for VDE with fast current decay

Figure 2.12 shows the time behaviors of the halo current flowing into the PP for recessed distances of *0cm* (no recess), *1 cm*, *2 cm* and *3 cm* in the case of VDEs with fast current decay. Total halo current flowing to #10 BMs (toroidally summed up including PP) is also shown. Maximum halo current flowing into PP without recess is *≈20kA* out of *≈1.3 MA* into the whole #10 BMs. When it is recessed by *3 cm*, halo current reduces down to *≈4 kA*. Left portion of Figures 2.13-2.17 show the plasma and halo boundaries at each time moment (a)-(e) shown in Fig. 2.12. Right portion of Figures 2.13-2.17 show the area, where the halo current flows into PP, at each time moment (a)-(e) for each recessed distance, *0 cm* (light gray), *1 cm* (gray), *2 cm* (dark gray) and *3 cm* (black), respectively.

3.3.2 Halo current into PP for VDE with slow current decay

Figure 2.18 shows the time behaviors of the halo current flowing into the PP for recessed distances of *0 cm* (no recess), *1 cm*, *2 cm* and *3 cm* in the case of VDEs with slow current decay. Total halo current flowing to #10 BMs (toroidally summed up including PP) is also shown. Maximum halo current flowing into PP without recess is ≈*50 kA* out of ≈*3.3 MA* into the whole #10 BMs. When it is recessed by *3 cm*, halo current reduces down to ≈*20 kA*. Since the plasma configuration (size) at the time moment of maximum halo current into PP differs from that of fast current decay case (see Figs 2.16 and 2.22), reduction of maximum halo current flowing into PP with *3 cm* recess from that without recess is smaller than in the case of fast current decay.

Left portion of Figures 2.19-2.23 show the plasma and halo boundaries at each time moment (a)-(e) shown in Fig. 2.18. Right portion of Figures 2.19-2.23 show the area, where the halo current flows into PP, at each time moment (a)-(e) for each recessed distance, *0 cm* (light gray), *1 cm* (gray), *2 cm* (dark gray) and *3 cm* (black), respectively.

3.3.3 Summary of halo current into PP

Evaluation of the halo current on the recessed component (port plug installed at #10 blanket module) with the DINA code as a function of recesses distance can be summarized as follows. Figure 2.24 shows the maximum halo current flowing into PP as a function of recessed distance for VDEs with fast (thin solid line) and slow (bold solid line) current decay, respectively. Dotted lines show the maximum halo current for the case of PP with *45 cm* toroidal length. When the port plug is recessed by *3 cm* (*0 cm*), maximum halo current is ≈*20 kA* (*50 kA*) for the upward VDE with slow current decay (*600 ms*) and ≈4 kA (*20 kA*) for fast current decay (*36 ms*).

4. Heat Load on PFC and Its Erosion during MDs and VDEs

The heat load on PFCs during MDs and VDEs can make a large impact on their lifetime. In particular, the impact on the *Be* first wall can be very large, since its melting temperature is rather low. The heat load during the TQ will be most severe both for MDs and VDEs, whereas the heat load during vertical movement of VDEs before the TQ may also be of serious concern, since hot burning plasmas directly contact the wall. In contrast, the heat load after the TQ is caused mostly by impurity radiation and, thus, it will not be localized on the wall. Thus, in the present paper, we will concentrate on the heat load before and during the TQ. Unfortunately, the database of the heat load during the TQ is still very limited. The most systematic database so far available is in [11, 12]. In this paper, we will use this database to estimate the heat load on the *Be* first wall and tungsten divertor baffle before and during the TQ for MDs and VDEs. In Table 2, major assumptions for this estimation taken from this database are summarized.

4.1 Heat Load and Erosion during Major Disruptions

In the case of MDs, the largest heat load on the *Be* first wall will be deposited on the upper wall, since half of the heat flux across the second separatrix will be deposited there. Figure 3.1 shows the flux surfaces near the upper wall from the equilibrium calculation for the case of the reference inductive scenario. In this reference equilibrium configuration, the flux surface, which is located at *56.7 mm* from the first separatrix at the outer mid-plane, barely touches the upper first wall, as shown by the dotted line in Fig. 3.1. In the figure, the flux lines of every *2 mm* beyond *40 mm* from the first separatrix are depicted and the intersecting region with the upper wall are indicated as (1)-(7). The location of the equilibrium relative to the wall is not unique and, it can be varied. The design guideline for the control system imposes that the flux surfaces below *40 mm* from the first separatrix should not intersect with the upper wall. Thus, the possible worst condition for the heat flux on the upper wall is that the flux surface *40 mm* from the first separatrix barely touches the wall. In the present evaluation, we shift the upper wall downward, for simplicity, instead of calculating the actual upward shifted equilibrium. This hypothetical wall position is also shown in Fig. 3.1 as a possible worst case. The intersecting points of these flux surfaces with the hypothetical wall are indicated as (a)-(h). Figure 3.2 shows the range of heat load density on the upper wall during the TQ of MDs for the reference (dotted line) and the possible worst (solid line) equilibrium configurations. These calculations are done by assuming *1 MJ* for the total energy loss during the TQ, so the actual energy loss W_{peak} (*MJ*) during the TQ must be multiplied to evaluate the actual value of the heat load density. The steady heat load width λss

$=5\ mm$ is assumed in the calculation. Upper and lower bounds correspond to the expansion factor of λss (5 corresponds to lower and 10 to upper). Table 3 summarizes the peak heat loads for two cases of W_{peak} ($175\ MJ$ and $350\ MJ$). The range corresponds to the expansion factors 5 to left and 10 to right. Energy deposition density divided by square root of deposition duration time ε ($MJ/m^2/\ s^{1/2}$) is conveniently used to indicate the melting or sublimation threshold of the target materials, since this parameter corresponds to the surface temperature increase. From energy deposition densities in Table 3 together with the assumption for the time duration of the heat deposition in Table 2, ε can be evaluated and is in the range of $8.2\text{-}75\ MJ/m^2/s^{1/2}$ for the deposition time duration of $1.5\text{-}3\ ms$. The criterion for melting of *Be* is $\approx 20\ MJ/m^2/s^{1/2}$ and, thus, melting of *Be* is expected in many MD cases. Calculations of two-dimensional heat conduction [42] under various energy deposition conditions have been performed and the resulting thicknesses of melt layer and vaporized layer have been evaluated. The results are shown in Fig. 3.3. From this figure, it is seen that the loss of *Be* thickness can be estimated as $\approx 30\text{-}100\ \mu m$/event for $1\text{-}2\ MJ/m^2$ (intermediate range of energy deposition density shown in Table 3) when the whole melt layer is lost. If we simply assume that all of MDs have exactly the same equilibrium and the location of energy deposition is the same, the total allowable number of MDs for the upper *Be* wall of $10\ mm$ is estimated as $100\text{-}300$. Although the equilibrium at the TQ for each discharge is not necessarily the same, this assumption may not be too stringent, since the poloidal length of the upper wall, which receives large energy loads, is rather wide, e.g., (3)-(7) in the reference wall position and (d)-(h) in the possible worst case. Therefore, substantial reduction of number of MDs (or number of localized energy deposition during the TQ in MDs) is of primary importance to avoid a frequent replacement of the upper first wall.

Energy load on the mid-plane region during the TQ is another concern, since the width of energy flow is wide. This is especially concern for the operation with ICRF heating, since the distance between plasma and antenna is small to keep the good coupling. The reference position of the first wall and limiter after retraction for the operation w/o and with ICRF heating is denoted by “FW” and “Limiter” in Fig. 3.4. These configurations are during burn before the TQ (before the movement due to beta drop). In the case with ICRF heating, $L_0=12\ cm$ is expected as the minimum distance. If the coupling is better than the assumed one, the distance could be longer than $12\ cm$.

The plasma moves inward during the TQ due to the beta drop. Fig. 3.5 shows the first separatrix surfaces just before ($7.1\ ms$) and after ($8.1\ ms$) the TQ calculated with the DINA code. The time duration of the beta drop is assumed *1 ms*. Figure 3.6 shows details of the time evolution of the radial position of the outer (R_{max}) and inner (R_{min}) separatrix surface, respectively. R_{max} moves inward by ≈*10 cm* and R_{min} moves inward by ≈*3.5 cm*. From Figs 3.5 and 3.6, the time evolution of the heat flux at the location of the first wall / limiter head (*17.5cm* and *12 cm* from the first separatrix just before the TQ) are shown in Fig. 3.7 and 3.8, respectively (beta drop starts at $t=0$). The peak heat flux (at the onset of the TQ) and total energy load density during the beta drop (*1 ms*) at the location of the first wall / limiter head located at *17.5 cm* and *12 cm* from the first separatrix just before the TQ is summarized in Tables 4 and 5, respectively. Total energy load density for various values of L_0 during energy deposition time (*1 ms*) can be obtained by integrating the heat flux (for the cases of L_0 =*17.5cm* and *12 cm* are provided in Figs 3.7 and 3.8). This is shown in Fig. 3.9.

In the actual operation of ITER, some uncertainty of the separatrix position due to uncertainties in reconstruction of the equilibrium and control system must be considered. If we assume the possible range of this uncertainty as ±*2cm*, the energy load density for the operation with ICRF heating could be larger or smaller than the case of reference location by 50% as shown in Fig. 3.9. The peak heat flux and the total energy load density at L_0 =*17.5 cm* and *12 cm* from the 1st separatrix are summarized in Tables 4 and 5, respectively.

When the limiter is retracted to the location of the first wall, the limiter surface will receive very small heat, since the surface is almost parallel to the field line. If the limiter is slightly protruded, the limiter head will receive the parallel heat flux shown in Tables 4 and 5. Even in this case, the limiter surface marginally melts only for the ICRF operation with full energy TQ and broadest energy deposition width (numbers of such disruption are limited) by careful shaping of the limiter surface (reduction of energy load density by a factor of *1/5-1/10* is assumed). Effect of toroidal field ripple and uncertainty of the separatrix position should be investigated carefully in the engineering design.

As shown in Figs 3.5 and 3.6, the inner separatrix surface also moves inward. Fig. 3.10 shows the movement of the corresponding flux surfaces at the inner region which are away from the separatrix by the specified distance in the figure at the outer mid-plane (if they are connected). When they are disconnected by the second separatrix, the movement of flux surfaces with the same Ψ_{pol} values are shown. It is seen from this figure, the movement of the flux surfaces becomes substantially small for the flux surfaces as they are apart from the separatrix. Therefore, the energy deposition is little affected by this plasma movement.

Movement of the strike point during the beta drop is shown in Fig. 3.11. The strike point remains on the target plate both for inner and outer divertors for the present plasma configuration and the present physics model of the DINA code.

Evaluations of the heat load in the mid-plane region (outboard limiter and ICRF antenna) during the TQ are summarized as follows:

- Heat load and energy deposition at the location of the first wall / limiter (retracted) during the TQ of disruptions are evaluated taking account of the inward plasma movement due to beta drop both for the operation with and w/o ICRF heating.
- The first wall and the limiter surface could marginally melt only for the ICRF operation with full energy TQ and broadest energy deposition width with careful shaping of the first wall and limiter surface (reduction of energy load density by a factor of *1/5-1/10* is assumed).
- However, numbers of such operation and disruption are limited.
- The heat load at the first wall and limiter during the thermal quench for the standard configuration (non-ICRF) can be made acceptable by careful shaping of the first wall and limiter for most of the cases.
- Energy load on the inner first wall will not be affected by the inward plasma movement due to beta drop.
- Movement of the divertor strike point during the inward plasma movement due to beta drop will be small and still within the target plate.

4.2 Heat Load and Erosion during VDEs

In the case of VDEs, the heat load on the *Be* first wall and tungsten baffle of the divertor cassette during two phases must be properly assessed. The first phase is during the vertical movement of the hot burning plasma limited by the first wall after the loss of vertical control. This phase can last for up to a few hundred *ms* for upward VDEs and for up to several tens of *ms* for downward VDEs. During this phase, the wall could melt or wall temperature increases, with which melting by the heat deposition during the subsequent phase can be enhanced. The second phase is during the TQ subsequently triggered after the vertical movement. Both upper and lower *Be* first walls and tungsten baffle must be examined, since upward and downward VDEs will occur with an equal probability.

4.2.1 Upward VDEs

Figure 3.12 shows equilibrium configurations during upward VDE at *600 ms* (dashed gray line; early phase of plasma touching the upper wall) and at *865 ms* (solid gray line; just before the TQ at $q=1.5$). The numbers on the wall are indicators of the position. The insert in Fig. 3.12 shows the time evolution of plasma current and edge safety factor. Fig. 3.13 shows the time evolution of the heat load (MW/m^2) on the wall position (*880-1060*) during the vertical movement (*550-865 ms*). It is assumed that after touching the wall, the plasma transits back to the L mode and the heat flow across the LCFS is *200 MW* (more than twice of the H mode phase). Radial profile of the heat flux at the outer mid-plane is assumed to be an exponential function with a decay length of λss. After the L mode transition, λss is assumed to become wider than that of the H mode phase, and thus, $\lambda ss \approx 1\ cm$ is assumed as a typical value in this paper. Detailed plasma magnetic configuration and incident angle of the field line with the first wall are taken into account in the evaluation of Fig. 3.13. Measure of melting, i.e., ε ($MJ/m^2/s^{1/2}$), can be evaluated by integrating the heat load of Fig. 3.13 and dividing the square root of the integration time duration. Fig. 3.14 shows the maximum value of ε at each wall position during the vertical movement (*550-865 ms*) for three different values of λss (solid line for *0.5 cm,* dashed line for *1 cm* and dotted line for *2 cm)*. It is seen that ε is well below the critical value for the melting of *Be* even for the narrow heat load width $\lambda ss=0.5\ cm$. Thus, melting will not occur during the vertical movement even if there is some asymmetry of heat load, e.g., between electron and ion sides. Such a low value of ε is attributed to the very shallow intersecting angle of the flux surfaces with the wall. Another possible important factor in the evaluation of ε is misalignment, but this is beyond the scope of this paper. At some moment during the vertical movement, a TQ will occur. Figure 3.15 shows ε during the TQ at each wall position at two occurrence times of the TQ, i.e., *600 ms* (bold dotted line) and *865 ms* (bold solid line). It is assumed that W_{peak} of *175MJ* is released during the TQ with an energy deposition width of *5 cm* and a time duration of the energy deposition of *1.5 ms*. The thin solid line with open triangles show the maximum values when the TQ occurs at an arbitrary time between *550 ms* and *865 ms*. The lower dotted horizontal line shows the critical value for melting of *Be*. The critical value for tungsten is also shown for comparison (upper dotted line; $\approx 60\ MJ/m^2/s^{1/2}$). It is seen from Fig. 3.15 that a wide region of the wall receives the heat in the early phase while ε exceeds the critical value for melting of *Be* in limited regions. In the later phase, ε significantly exceeds the critical value in some regions. Of particular concern is the energy load on the upper wall (position from *720* to *760)*, where a loss of $\approx$*30-100* μm/event is expected by MDs. From Fig. 3.15, it is expected that the energy deposition on this region is not so large and the deposition is restricted to when the TQ occurs in the early phase of the vertical movement after the plasma touches the wall. Thus, the additional loss by melting of this region due to VDEs will not be significant.

Calculations of two-dimensional heat conduction for the region with the largest energy deposition (at the wall position *1013*) have been performed to evaluate the loss of *Be*. Figs 3.16 (a) and (b) show the heat load, surface temperature and melting/vaporized thickness at this wall position. The wall starts to receive heat load from *560 ms* as shown in Fig. 3.16 (b) and the surface temperature increases up to 660 *K* before the TQ (*855 ms*) as shown in Fig. 3.16 (a). At the TQ, additional large heat load up to $2.3\ GW/m^2$ deposits on this wall, which leads to $\approx$*167* μm/event total loss of the wall by melting/vaporization. Thus, substantial reduction of the number of occurrence of unmitigated VDEs is essential to maintain a reasonable lifetime of the first wall. As stated in Sec. 2, this reduction will be feasible by constructing a reliable position detection system and disruption mitigation system.

Another important point is how far the wall position of the largest erosion shifts depending on the initial plasma condition. In other words, whether or not the same wall position suffers from the largest erosion by every VDE. To answer this question, all possible initial plasma conditions must be investigated and it is difficult to perform a thorough investigation. In this paper, we examine only limited cases, i.e., different initial internal inductance ℓ_i, which is one of the most likely differences in the initial plasma condition.

Figures 3.17-3.21 and Figures 3.22-3.26 show the analyses results on the initial plasma with the internal inductance, $l_i = 0.7$ and 1.0, respectively. Note that the vertical movement is slower for lower l_i case than the higher one due to smaller growth rate of the vertical instability (i.e., stabilizing effect by the VV is stronger for flat current profile). Figure 3.17 shows equilibrium configurations during a upward VDE at *650 ms* (dashed gray line; early phase of plasma touching the upper wall) and at *1020 ms* (solid gray line; just before the TQ at $q=1.5$). The insert in Fig. 3.17 shows the time evolution of plasma current and edge safety factor. Fig. 3.18 shows the time evolution of the heat load (MW/m^2) on the wall position (*870-1050*) during the vertical movement (*650-1020 ms*). Fig. 3.19 shows the maximum value of ε at each wall position during the vertical movement (*650-1020 ms*) for three different values of λss (solid line for *0.5 cm,* dashed line for *1 cm* and dotted line for *2 cm)*. It is seen that ε is well below the critical value for the melting of *Be* even for the narrow heat load width $\lambda ss=0.5\ cm$. At some moment during the vertical movement, a TQ will occur. Figure 3.20 shows ε during the TQ at each wall position at two occurrence times of the TQ, i.e., *650 ms* (bold dotted line) and *1020 ms* (bold solid line). It is assumed that W_{peak} of *175MJ* is released during the TQ with an energy deposition width of *5 cm* and a time duration of the energy deposition of *1.5 ms*. The thin solid line with open triangles show the maximum values when the TQ occurs at an arbitrary time between *620 ms* and *1020 ms*. It is seen from Fig. 3.20 that a wide region of the wall receives the heat in the early phase while ε exceeds the critical value for melting of *Be* in limited regions. In the later phase, ε significantly exceeds the critical value in some regions. Calculations of two-dimensional heat conduction for the region with the largest energy deposition (at the wall position *863*) have been performed to evaluate the loss of *Be*. Figs 3.21 (a) and (b) show the heat load, surface temperature and melting/vaporized thickness at this wall position. The wall starts to receive heat load from *925 ms* as shown in Fig. 3.21 (b) and the surface temperature increases up to 600 *K* before the TQ (*1020 ms*) as shown in Fig. 3.21 (a). At the TQ, additional large heat load up to $2.2\ GW/m^2$ deposits on this wall, which leads to $\approx 140\ \mu m$/event total loss of the wall by melting/vaporization.

Figure 3.22 shows equilibrium configurations during a upward VDE at *500 ms* (dashed gray line; early phase of plasma touching the upper wall) and at *690 ms* (solid gray line; just before the TQ at $q=1.5$). The insert in Fig. 3.22 shows the time evolution of plasma current and edge safety factor. Fig. 3.23 shows the time evolution of the heat load (MW/m^2) on the wall position (*890-1050*) during the vertical movement (*500-690 ms*). Fig. 3.24 shows the maximum value of ε at each wall position during the vertical movement (*500-690 ms*) for three different values of λss (solid line for *0.5 cm,* dashed line for *1 cm* and dotted line for *2 cm)*. It is seen that ε is well below the critical value for the melting of *Be* even for the narrow heat load width $\lambda ss=0.5\ cm$. At some moment during the vertical movement, a TQ will occur. Figure 3.25 shows ε during the TQ at each wall position at two occurrence times of the TQ, i.e., *500 ms* (bold dotted line) and *690 ms* (bold solid line). It is assumed that W_{peak} of *175MJ* is released during the TQ with an energy deposition width of *5 cm* and a time duration of the energy deposition of *1.5 ms*. The thin solid line with open triangles show the maximum values when the TQ occurs at an arbitrary time between *480 ms* and *690 ms*. It is seen from Fig. 3.25

that a wide region of the wall receives the heat in the early phase while ε exceeds the critical value for melting of *Be* in limited regions. In the later phase, ε significantly exceeds the critical value in some regions. Calculations of two-dimensional heat conduction for the region with the largest energy deposition (at the wall position *1018*) have been performed to evaluate the loss of *Be*. Figs 3.26 (a) and (b) show the heat load, surface temperature and melting/vaporized thickness at this wall position. The wall starts to receive heat load from *480 ms* as shown in Fig. 3.26 (b) and the surface temperature increases up to 670 *K* before the TQ (*690 ms*) as shown in Fig. 3.26 (a). At the TQ, additional large heat load up to $2.4\ GW/m^2$ deposits on this wall, which leads to $\approx 170\ \mu m$/event total loss of the wall by melting/vaporization.

Figure 3.27 shows the comparison of the possible maximum ε during the TQ for two different internal inductances, *0.7* (dashed line taken from open triangles in Fig. 3.20) and *1.0* (dotted line taken from open triangles in Fig. 3.25) with the reference case (solid line taken from open triangles in Fig. 3.15). It is seen from this figure that positions of the largest erosion are very close for these cases.

4.2.2 Downward VDEs

Figure 3.28 shows equilibrium configurations during a downward VDE at *600 ms* (dashed gray line; early phase of plasma touching the upper wall) and at *645 ms* (solid gray line; just before the TQ at $q=1.5$). The insert in Fig. 3.28 shows the time evolution of plasma current and edge safety factor. Fig. 3.29 shows the time evolution of the heat load (MW/m^2) on the wall position (*1770-1890*) during the vertical movement (*570-645 ms*). It is seen from Fig. 3.29 that, in the downward VDE, the plasma is limited mainly by the tungsten divertor baffle and, thus, this region (*1840-1890*) receives large heat load. In contrast, the heat load on the *B*e first wall of No. 18 blanket module (*1770-1790*) is rather small due to the small intersecting angle of the wall with the flux surface. This feature can be clearly seen by evaluating ε at each wall position. Figure 3.30 shows the maximum ε ($max.\varepsilon$) at each wall position after the plasma touches the wall during the vertical movement (*570-645 ms*) for three different widths of heat flux at the mid-plane λss (solid line for *0.5 cm*, dashed line for *1 cm* and dotted line for *2 cm*). The heat flow across the LCFS is *200 MW*. It is seen that the $max.\varepsilon$ for the *Be* first wall is much lower than those of the upward VDE case, whereas the peak value of the *max.*ε for the divertor baffle region is larger than the upward VDE case due to the larger intersecting angle between the flux surfaces and the wall. However, the *max.*ε is below the critical value for melting even for the tungsten baffle during this phase.

Figure 3.31 shows ε during the TQ at each wall position at two occurrence times of the TQ, i.e., *600 ms* (bold dotted line) and *645 ms* (bold solid line). It is assumed that W_{peak} of *175MJ* is released during the TQ with an energy deposition width of *5 cm* and a duration of the energy deposition of *1.5 ms*. The thin solid line with open triangles show the maximum values when the TQ occurs at an arbitrary time between *550 ms* and *645 ms*. Although ε exceeds the critical value for melting, it is somewhat smaller for the *B*e first wall (*1600-1780*) than the upward VDE case. A much larger ε is anticipated for the tungsten baffle region and the value significantly exceeds the critical value for melting ($60\ MJ/m^2/s^{1/2}$). Calculations of two-dimensional heat conduction for the region with the largest energy deposition (at the wall position *1842*) have been performed to evaluate the loss of tungsten. Figure 3.32 (b) shows the heat load during the vertical movement and the TQ. The wall receives a heat load of $17.5\ MW/m^2$ just before the TQ and $6.54\ GW/m^2$ during the TQ as shown in Fig. 3.32 (b). Figure 3.32 (a) shows the surface temperature and melting/vaporized thickness at this baffle position. The surface temperature increases up to *750 K* before the TQ and reaches *6760 K* during the TQ. Consequently, the total loss of tungsten at this baffle position is ≈235 μm/event.

The analyses with varied l_i of the initial plasma were also performed. Figures 3.33-3.37 and Figures 3.38-3.42 show the analyses results on the initial plasma with the internal inductance, $l_i = 0.7$ and 1.0, respectively. The vertical movement is slower for lower l_i case than the higher one same as the upward VDEs. Figure 3.33 shows equilibrium configurations during a downward VDE at *780 ms* (dashed gray line; early phase of plasma touching the upper wall) and at *825 ms* (solid gray line; just before the TQ at $q=1.5$). The insert in Fig. 3.33 shows the time evolution of plasma current and edge safety factor. Fig. 3.34 shows the time evolution of the heat load (MW/m^2) on the wall position (*1760-1890*) during the vertical movement (*750-825 ms*). Figure 3.35 shows the maximum ε (*max.*ε) at each wall position after the plasma touches the wall during the vertical movement (*750-825 ms*) for three different widths of heat flux at the mid-plane λss (solid line for *0.5 cm*, dashed line for *1 cm* and dotted line for *2 cm*). The heat flow across the LCFS is *200 MW*. Figure 3.36 shows ε during the TQ at each wall position at two occurrence times of the TQ, i.e., *780 ms* (bold dotted line) and *825 ms* (bold solid line). It is assumed that W_{peak} of *175MJ* is released during the TQ with an energy deposition width of *5 cm* and a duration of the energy deposition of *1.5 ms*. The thin solid line with open triangles show the maximum values when the TQ occurs at an arbitrary time between *750 ms* and *825 ms*. Although ε exceeds the critical value for melting, it is somewhat smaller for the *B*e first wall (*1600-1780*) than the upward VDE case. A much larger ε is anticipated for the tungsten baffle region and the value significantly exceeds the critical value for melting ($60\ MJ/m^2/s^{1/2}$). Calculations of two-dimensional heat conduction for the region with the largest energy deposition (at the wall position *1842*) have been performed to evaluate the loss of tungsten. Figure 3.37 (b) shows the heat load during the vertical movement and the TQ. The wall receives a heat load of $9.4\ MW/m^2$ just before the TQ and $6.91\ GW/m^2$ during the TQ as shown in Fig. 3.37 (b). Figure 3.37 (a) shows the surface temperature and melting/vaporized thickness at this baffle position. The surface temperature increases up to *700 K* before the TQ and reaches *6780 K* during the TQ. Consequently, the total loss of tungsten at this baffle position is $\approx 240\ \mu m$/event.

Figure 3.38 shows equilibrium configurations during a downward VDE at *520 ms* (dashed gray line; early phase of plasma touching the upper wall) and at *555 ms* (solid gray line; just before the TQ at $q=1.5$). The insert in Fig. 3.38 shows the time evolution of plasma current and edge safety factor. Fig. 3.39 shows the time evolution of the heat load (MW/m^2) on the wall position (*1760-1890*) during the vertical movement (*490-555 ms*). Figure 3.40 shows the maximum ε ($max.\varepsilon$) at each wall position after the plasma touches the wall during the vertical movement (*490-555 ms*) for three different widths of heat flux at the mid-plane λss (solid line for *0.5 cm*, dashed line for *1 cm* and dotted line for *2 cm*). The heat flow across the LCFS is *200 MW*. Figure 3.41 shows ε during the TQ at each wall position at two occurrence times of the TQ, i.e., *520 ms* (bold dotted line) and *555 ms* (bold solid line). It is assumed that W_{peak} of *175MJ* is released during the TQ with an energy deposition width of *5 cm* and a duration of the energy deposition of *1.5 ms*. The thin solid line with open triangles show the maximum values when the TQ occurs at an arbitrary time between *490 ms* and *555 ms*. Although ε exceeds the critical value for melting, it is somewhat smaller for the *B*e first wall (*1600-1780*) than the upward VDE case. A much larger ε is anticipated for the tungsten baffle region and the value significantly exceeds the critical value for melting ($60\ MJ/m^2/s^{1/2}$). Calculations of two-dimensional heat conduction for the region with the largest energy deposition (at the wall position *1842*) have been performed to evaluate the loss of tungsten. Figure 3.42 (b) shows the heat load during the vertical movement and the TQ. The wall receives a heat load of $27.9\ MW/m^2$ just before the TQ and $6.01\ GW/m^2$ during the TQ as shown in Fig. 3.42 (b). Figure 3.42 (a) shows the surface temperature and melting/vaporized thickness at this baffle position. The surface temperature increases up to *628 K* before the TQ and reaches *6720 K* during the TQ. Consequently, the total loss of tungsten at this baffle position is $\approx 225\ \mu m$/event.

Figure 3.43 shows the results of comparison of ε for two different internal inductances, *0.7* (dashed line taken from open triangles in Fig. 3.36) and *1.0* (dotted line taken from open triangles in Fig. 3.41) with the reference case (solid line taken from open triangles in Fig. 3.31). The positions of the largest erosion on the tungsten baffle are very close for these cases. The peak value of ε on the *Be* first wall for $\ell_i=1.0$ becomes somewhat larger than the reference case, whereas it is still smaller than the case of upward VDEs.

These evaluations conclude that the *Be* first wall will not melt during the vertical movement even after the plasma touches the wall both for upward and downward VDEs. Significant melting is, however, anticipated for the upper *Be* wall and tungsten divertor baffle during the TQ. It is naturally expected that the lifetime can be substantially prolonged if any mitigation can be triggered before the occurrence of the TQ during most of VDEs. This point will be discussed in the next section in detail.

5. Possible Reduction of Erosion by Disruption Prediction and Mitigation

Recently, significant progress has been made both on disruption prediction and mitigation methods. In this section, we will briefly examine the possible reduction of erosion by employing recently developed disruption prediction and mitigation methods. For the mitigation, MGI has been developed [13-16] and it has been confirmed that the localized heat load on the divertor and the wall due to the TQ, runaway electron generation and halo current during current quench phase can be significantly reduced. Thus, a substantial reduction of erosion can be expected by combining this mitigation system with an appropriate disruption prediction system. Prediction algorithms based on neural network system have been developed in many machines [17-23]. In this paper, we will employ the neural network disruption prediction system recently developed based on JT-60U disruption data as an example [22, 23]. One major advantage of this network system is that the prediction success rate can be significantly increased by maintaining the prediction false rate very low (typically $\approx 2\%$) for various types of disruptions, e.g., density limit, locked mode, high internal inductance disruptions. Here, the prediction false rate is defined as the ratio of the number of non-disruptive discharges, to which the mitigation is erroneously triggered, to the total number of non-disruptive discharges. The prediction success rate strongly depends on the time delay of the mitigation system. Inherent time delay of the MGI system is the traveling time of the gas through the gas delivery pipe. When we assume that the length of the pipe is 2m, the required time for the gas to reach the plasma edge from the gas reservoir is ≈5.3 ms for neon and ≈7.5 ms for argon. Another time delay is the required time to trigger the radiation collapse after the gas reaches the plasma edge. In DIII-D experiments, this time delay is *2-3 ms* [15]. Thus, the total time delay τ_0 will be at least *≈5-10 ms* including all other possible time delays in the overall prediction/mitigation system. In Ref. [22], the prediction success rate is evaluated as a function of the time prior to the disruption onset, which is equivalent to τ_0 in the present definition, for various types of disruptions. Figure 4.1 shows the prediction missed rate (1-success rate) as a function of τ_0 for density limit (red solid line), locked mode (green dashed line) and high internal inductance (purple dotted line) disruptions evaluated from the data provided in Ref. [22]. From this figure, the prediction missed rate for τ_0 ≈5-*10 ms* is *≈2-3%* for these types of disruptions. Based on these considerations, if we assume that the total number of shots N with full fusion power is 3×10^4 and *10%* of these shots (3×10^3) disrupt, the numbers of mitigation success shots, missed rate and shots, false rate and shots can be estimated and are summarized in Table 6. Hundreds of missed shot could be marginally acceptable for the possible maximum erosion due to MDs (*≈100μm*/event). In the case of VDEs, there will be very high chance of realizing such a prediction/mitigation system, since it takes more than *0.5 s* before the plasma starts to contact the wall during VDEs in ITER. Consequently, the plasma movement can be detected and the mitigation is triggered. Thus, it is expected that the unmitigated VDEs can be reduced to a few shots during the whole life of ITER.

There are several points to be carefully investigated in these estimations. The first point is the prediction capability for high beta disruptions. At present, the prediction success rate is still not satisfactory (up to *≈80%*) for these disruptions [25, 26]. In addition, it is shown that the energy release during the TQ for these disruptions is close to the highest of these discharges (i.e., energy loss before the TQ is small) [10, 11]. Substantial improvement of the prediction capability for high beta disruptions is an important item of future physics R&D. A more sophisticated algorithm of the neural network system using not only global parameters but also profile data will probably be necessary for this improvement.

The second point is that certain numbers of disruption shots are necessary during the learning phase of the neural network system. It is shown in Ref. [24] that less than *100* shots are enough to establish the algorithm of the system. Further reduction of the necessary numbers of disruption shot is another important physics R&D. In Ref. [27], it is shown that some degradation of the prediction success rate is anticipated when a neural network system is applied to one machine after developed in other machine, e.g., between JET and ASDEX-U. This result, however, should not be applied to ITER directly. In ITER, incessant improvement of the algorithm and weight will be performed during lower current and power discharges, so that the success rate for discharges with full current and power could be as high as the optimized case for the existing machines.

The third point is possible melting of the *Be* first wall by the localized radiation due to the injected massive impurity gas for disruption mitigation. Since the number of gas injections for disruption mitigation are more than *3000* (see Table 6), even small erosion/injection can lead to large total erosion during the life. Figure 4.2 shows time evolution of the surface temperature and melting/vaporized thickness during the radiation collapse after gas injection for the cases with (a) toroidally and poloidally uniform distribution and (b) a factor of 2 peaking. It is assumed that the total stored energy before the TQ is *350 MJ* and time duration of the radiation collapse is *1 ms*. It is seen from these figures that the *Be* wall will not melt when the peaking is small, whereas melt layer thickness is significant if the radiation is localized. As was described before, present experiments in DIII-D show that there is a time delay of several *ms* before the onset of the radiation collapse after the gas reaches the plasma edge; therefore the injected impurity could travel toroidally and poloidally to some extent. It is also important to enhance the uniformity by preparing several gas injection pipes distributed uniformly in the toroidal direction.

6. Conclusions

Several representative disruption scenarios have been specified and disruption simulations are performed with the DINA code based on newly derived physics guidelines for the shortest current quench time and their waveforms ($\Delta t \approx 36\ ms$ linear and $\tau \approx 16\ ms$ exponential waveforms). Analyses of the EM load generated by the induced eddy and halo currents on BMs have been performed with the 3D FEM code for these scenarios. The guideline for the maximum product of halo current fraction and toroidal peaking factor (maximum $f_h \approx 0.7$) expected in ITER is also used for the analyses. Simulation for the downward VDE with slow current decay is performed to obtain maximum poloidal halo current, which is essential for the vertical force on the VV. Some margins are confirmed in the EM loads due to induced eddy and halo currents on the BMs and the VV for these representative scenarios. However, the margins are not large, and thus further efforts both from the physics and engineering sides are needed to enlarge the margins. The disruption prediction/mitigation system cannot improve the margin substantially, since the prediction cannot be *100%* reliable.

The heat loads on various parts of the first wall due to vertical movements and TQ have been calculated based on the database of heat deposition during disruptions and simulation results with the DINA code. It is concluded that melting of the *Be* wall and tungsten baffle during vertical movement before the TQ will not occur both for upward and downward VDEs. Melting is anticipated at the TQ after vertical movement. For upward VDEs, total loss (including melting and vaporized layer) of $\approx 170\ \mu m$/event is expected for the upper *Be* wall. For downward VDEs, total loss of $\approx 240\ \mu m$/event is expected for the tungsten baffle. Loss of *Be* wall for the #18 BM is smaller than that of the upper wall during upward VDEs. The position with the largest erosion has been investigated for different initial plasma conditions (different values of internal inductance ℓ_i). It has been shown that the position will not change so much for different initial internal inductance, which is one of the most likely differences in the initial plasma condition. More comprehensive studies on the initial plasma conditions, however, are necessary to draw definitive conclusions.

It has been shown that the lifetime of the wall limited by erosion could be extended substantially by implementing a reliable detection and mitigation system, e.g., MGI. This is particularly effective for VDEs, since it takes more than *500 ms* before the occurrence of the TQ after loss of vertical control. Thus, mitigation can be triggered with high reliability by constructing a reliable position detection system.

It has been shown that more severe melting is anticipated due to MDs, since for these disruptions, at least several tens of unmitigated disruptions must be considered even if an advanced prediction/mitigation system is implemented. With these unmitigated MDs the loss of *Be* layer is expected to be $\approx 30\text{-}100\ \mu m$/event.

Further R&D is necessary to improve the prediction success rate for high beta disruptions and to reduce the necessary disruption shots for the learning phase of the neural network disruption prediction system. Possible localization of the radiative heat load on the first wall due to the MGI is of some concern. Latest experiments, however, show that radiative heat load will not be so localized and ε is marginally below the critical value for melting.

Part of this study will be published in Ref. [43] with further detailed physics explanation.

Acknowledgements

The authors are grateful to Dr. K. Sato for arranging the run of the DREAM code and to Dr. R. Yoshino for providing the background data for Fig. 4.1. The authors are also grateful to Dr. R. Yoshino and Dr. Y. Shimomura for their continuous encouragements throughout this work.

References

[1] ITER Physics Basis, Nucl. Fusion **39** (1999) 2137.

[2] Hyatt, A.W. et al., 47th meeting of APS Division of Plasma Physics, Denver (2005), CP1.00004 and http://meetings.aps.org/Meeting/DPP05/Event/34790.

[3] Wesley, J., et al., in Fusion Energy 2006 (Proc. 21st Int. Conf. Chengdu, 2006) (Vienna: IAEA) CD-ROM file IT/P1-21 and http://www-naweb.iaea.org/napc/physics/FEC/FEC2006/html/index.htm.

[4] Granetz, R.S. et al., Nucl. Fusion **36** (1996) 545.

[5] Humphreys, D.A., Kellman, A.G., Phys. Plasmas **6** (1999) 2742.

[6] Neyatani, Y. et al., Nucl. Fusion **39** (1999) 559.

[7] Knight, P.J. et al., Nucl. Fusion **40** (2000) 325.

[8] Riccardo, V., Plasma Phys. Control. Fusion **45** (2003) A269.

[9] Riccardo, V. et al., Plasma Phys. Control. Fusion **44** (2002) 905.

[10] Riccardo, V. et at., Nucl. Fusion **45** (2005) 1427.

[11] Loarte, A. et al., in Fusion Energy 2004 (Proc. 20th Int. Conf. Vilamoura, 2004) (Vienna: IAEA) CD-ROM file IT/P3-34 and http://www-naweb.iaea.org/napc/physics/fec/fec2004/datasets/index.htm.

[12] Loarte, A. et al., in Fusion Energy 2006 (Proc. 21st Int. Conf. Chengdu, 2006) (Vienna: IAEA) CD-ROM file IT/P1-14 and http://www-naweb.iaea.org/napc/physics/FEC/FEC2006/html/index.htm.

[13] Whyte, D.G. et al., Phys. Rev. Lett. **89** (2002) 055001.

[14] Whyte, D.G., J., Nucl. Material. **313-316** (2003) 1239.

[15] Hollmann, E.M. et al., Nucl. Fusion **45** (2005) 1046.

[16] Granetz, R.S. et al., in Fusion Energy 2006 (Proc. 21st Int. Conf. Chengdu, 2006) (Vienna: IAEA) CD-ROM file EX/4-3 and http://www-naweb.iaea.org/napc/physics/FEC/FEC2006/html/index.htm.

[17] Hernandez, J.V. et al., Nucl. Fusion **36** (1996) 1009.

[18] Vannucci, A. et al., Nucl. Fusion **39** (1999) 255.

[19] Sengupta, A., Ranjan, P., Nucl. Fusion **40** (2000) 1993.

[20] Sengupta, A., Ranjan, P., Nucl. Fusion **41** (2001) 487.

[21] Pautasso, G. et al., J., Nucl. Material. **290-293** (2001) 1045.

[22] Pautasso, G. et al., Nucl. Fusion **42** (2002) 100.

[23] Cannas, B. et al., Nucl. Fusion **44** (2004) 68.

[24] Yoshino, R., Nucl. Fusion **43** (2003) 1771.

[25] Wroblewski, D. et al., Nucl. Fusion **37** (1997) 725.

[26] Yoshino, R., Nucl. Fusion **45** (2005) 1232.

[27] Windsor, C.G. et al., Nucl. Fusion **45** (2005) 337.

[28] Sugihara, M. et al., 30th EPS, St. Petersburg (2003), P-2.139.

[29] Sugihara, M., Lukash, V.E. et al., J. Plasma Fusion Science **79** (2003) 706.

[30] Riccardo, V. et al., Plasma Phys. Control. Fusion **47** (2005) 117.

[31] Sugihara, M., Lukash, V.E., et al., in Fusion Energy 2004 (Proc. 20th Int. Conf. Vilamoura, 2004) (Vienna: IAEA) CD-ROM file IT/P3-29 and http://www-naweb.iaea.org/napc/physics/fec/fec2004/datasets/index.html.

[32] Shimada, M., Sugihara, M., Fujieda, H., et al., in Fusion Energy 2006 (Proc. 21st Int. Conf. Chengdu, 2006) (Vienna: IAEA) CD-ROM file IT/P1-19 And http://www-naweb.iaea.org/napc/physics/FEC/FEC2006/html/index.htm.

[33] Riccardo, V., Plasma Phys. Control. Fusion **46** (2004) 925.

[34] Khayrutdinov, R.R., Lukash, V.E., J. Comp. Physics **109** (1993) 193.

[35] Sugihara, M., Lukash, V.E. et al., Plasma Phys. Control. Fusion **46** (2004) 1581.

[36] Lukash, V.E., Sugihara, M. et al., Plasma Phys. Control. Fusion **47** (2005) 2077.

[37] Rosenbluth, M.N., Putvinski, S.V., Nucl. Fusion **37** (1997) 1355.

[38] Helander, P. et al., Plasma Phys. Control. Fusion **44** (2002) B247.

[39] Gill, R.D. et al., Nucl. Fusion **42** (2002) 1039.

[40] Yoshino, R. Tokuda, S, Kawano, Y., Nucl. Fusion **39** (1999) 151.

[41] Yoshino, R. Tokuda, Nucl. Fusion **40** (2000) 1293.

[42] Yamazaki, S. Seki, M. et al., Japan Atomic Energy Research Institute Report, JAERI-M 88-163 (1988).

[43] Sugihara, M. Shimada, M. Fujieda, H. et al., Nucl. Fusion **47** (2007) 337.

Table 1
Major assumptions used in simulations with the DINA code for representative disruption scenarios

Physics guidelines \ Representative scenarios	Major Disruptions (MD)	Down and upward VDE with fast and slow current quench
1. Current quench waveform and time (Fast current quench case)	Linear *36ms* and Exponential *16 ms*	⇐
2. Thermal quench time duration	Beta drop : *1 ms* *j* flattening : ≈ *3 ms*	⇐
3. Surface q value at thermal quench	*3*	*1.5 – 2* [10]
4. Beta drop during thermal quench	≈ *0.72 - 0.75*	≈ *0.75 - 0.4*
5. Change of ℓ_i during thermal quench	*0.15 - 0.2*	⇐
6. $f_h \equiv (I_{h,max}/I_{p0}) \times TPF$ for VDE with slow current quench case		*0.7* for slow downward VDE

Table 2
Assumption taken from [11] used for the estimation of heat load on various part of the first wall during the TQ

Energy release at the TQ (relative to peak stored energy W_{peak})	$(0.5\text{-}1.0)\ W_{peak}$
Expansion factor of heat load width from the steady heat load width λss	*(5-10)*
Time duration of heat deposition on divertor/wall	*(1.5-3) ms*

Table 3
Range of peak heat load density and location on the upper wall during the TQ of MD for two cases of plasma stored energy (*175* and *350 MJ*) at the onset of the TQ

Case and peak location \ Energy loss / disruption	*175 MJ*	*350 MJ*
Reference : peak location (6) – (8) (MJ/m^2) (Fig.3.1)	*0.45 – 0.92*	*0.9 – 1.84*
Possible worst : peak location (f) - (g) (MJ/m^2) (Fig.3.1)	*0.9 – 1.44*	*1.8 – 2.9*

Table 4
Peak heat flux and total energy load density at L_0 =17.5 cm from the 1st separatrix

Thermal Energy Loss during thermal quench (*MJ*)	*175*	*350*
Peak heat flux at L_0 =*17.5 cm* (*GW/m²*) (Fig. 3.7) (Parallel to the field line)	*0.18 – 3.0** ($5\times\lambda_{ss}$ - $10\times\lambda_{ss}$)	*0.36 – 6.0** ($5\times\lambda_{ss}$ - $10\times\lambda_{ss}$)
Total energy load density at L_0 =*17.5 cm* (*MJ/m²*) (Parallel to the field line)	*0.045 – 1.3** ($5\times\lambda_{ss}$ - $10\times\lambda_{ss}$)	*0.09 – 2.6* ($5\times\lambda_{ss}$ - $10\times\lambda_{ss}$)
Time duration of heat deposition (*ms*)	*1.0*	*1.0*

*Range corresponds to the decay length of $5\times\lambda_{ss}$ (*25 mm*) and $10\times\lambda_{ss}$ (*50 mm*) at the outer mid-plane.

Table 5
Peak heat flux and total energy load density at L_0 =12 cm from the 1st separatrix

Thermal Energy Loss during thermal quench (*MJ*)	*175*	*350*
Peak heat flux at L_0 =*12 cm* (*GW/m²*) (Fig. 3.8) (Parallel to the field line)	*1.65 – 9.1** ($5\times\lambda_{ss}$ - $10\times\lambda_{ss}$)	*3.3 – 18.2** ($5\times\lambda_{ss}$ - $10\times\lambda_{ss}$)
Total energy load density at L_0 =*12 cm* (*MJ/m²*) (Parallel to the field line)	*0.4 - 3.9** ($5\times\lambda_{ss}$ - $10\times\lambda_{ss}$)	*0.8 – 7.9* ($5\times\lambda_{ss}$ - $10\times\lambda_{ss}$)
Time duration of heat deposition (*ms*)	*1.0*	*1.0*

*Range corresponds to the decay length of $5\times\lambda_{ss}$ (*25 mm*) and $10\times\lambda_{ss}$ (*50 mm*) at the outer mid-plane.

Table 6
Expected number of mitigation success shots, missed rate and shots, false rate and shots out of *3000* disruptive shots in ITER. Total time delay of the prediction and mitigation system is assumed to be *5-10* ms.

Total shots: $N=3\times10^4$ Disruptive shots ($0.1N$): 3×10^3	
Δt (*ms*)	$\approx$ *5-10*
Success shots	$\approx$ *2900-2950*
Missed rate (%) and shots	($\approx$ *2-3%*) $\approx$ *50-100*
False rate (%) and shots	($\approx$ *2%*) $\approx$ *600*

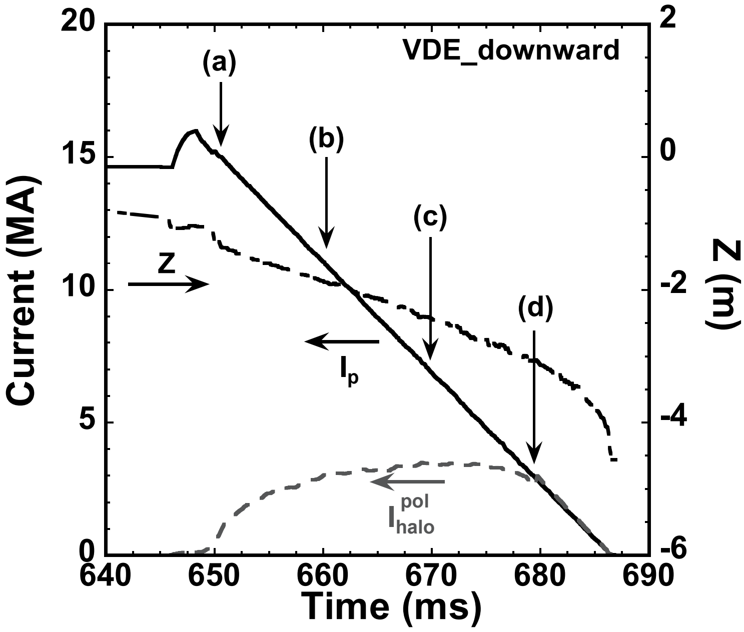

Figure 1.1 (a)
Time evolutions of the plasma current, the vertical position and the poloidal halo current for downward VDE for the linear quench waveform with *36 ms* current quench time simulated with the DINA code

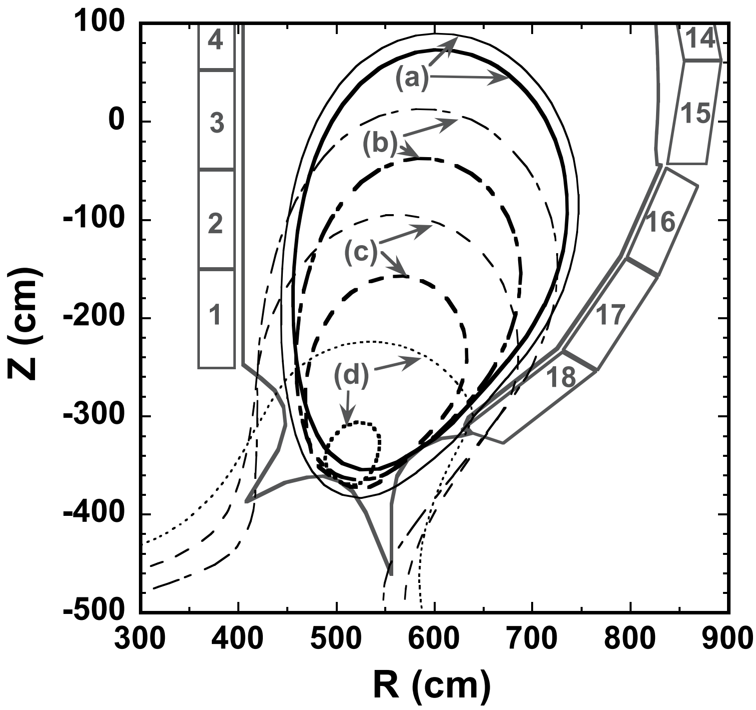

Figure 1.1 (b)
Four time slices of Last Closed Flux Surface (LCFS; bold line) and halo boundaries (thin line) at (a), (b), (c) and (d) in Fig. 1.1 (a)

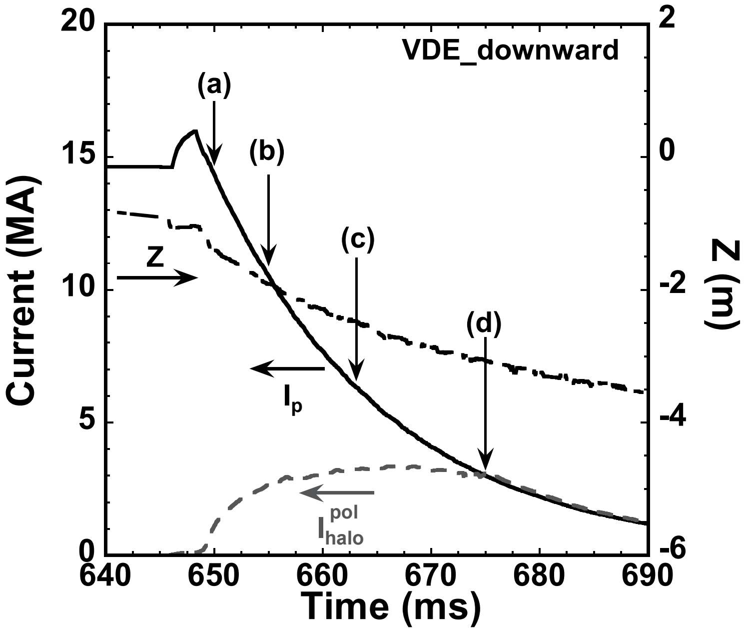

Figure 1.2 (a)
Time evolutions of the plasma current, the vertical position and the poloidal halo current for downward VDE for the exponential quench waveform with a time constant of *16 ms* simulated with the DINA code

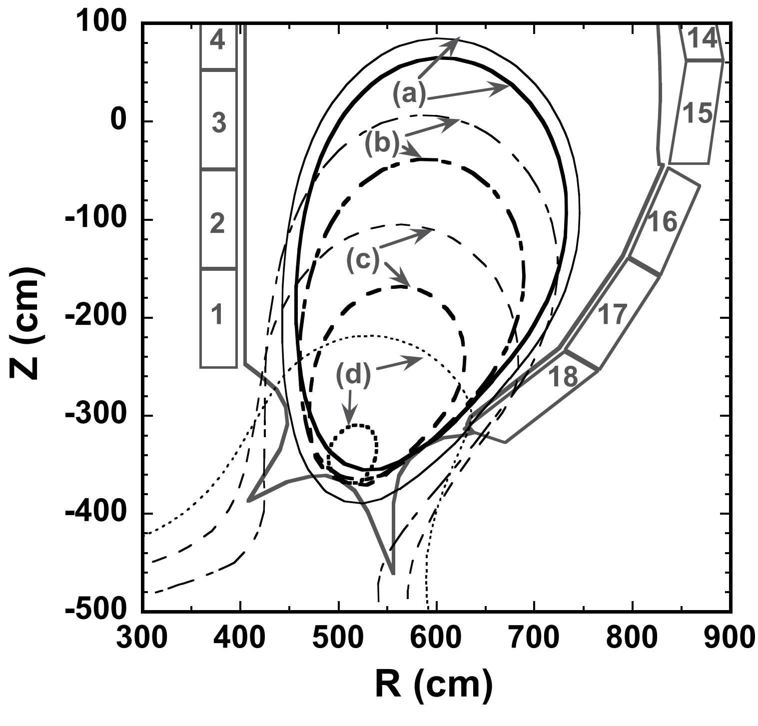

Figure 1.2 (b)
Four time slices of Last Closed Flux Surface (LCFS; bold line) and halo boundaries (thin line) at (a), (b), (c) and (d) in Fig. 1.2 (a)

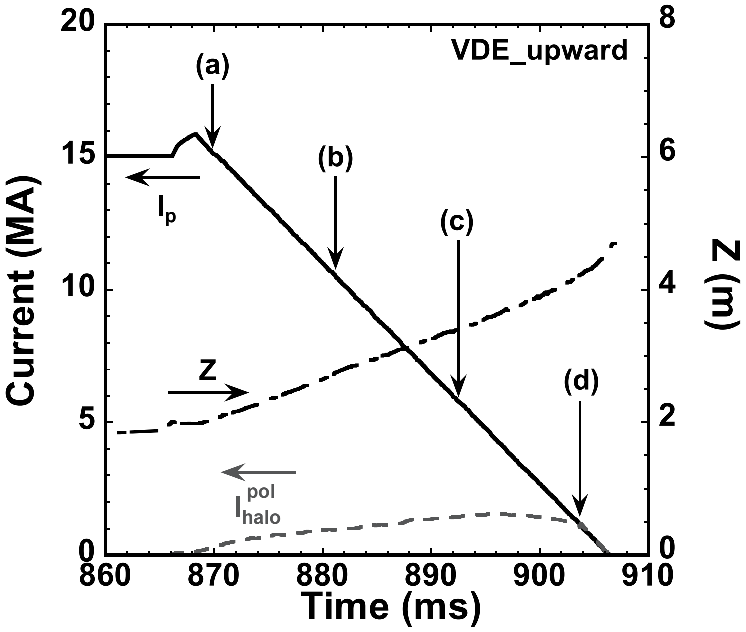

Figure 1.3 (a)
Time evolutions of the plasma current, the vertical position and the poloidal halo current for upward VDE for the linear quench waveform with *36* ms current quench time simulated with the DINA code

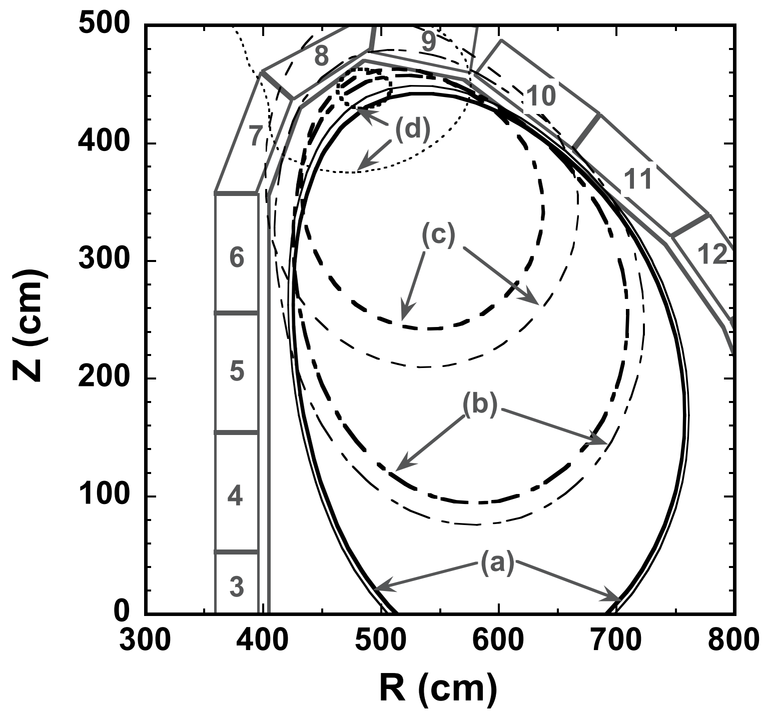

Figure 1.3 (b)
Four time slices of Last Closed Flux Surface (LCFS; bold line) and halo boundaries (thin line) at (a), (b), (c) and (d) in Fig. 1.3 (a)

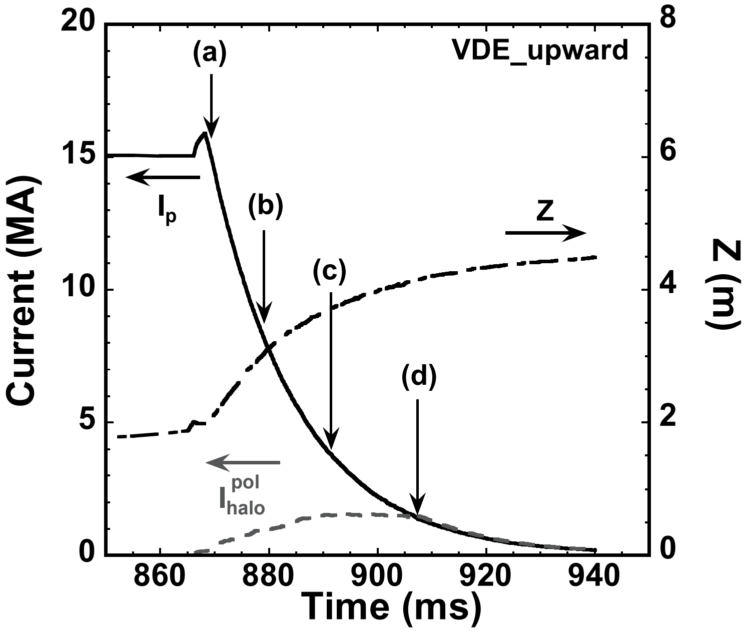

Figure 1.4 (a)
Time evolutions of the plasma current, the vertical position and the poloidal halo current for upward VDE for the exponential quench waveform with a time constant of *16* ms simulated with the DINA code

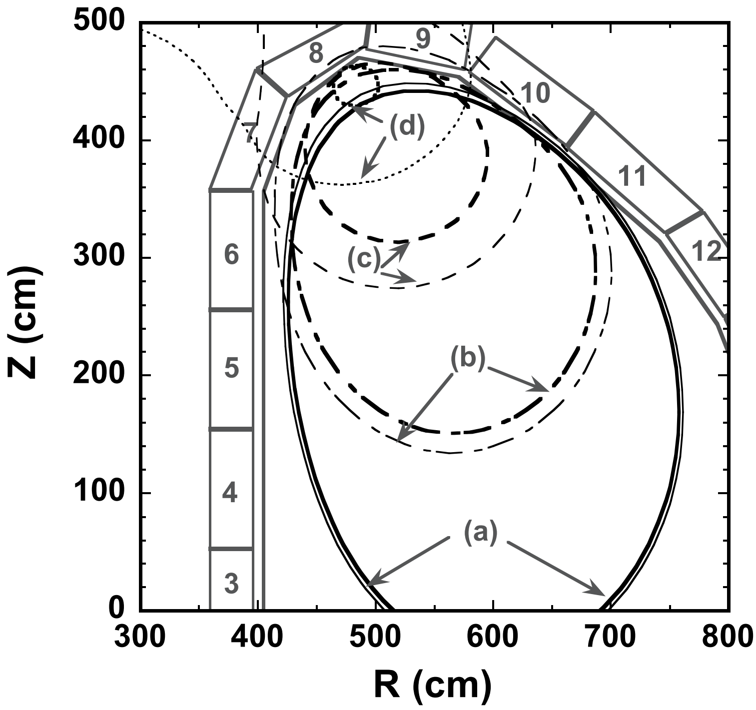

Figure 1.4 (b)
Four time slices of Last Closed Flux Surface (LCFS; bold line) and halo boundaries (thin line) at (a), (b), (c) and (d) in Fig. 1.4 (a)

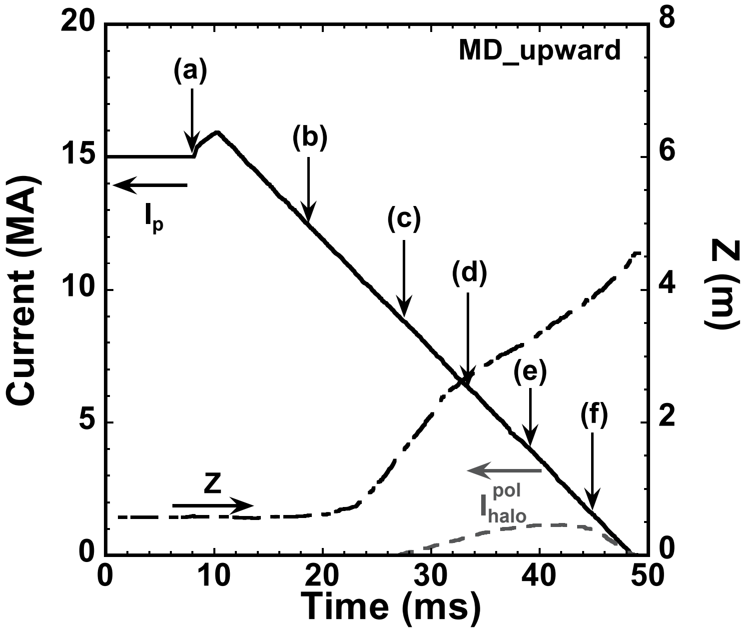

Figure 1.5 (a)
Time evolutions of the plasma current, the vertical position and the poloidal halo current for MD for the linear quench waveform with *36* ms current quench time simulated with the DINA code

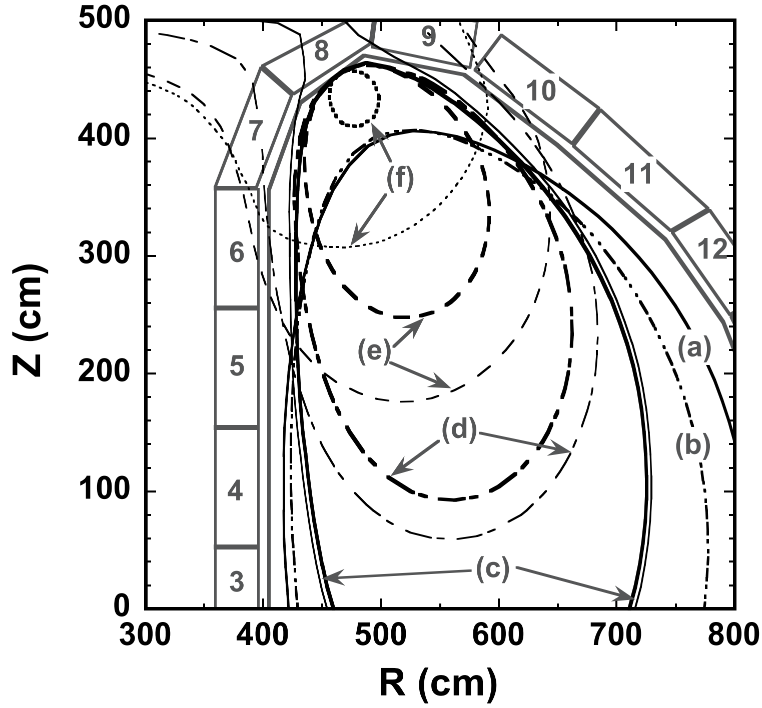

Figure 1.5 (b)
Six time slices of Last Closed Flux Surface (LCFS; bold line) and halo boundaries (thin line) at (a), (b), (c), (d), (e) and (f) in Fig. 1.5 (a)

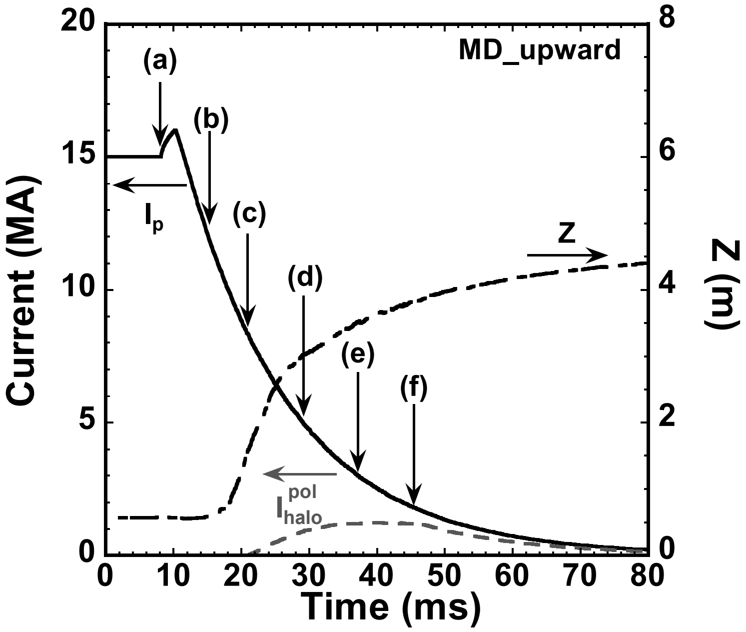

Figure 1.6 (a)
Time evolutions of the plasma current, the vertical position and the poloidal halo current for MD for the exponential quench waveform with a time constant of *16* ms simulated with the DINA code

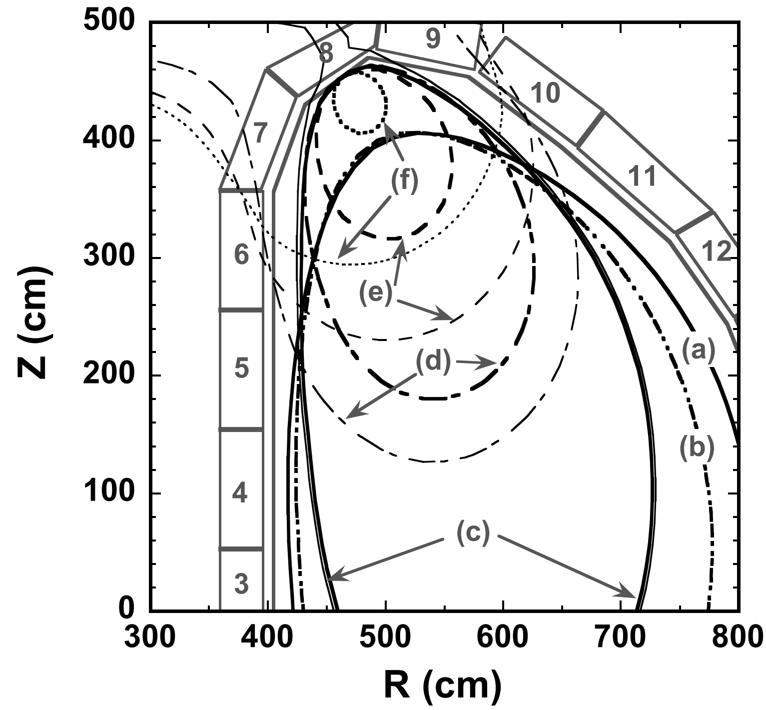

Figure 1.6 (b)
Six time slices of Last Closed Flux Surface (LCFS; bold line) and halo boundaries (thin line) at (a), (b), (c), (d), (e) and (f) in Fig. 1.6 (a)

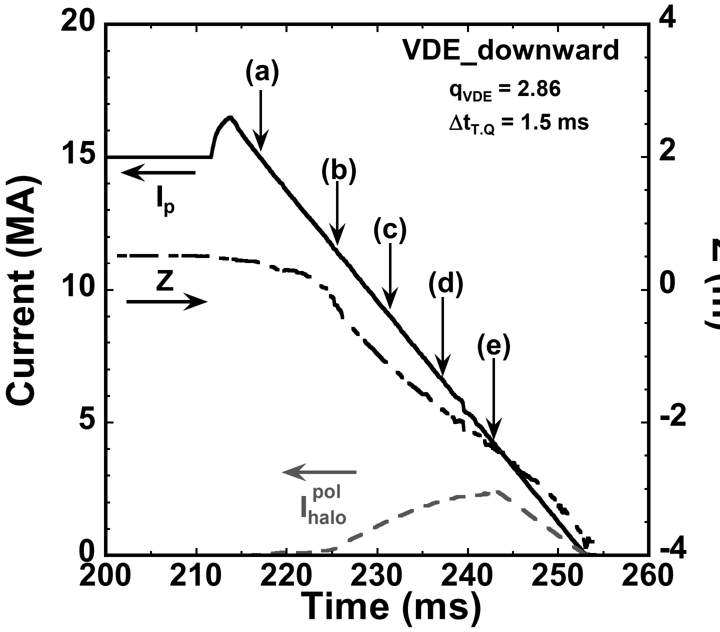

Figure 1.7 (a)
Time evolutions of the plasma current, the vertical position and the poloidal halo current for downward VDE for the linear quench waveform with *36 ms* simulated with the DINA code (TQ occurs at larger *q* value (*q=2.86*).)

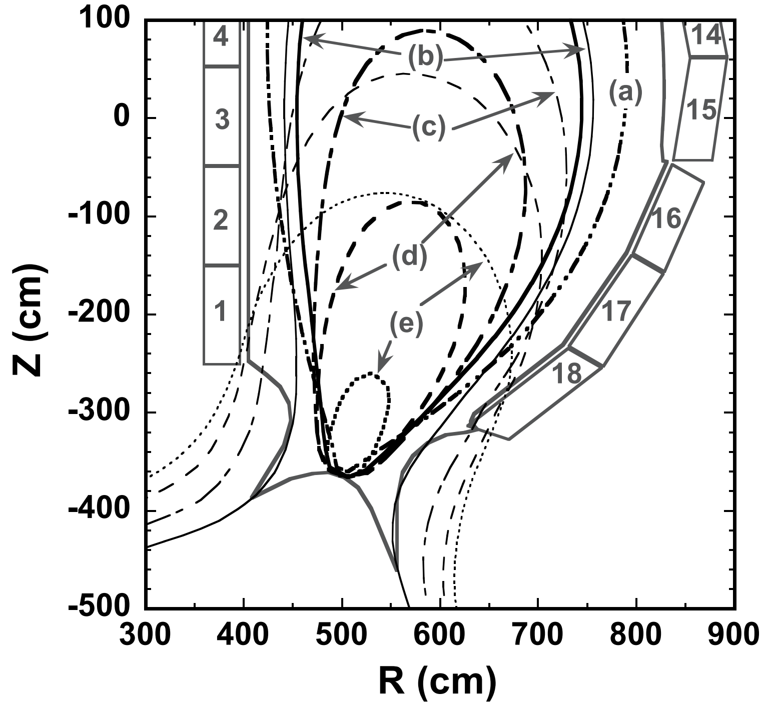

Figure 1.7 (b)
Five time slices of Last Closed Flux Surface (LCFS; bold line) and halo boundaries (thin line) at (a), (b), (c), (d) and (e) in Fig. 1.7 (a)

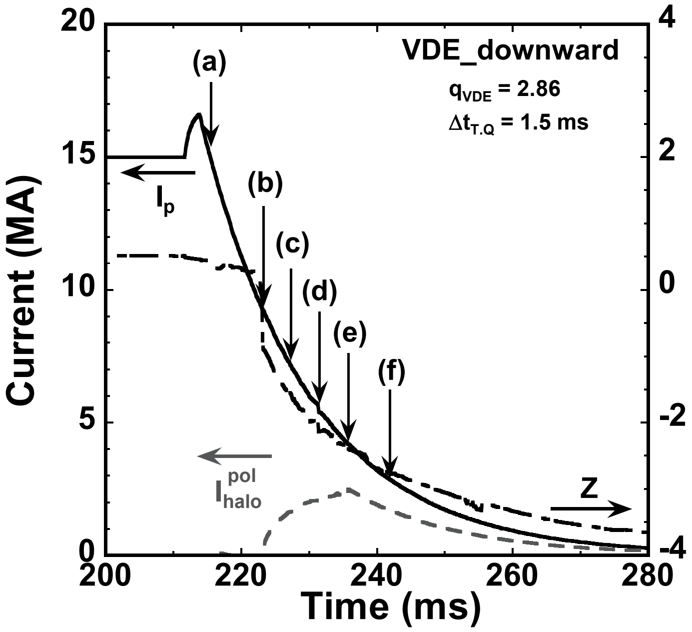

Figure 1.8 (a)
Time evolutions of the plasma current, the vertical position and the poloidal halo current for downward VDE for the exponential quench waveform with a time constant of *16 ms* simulated with the DINA code (TQ occurs at larger *q* value (*q=2.86*).)

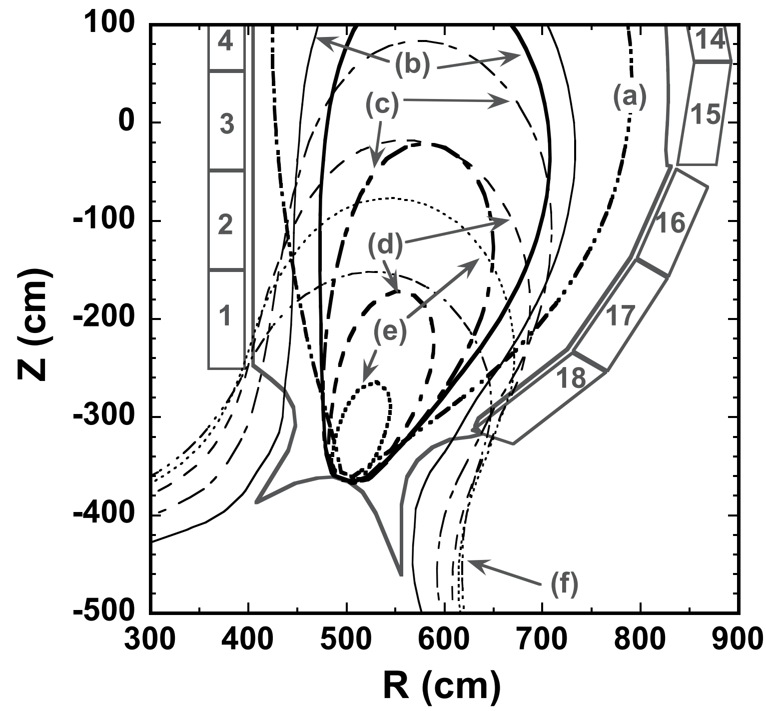

Figure 1.8 (b)
Five time slices of Last Closed Flux Surface (LCFS; bold line) and halo boundaries (thin line) at (a), (b), (c), (d) and (e) in Fig. 1.8 (a)

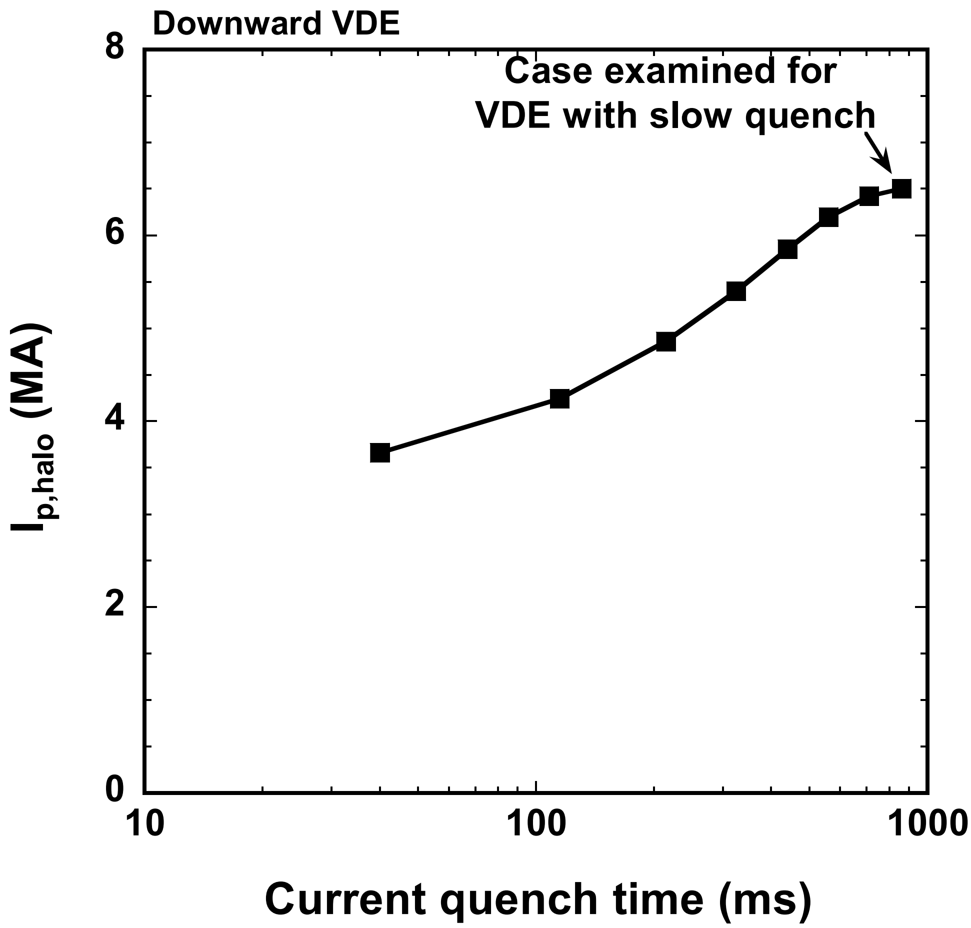

Figure 1.9
Maximum induced poloidal halo current during downward VDEs with various current quench times simulated with the DINA code

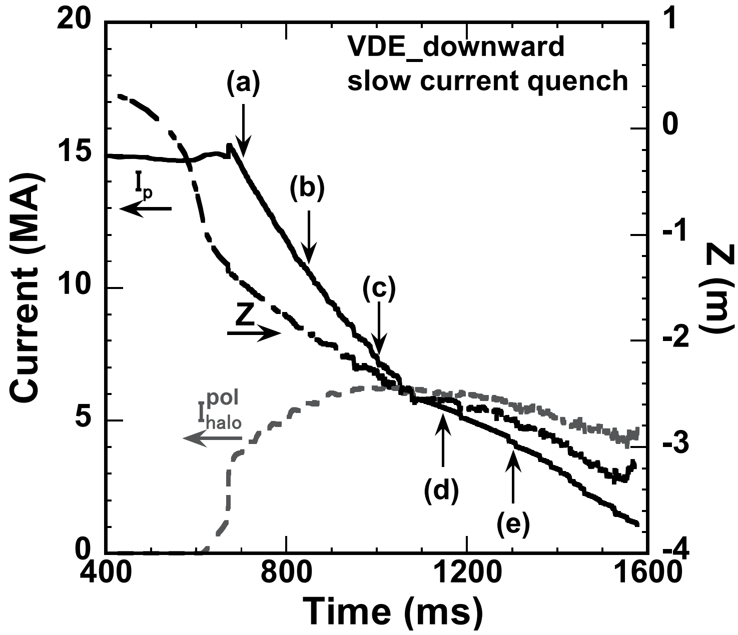

Figure 1.10 (a)
Time evolutions of the plasma current, the vertical position and the poloidal halo current for downward VDE with slow current quench (case shown by the arrow in Fig. 1.9) simulated with the DINA code

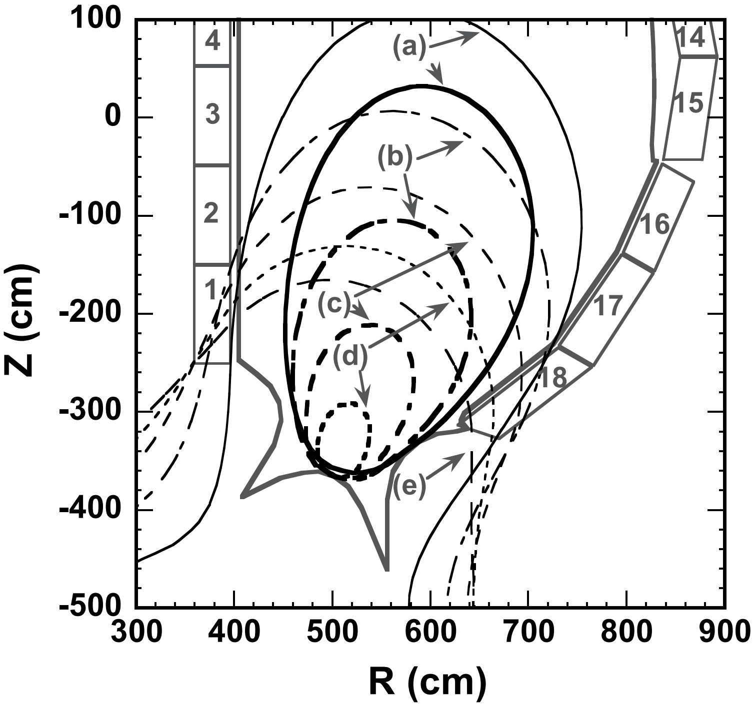

Figure 1.10 (b)
Four time slices of Last Closed Flux Surface (LCFS; bold line) and halo boundaries (thin line) at (a), (b), (c) and (d) in Fig. 1.10 (a)

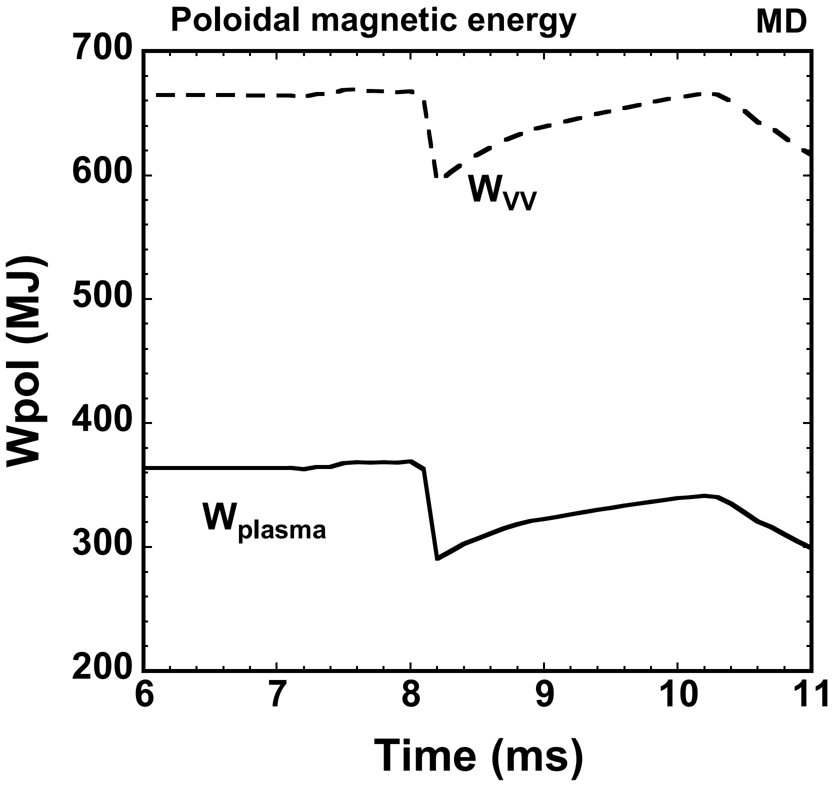

Figure 1.11
Poloidal magnetic energy inside the VV (W_{VV}) and plasma (W_{plasma})

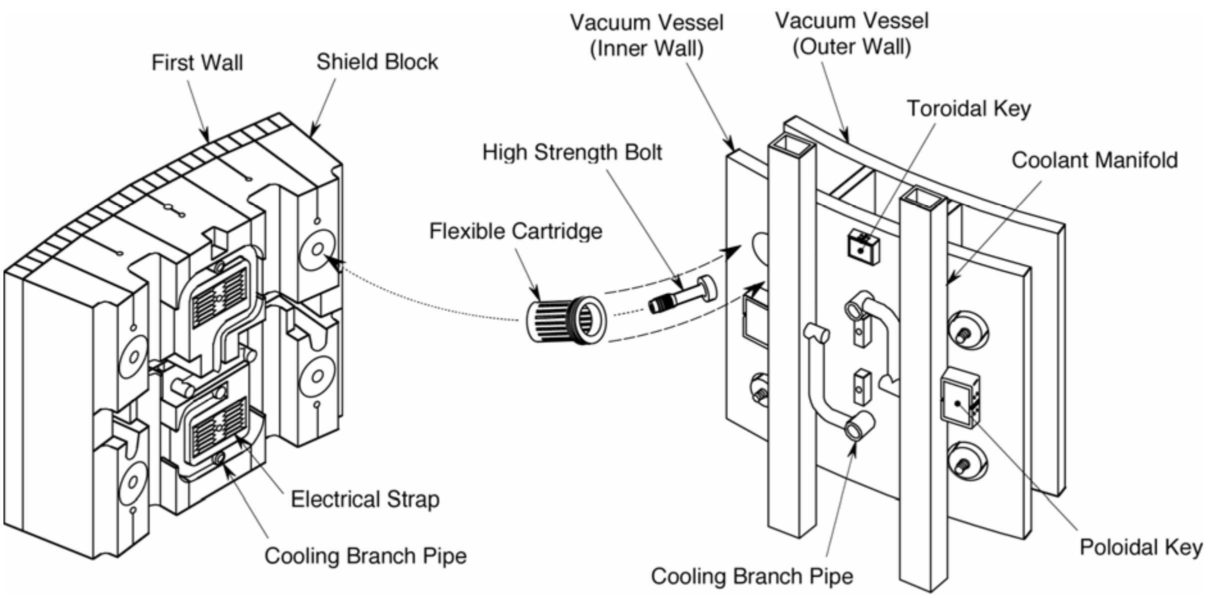

Figure 2.1
Design of a typical BM and its supporting structures (key and flexible support) on the VV

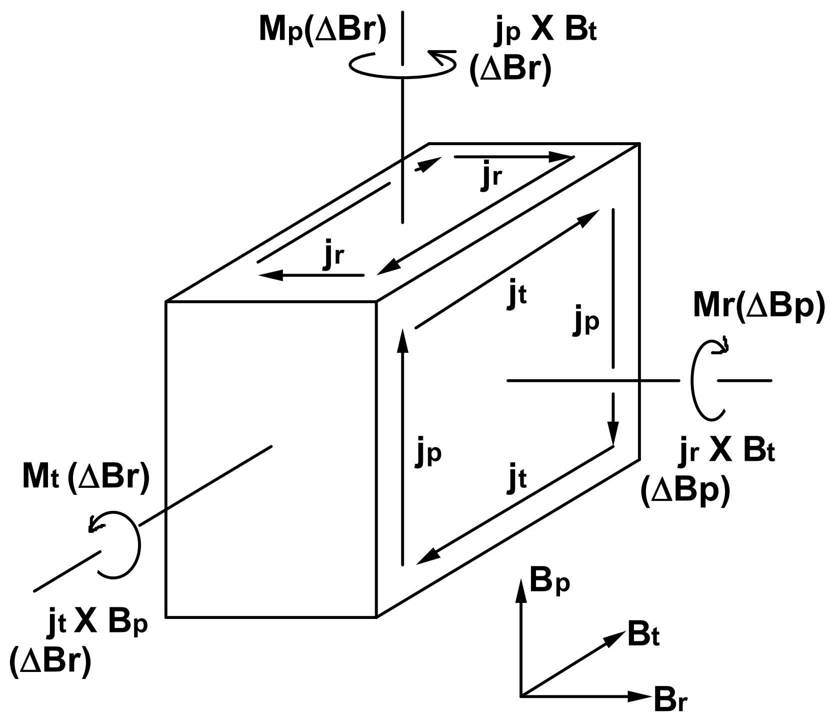

Figure 2.2
Schematics of the radial (Mr), poloidal (Mp) and toroidal (Mt) moments on BM generated by the coupling of induced eddy currents j_r in radial direction with the toroidal magnetic field B_t, in poloidal direction j_p with B_t and in toroidal direction j_t with the poloidal magnetic field B_p. Eddy current j_r is induced by the change of poloidal magnetic field (ΔB_p) and j_p and j_t are induced by the change of radial magnetic field (ΔB_r).

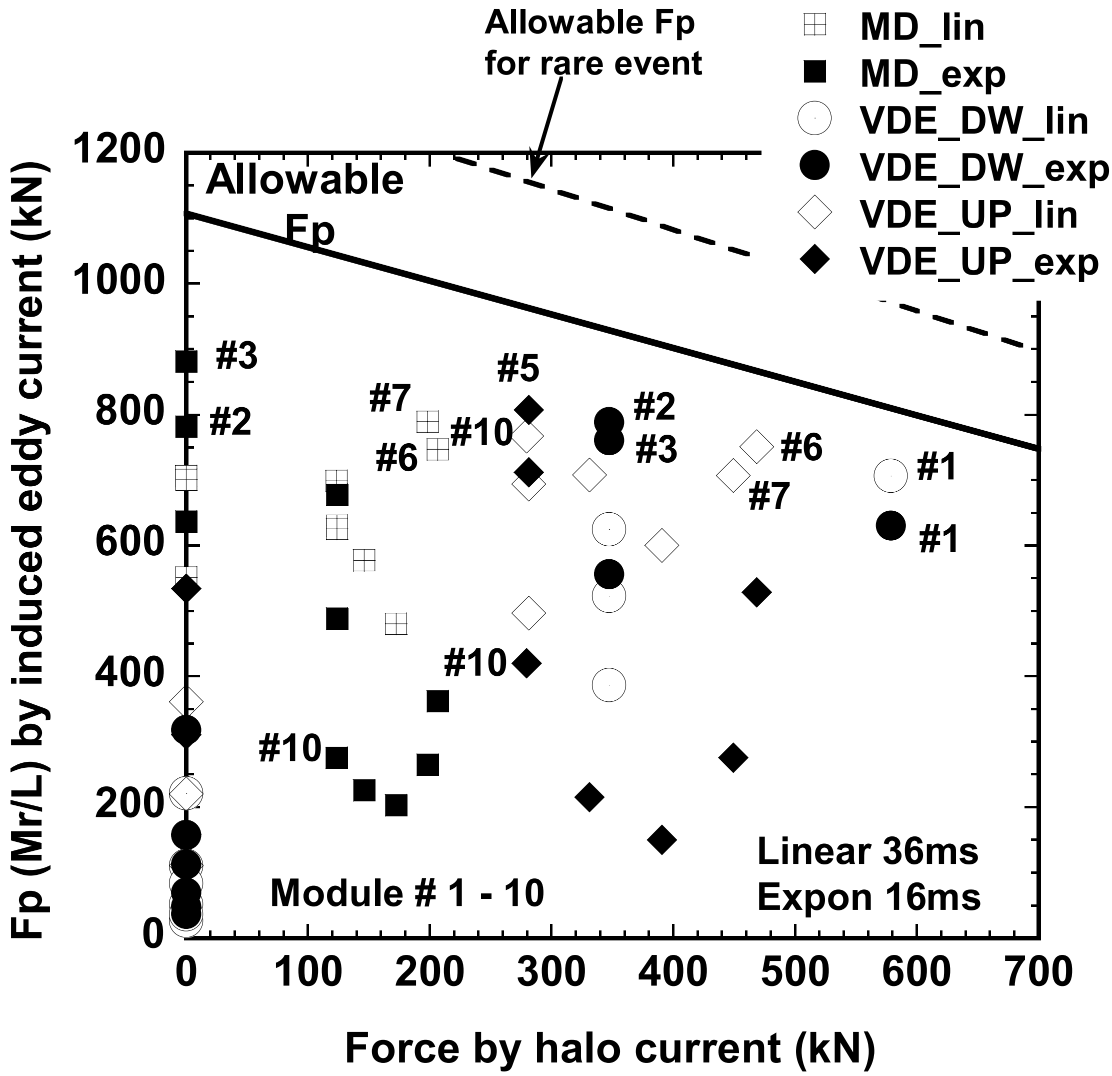

Figure 2.3
Maximum poloidal (vertical) forces F_p due to the induced eddy and halo currents on #1-10 BMs for representative scenarios of MDs (MD_lin and MD_exp) and upward/downward VDEs (VDE_UP_lin, VDE_UP_exp, VDE_DW_lin and VDE_DW_exp) with a fast current quench (*36* ms quench time for the linear waveform and *16* ms time constant for the exponential waveform), respectively.

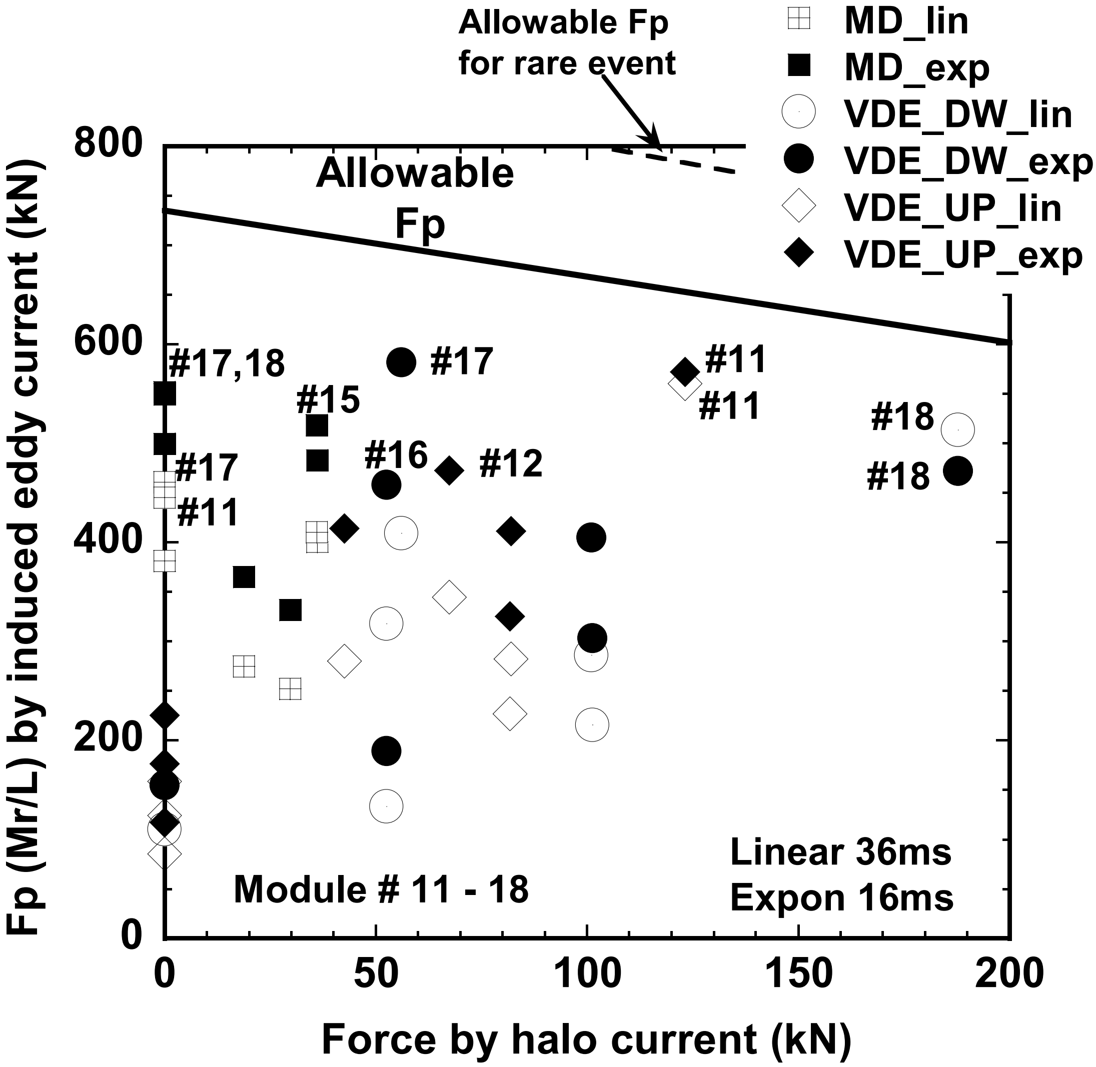

Figure 2.4
Maximum poloidal (vertical) forces F_p due to the induced eddy and halo currents on #11-18 BMs for representative scenarios of MDs (MD_lin and MD_exp) and upward/downward VDEs (VDE_UP_lin, VDE_UP_exp, VDE_DW_lin and VDE_DW_exp) with a fast current quench (*36* ms quench time for the linear waveform and *16* ms time constant for the exponential waveform), respectively.

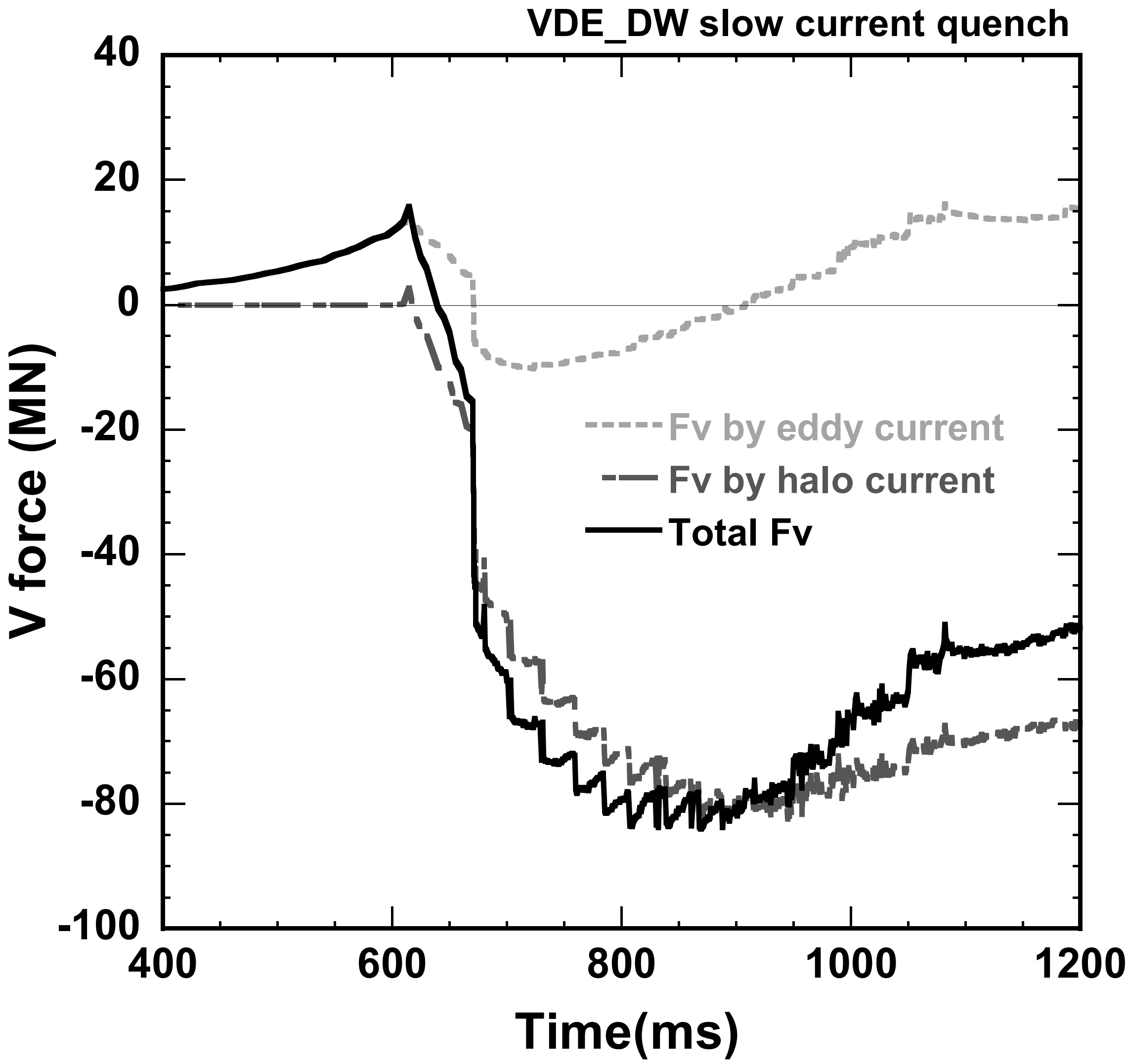

Figure 2.5
Time evolutions of the vertical forces on the VV due to halo (dashed line) and eddy (dotted line) currents as well as the total force (solid line) for the case of downward VDE with slow current quench shown in Fig. 1.10 (a) and (b)

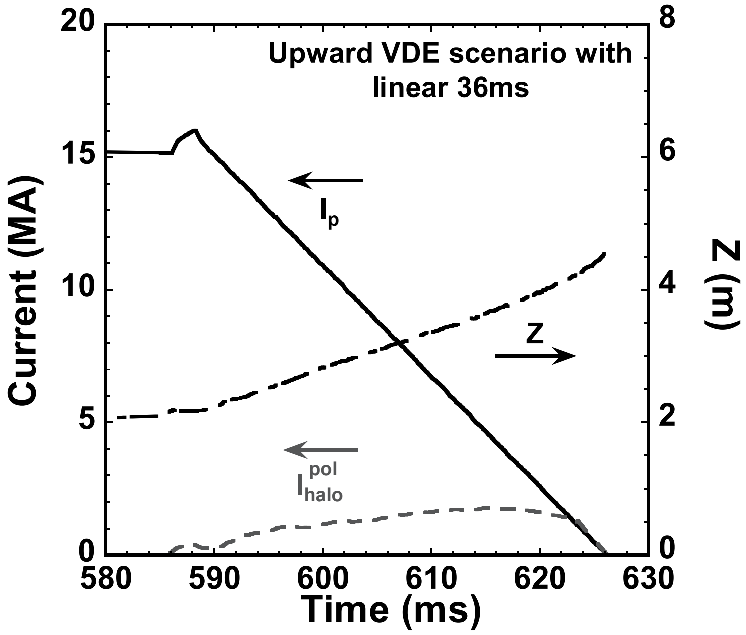

Figure 2.6
Waveform of plasma current Ip, vertical position of plasma current center Z and total poloidal halo current I_{halo}^{pol} for VDE with fast current decay (*36ms*)

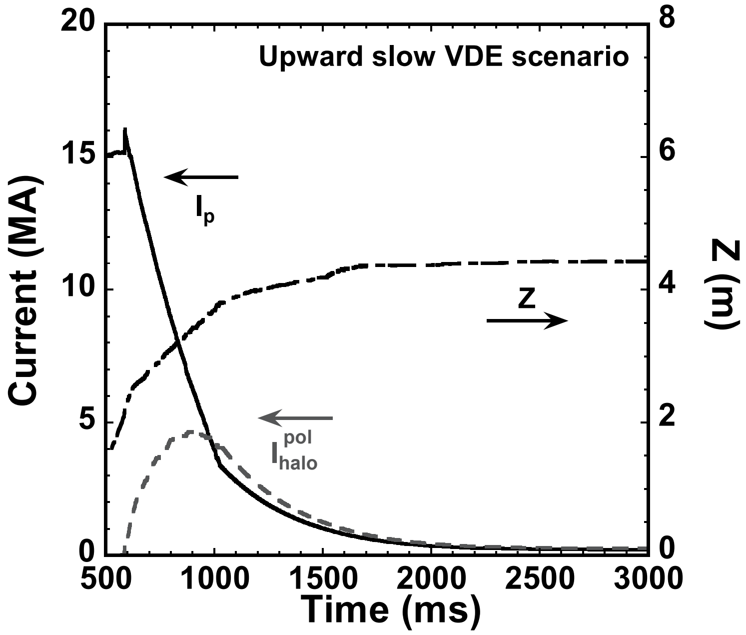

Figure 2.7
Waveform of plasma current Ip, vertical position of plasma current center Z and total poloidal halo current I_{halo}^{pol} for VDE with slow current decay (*≈600ms*)

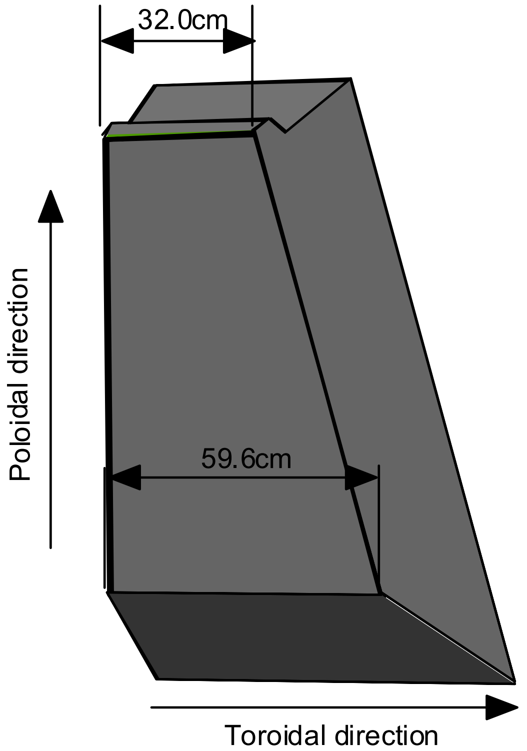

Figure 2.8
Real geometry of port plug

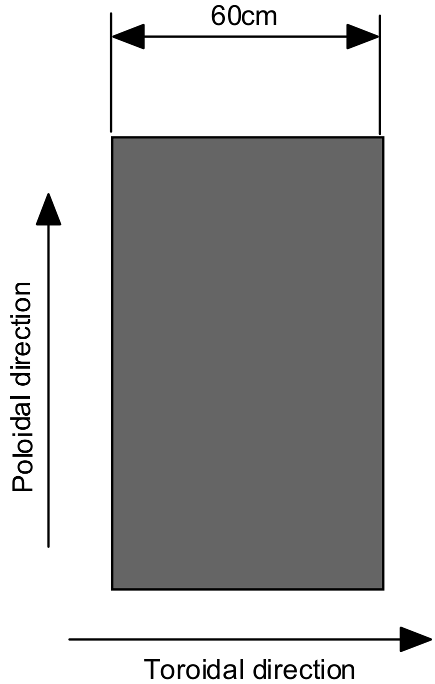

Figure 2.9
Geometry of port plug used in this analysis

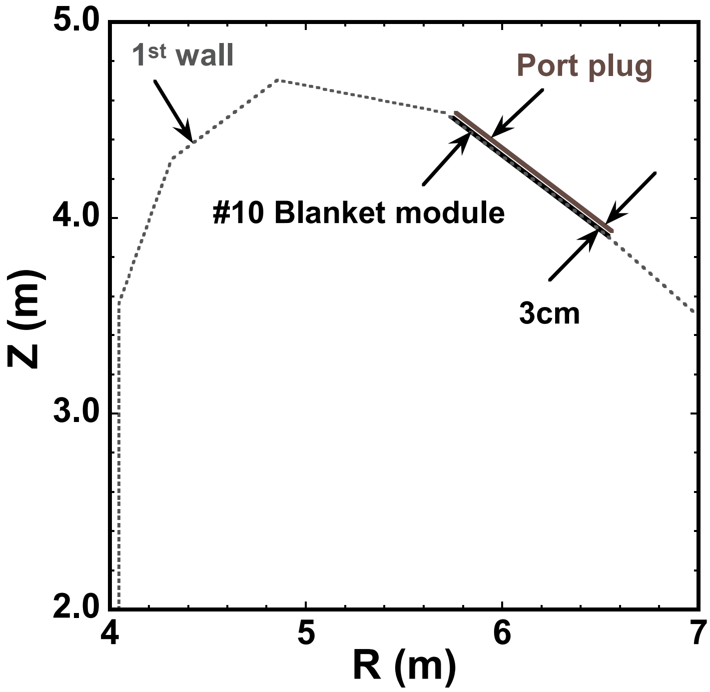

Figure 2.10
Configuration of the first wall, blanket module and port plug on poloidal cross-section

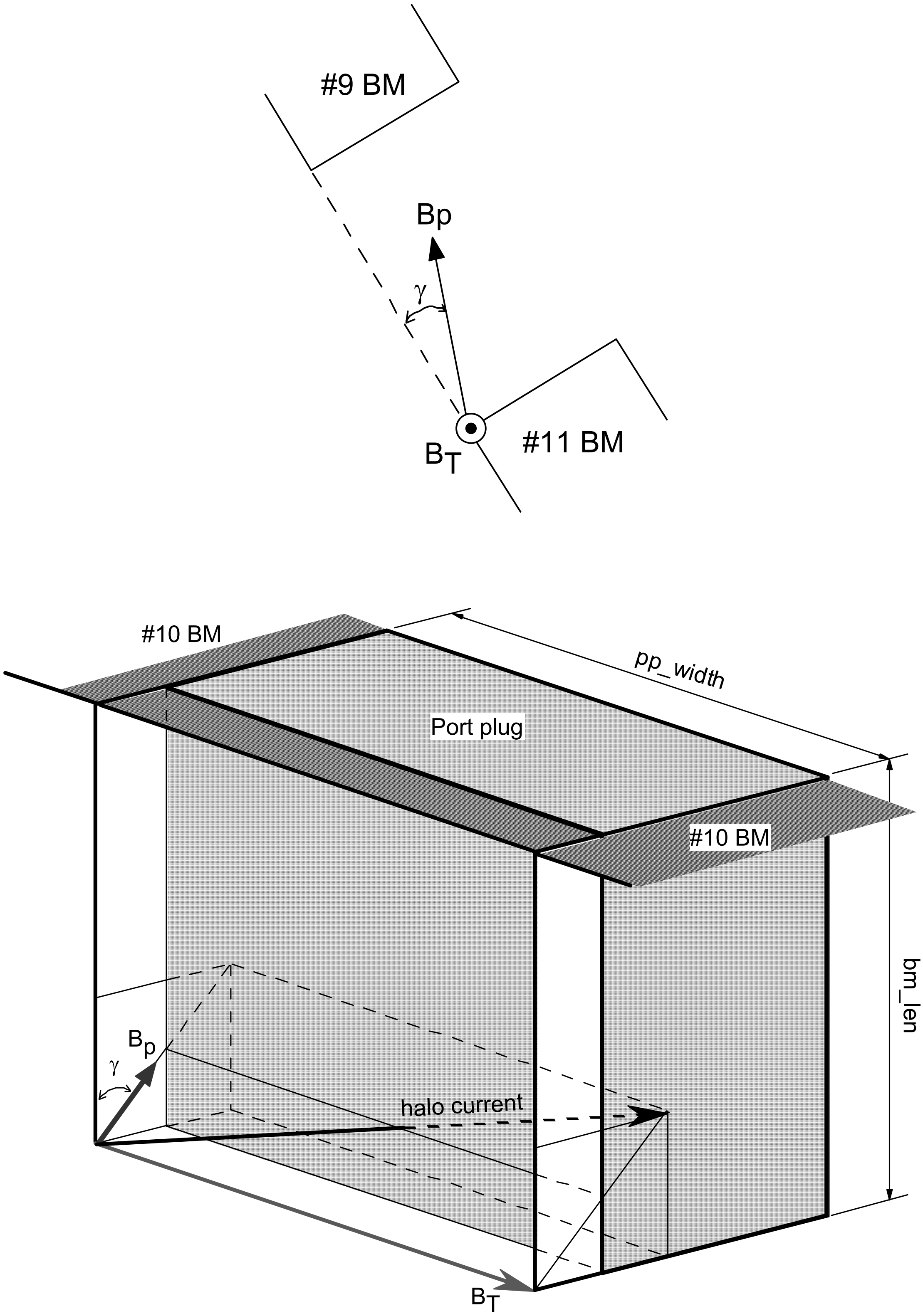

Figure 2.11
Flow path of halo current into port plug

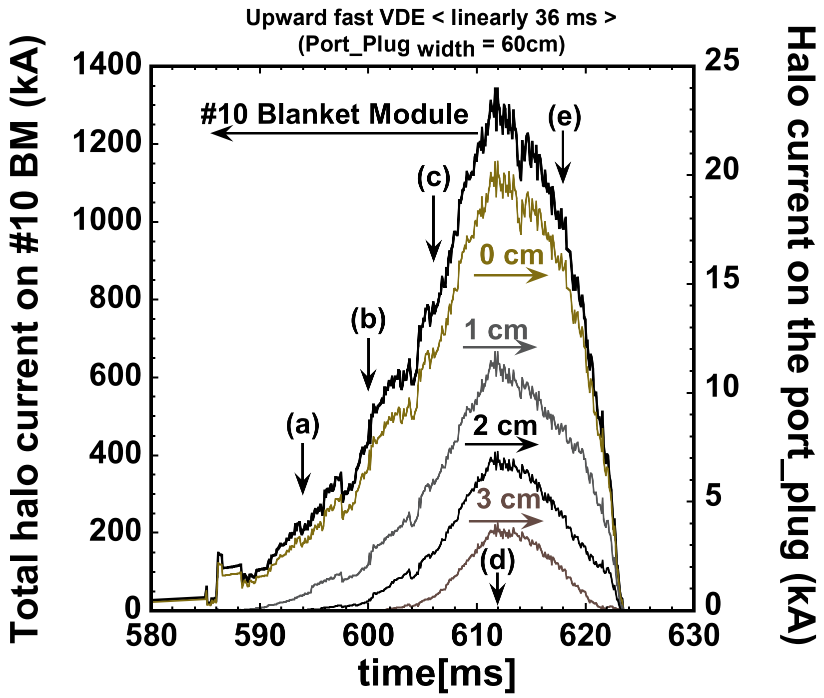

Figure 2.12
Time evolution of halo current flowing into PP for recessed distance *0cm* (no recess), *1cm*, *2cm* and *3cm* during VDE with fast current decay. Total halo current flowing to #10 BMs (toroidally summed up including PP) is also shown in black.

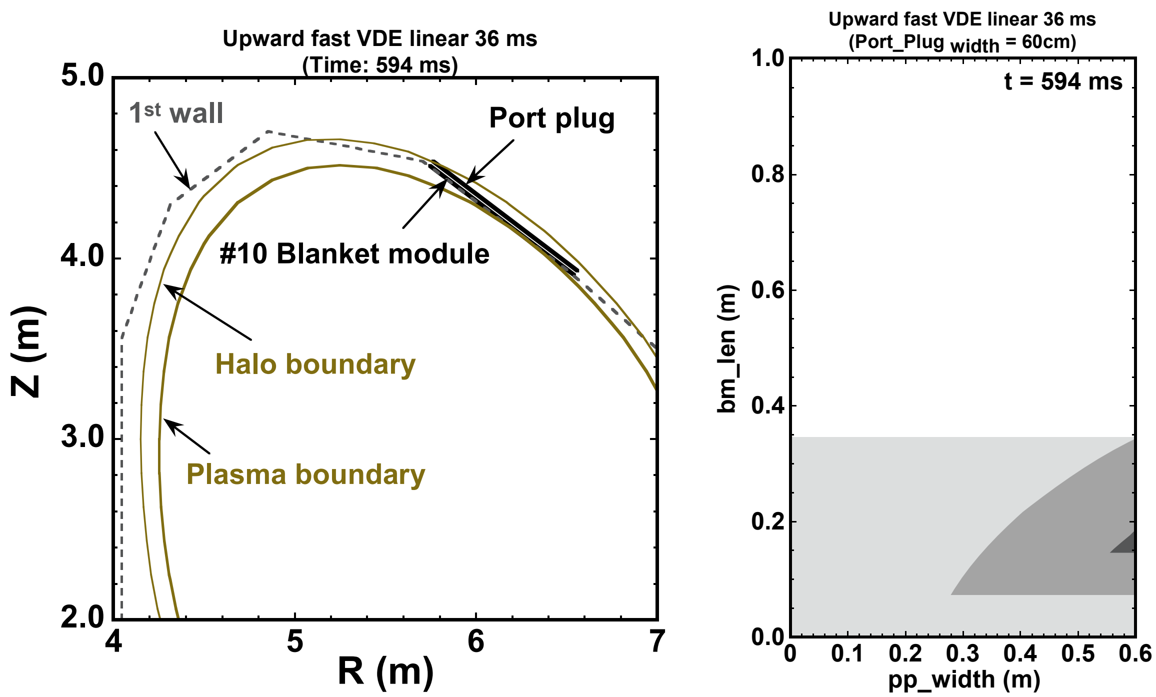

Figure 2.13
(Left): Plasma and halo boundaries at *594ms* (shown by (a) in Fig. 2.12).
(Right): Area on PP, where the halo current flows, at time moment (a) for each recessed distance, *0cm* (light gray), *1cm* (gray), *2cm* (dark grey), respectively.

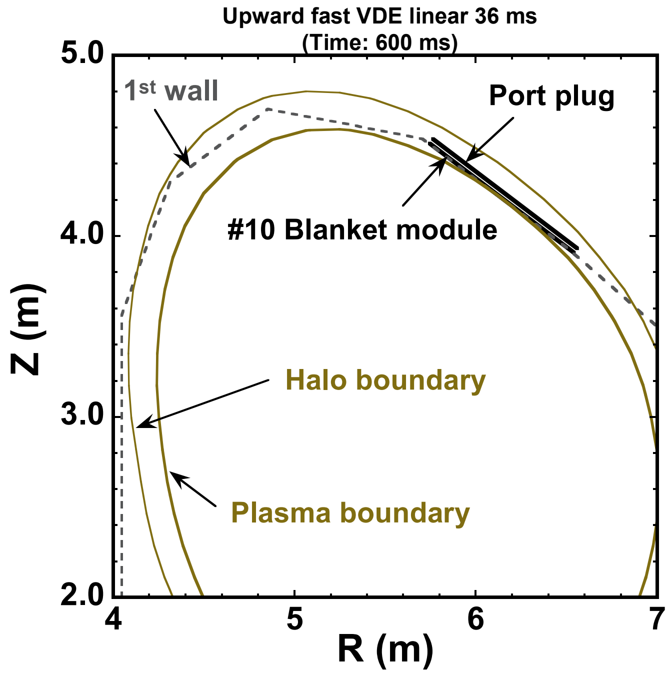

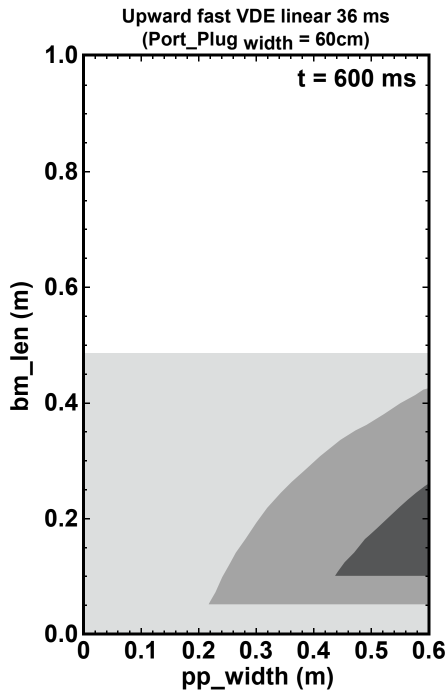

Figure 2.14
(Left): Plasma and halo boundaries at *600ms* (shown by (b) in Fig. 2.12).
(Right): Area on PP, where the halo current flows, at time moment (b) for each recessed distance, *0cm* (light gray), *1cm* (gray), *2cm* (dark gray), respectively.

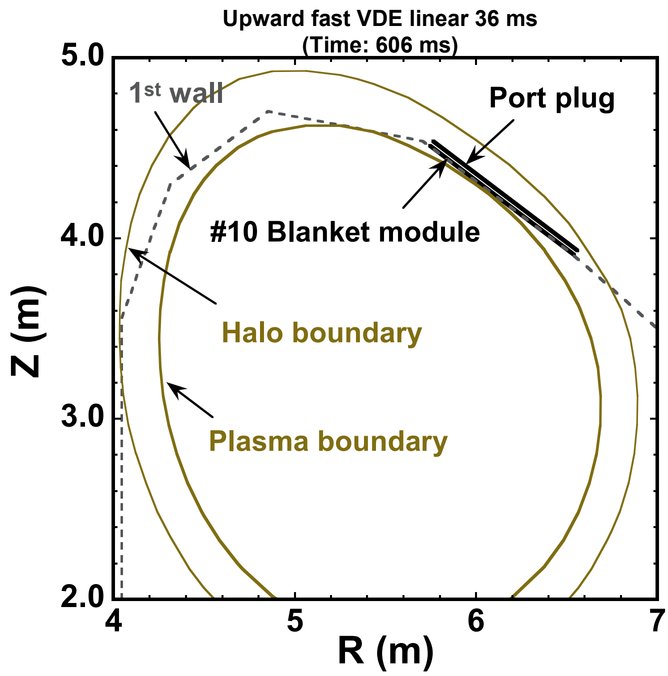

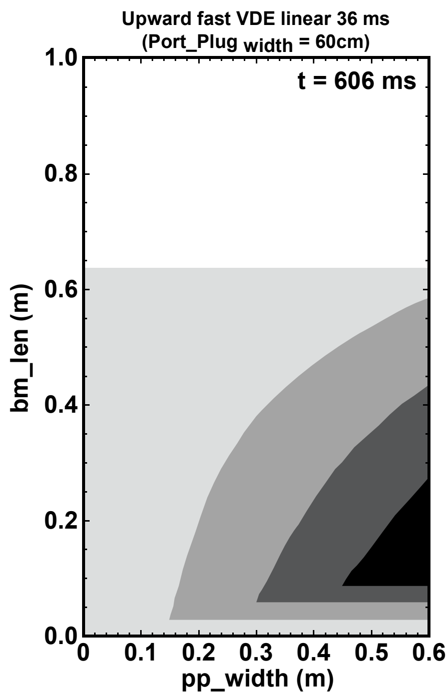

Figure 2.15
(Left): Plasma and halo boundaries at *606ms* (shown by (c) in Fig. 2.12).
(Right): Area on PP, where the halo current flows, at time moment (c) for each recessed distance, *0cm* (light gray), *1cm* (gray), *2cm* (dark gray) and *3cm* (black), respectively.

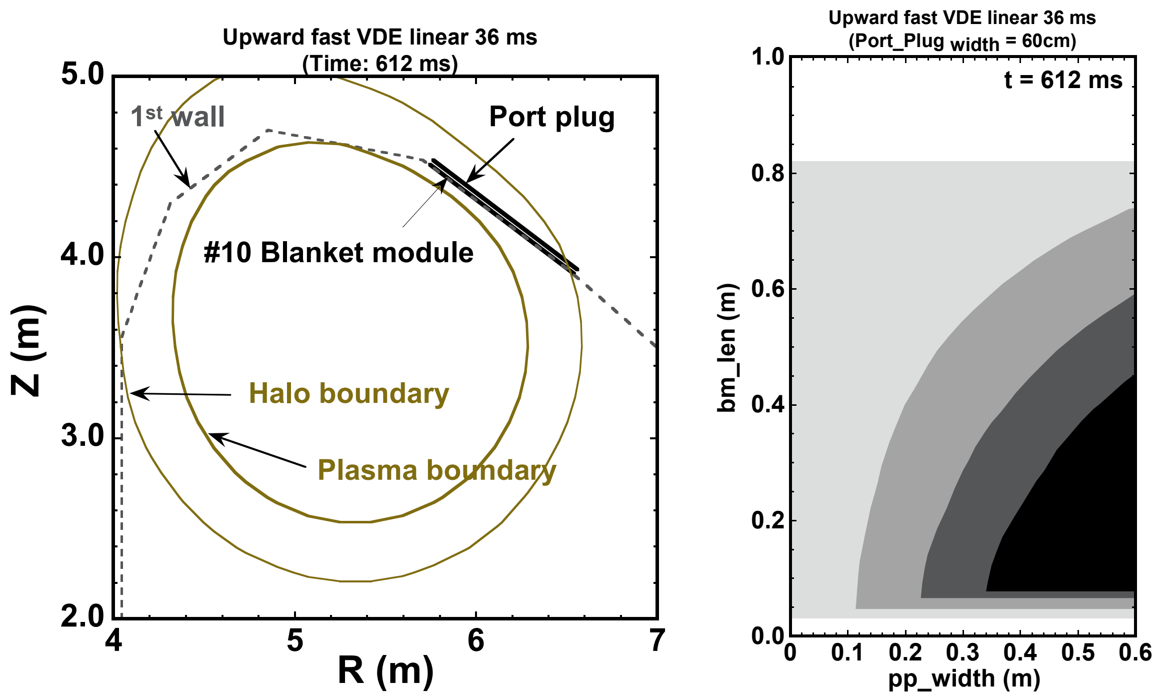

Figure 2.16
(Left): Plasma and halo boundaries at *612ms* (shown by (d) in Fig. 2.12).
(Right): Area on PP, where the halo current flows, at time moment (d) for each recessed distance, *0cm* (light gray), *1cm* (gray), *2cm* (dark gray) and *3cm* (black), respectively.

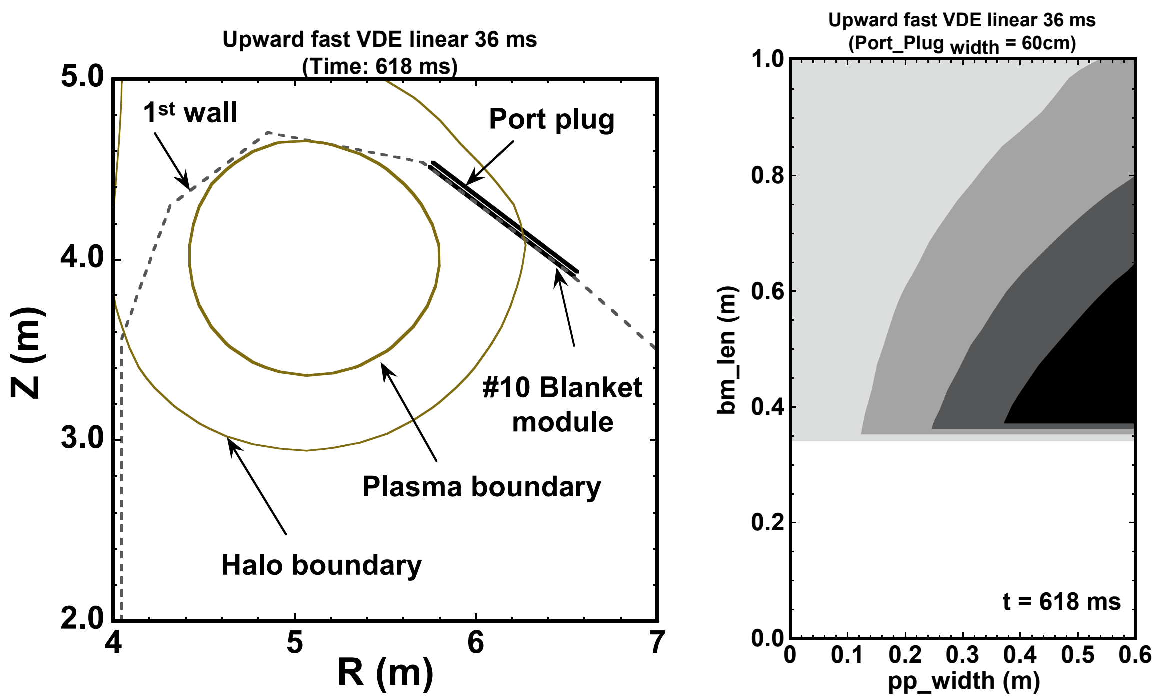

Figure 2.17
(Left): Plasma and halo boundaries at *618ms* (shown by (e) in Fig. 2.12).
(Right): Area on PP, where the halo current flows, at time moment (e) for each recessed distance, *0cm* (light gray), *1cm* (gray), *2cm* (dark gray) and *3cm* (black), respectively.

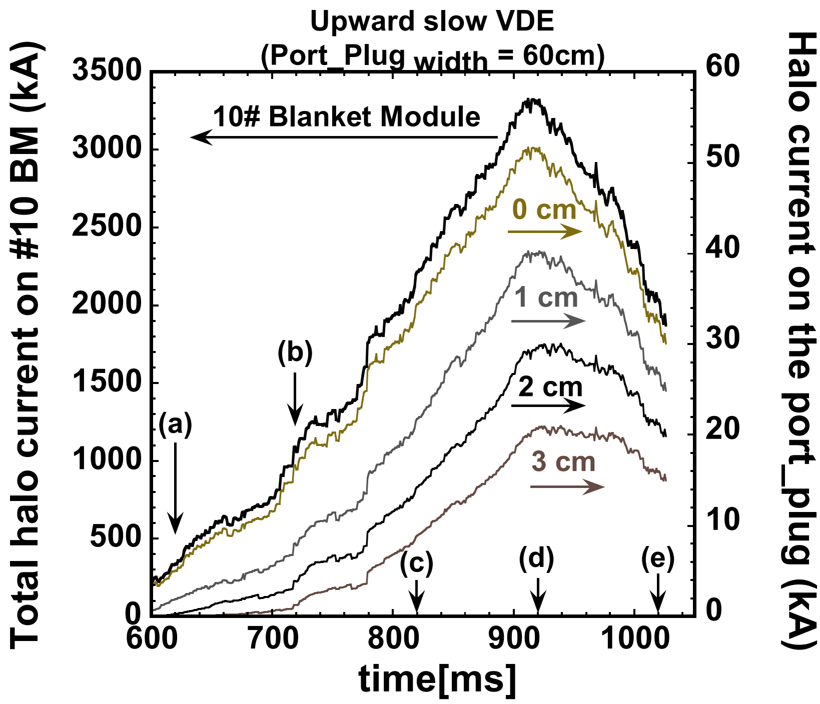

Figure 2.18
Time evolution of halo current flowing into PP for recessed distance *0cm* (no recess), *1cm*, *2cm* and *3cm* during VDE with slow current decay. Total halo current flowing to #10 BMs (toroidally summed up including PP) is also shown in black.

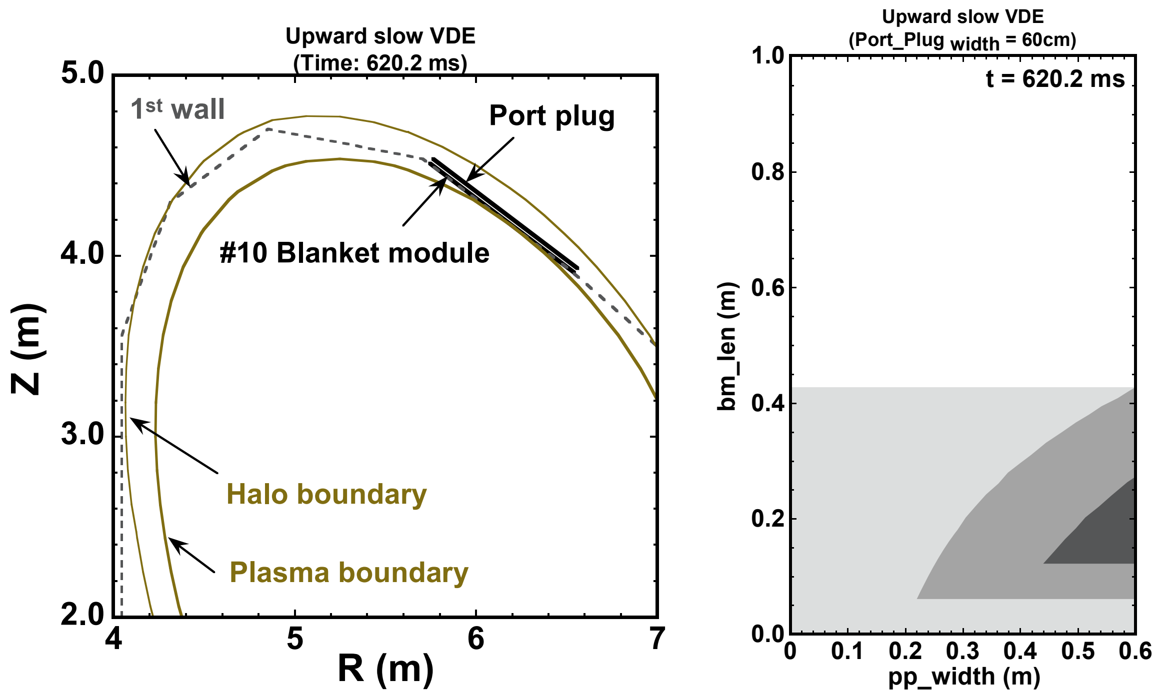

Figure 2.19
(Left): Plasma and halo boundaries at *620ms* (shown by (a) in Fig. 2.18).
(Right): Area on PP, where the halo current flows, at time moment (a) for each recessed distance, *0cm* (light gray), *1cm* (gray), *2cm* (dark gray), respectively.

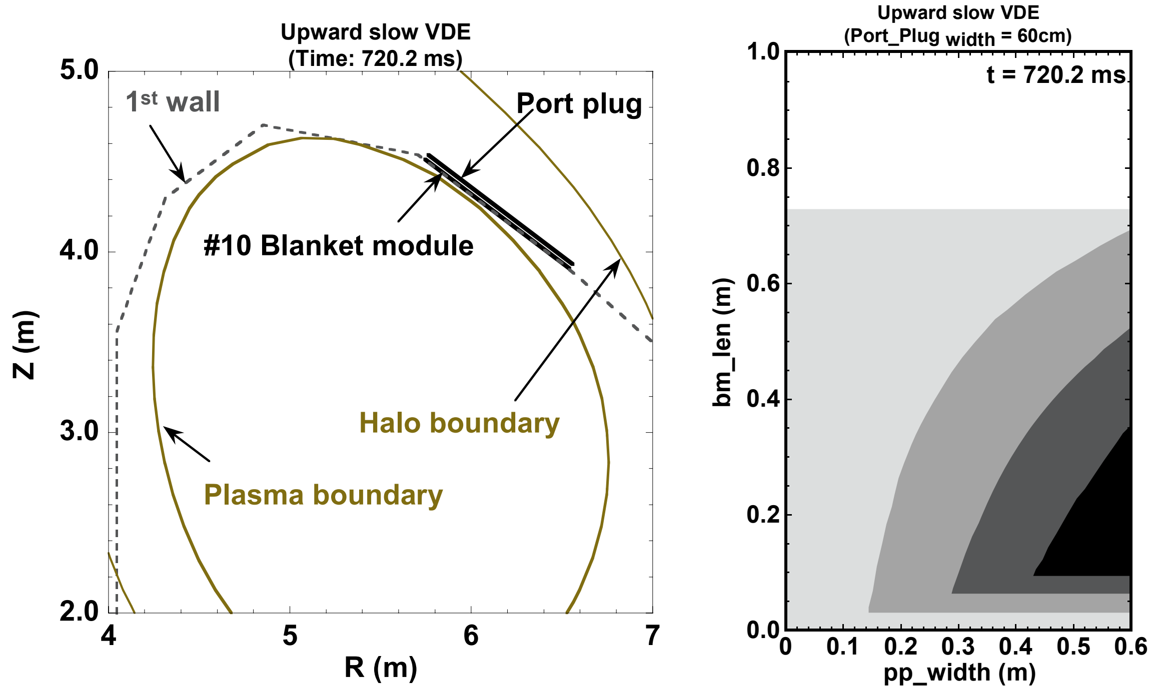

Figure 2.20

(Left): Plasma and halo boundaries at *720ms* (shown by (b) in Fig. 2.18).
(Right): Area on PP, where the halo current flows, at time moment (b) for each recessed distance, *0cm* (light gray), *1cm* (gray), *2cm* (dark gray) and *3cm* (black), respectively.

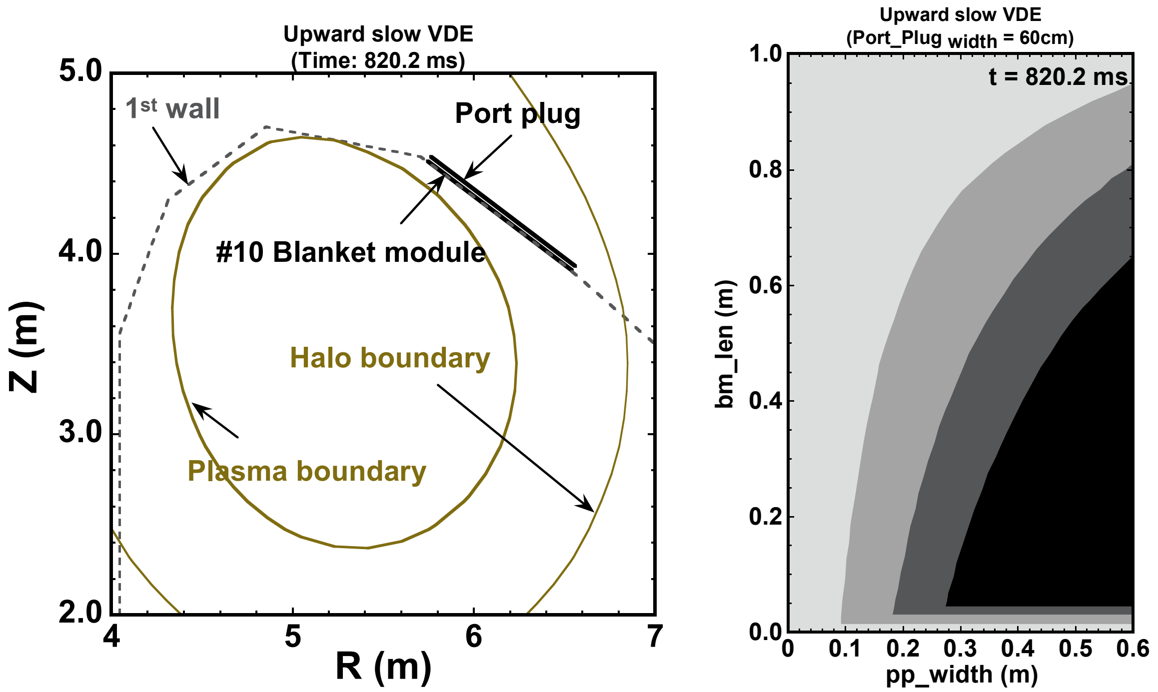

Figure 2.21

(Left): Plasma and halo boundaries at *820ms* (shown by (c) in Fig. 2.18).
(Right): Area on PP, where the halo current flows, at time moment (c) for each recessed distance, *0cm* (light gray), *1cm* (gray), *2cm* (dark gray) and *3cm* (black), respectively.

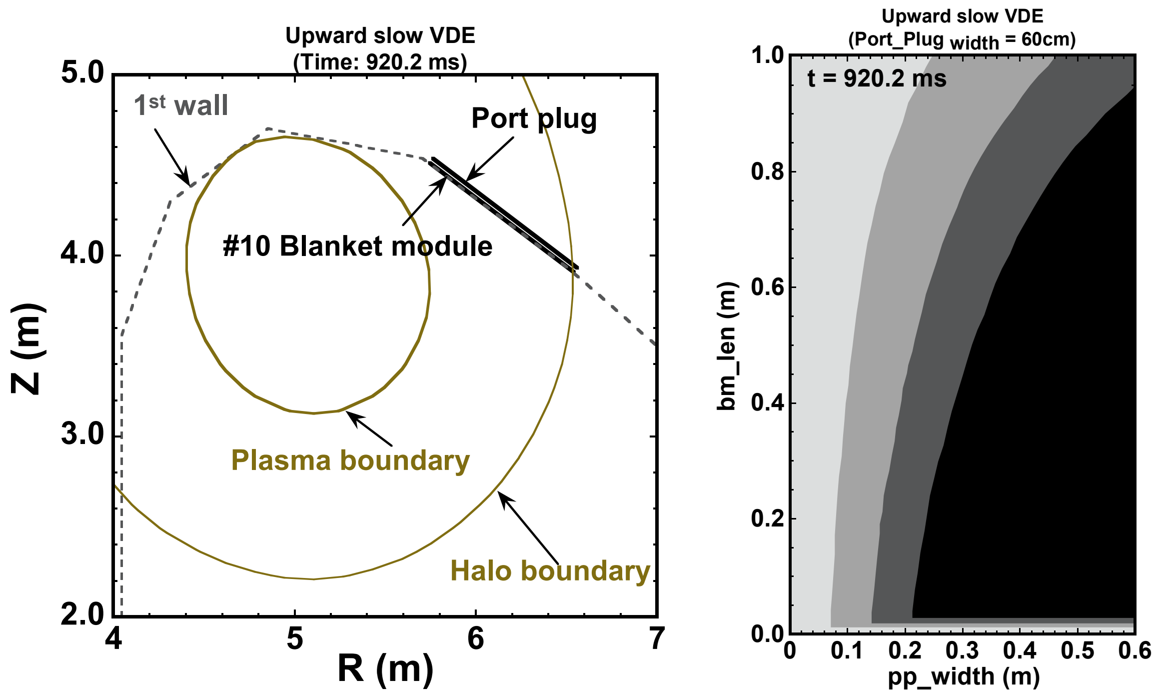

Figure 2.22
(Left): Plasma and halo boundaries at *920ms* (shown by (d) in Fig. 2.18).
(Right): Area on PP, where the halo current flows, at time moment (d) for each recessed distance, *0cm* (light gray), *1cm* (gray), *2cm* (dark gray) and *3cm* (black), respectively.

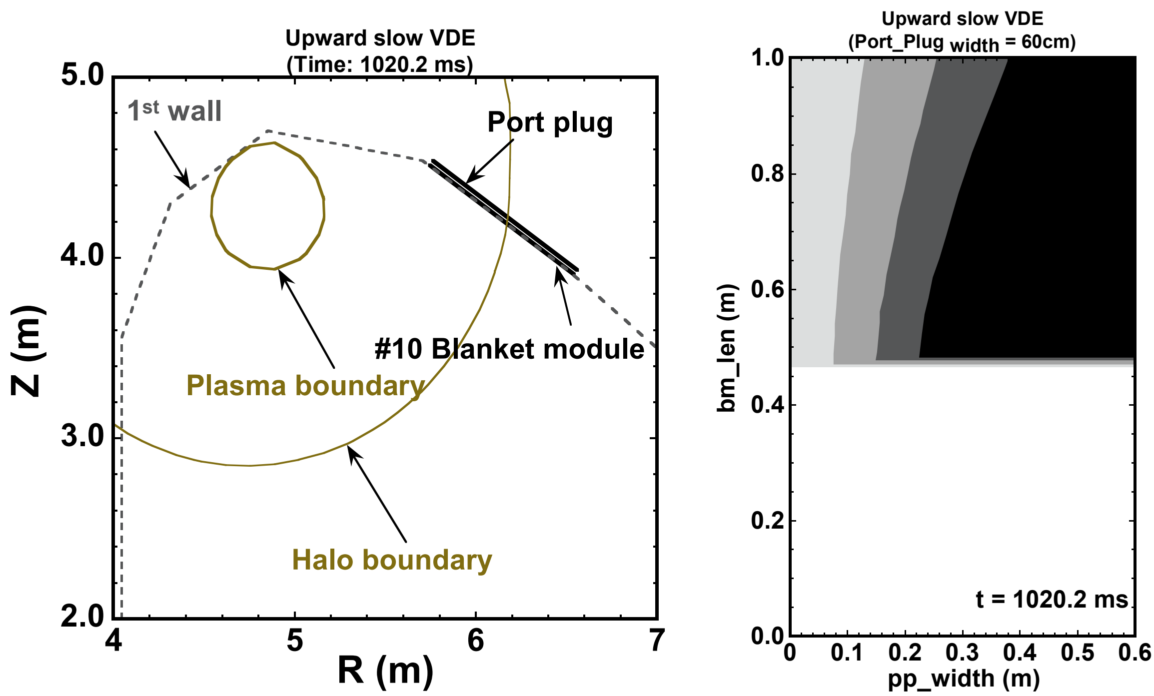

Figure 2.23
(Left): Plasma and halo boundaries at *1020ms* (shown by (e) in Fig. 2.18).
(Right): Area on PP, where the halo current flows, at time moment (e) for each recessed distance, *0cm* (light gray), *1cm* (gray), *2cm* (dark gray) and *3cm* (black), respectively.

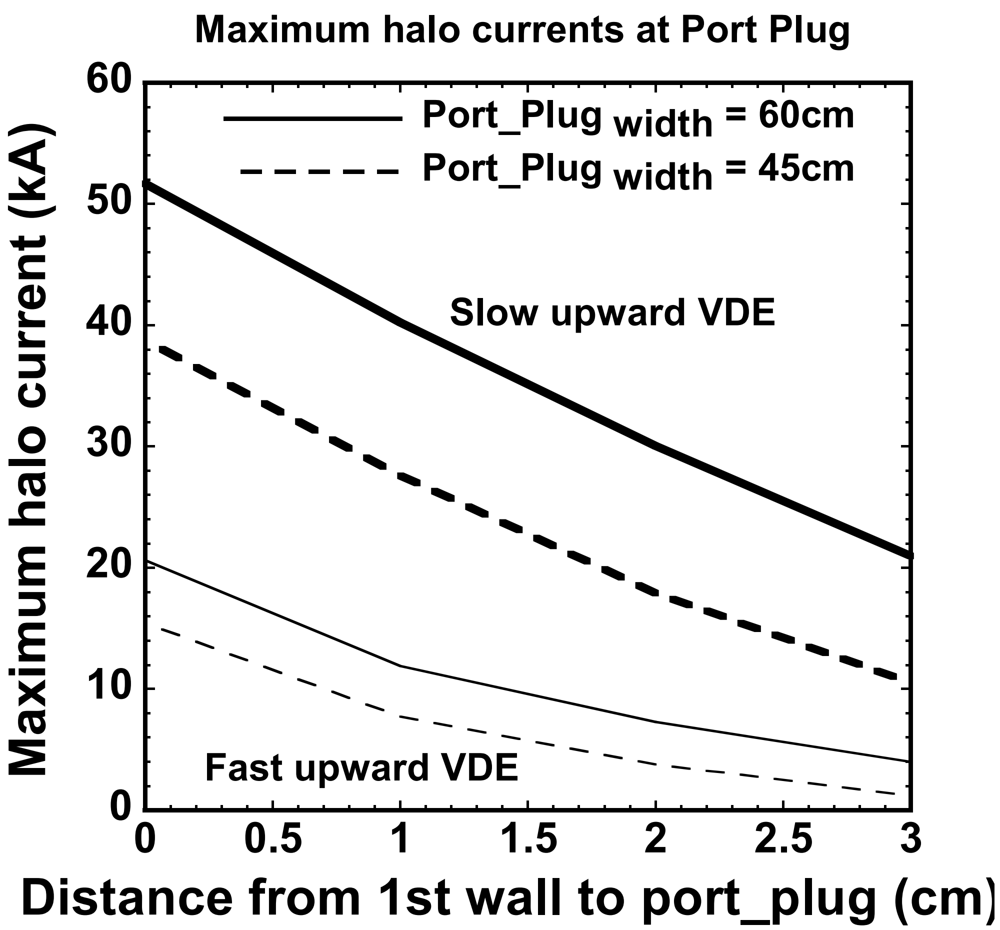

Figure 2.24
Maximum halo current flowing into PP as a function of recessed distance for fast (thin solid line) and slow (bold solid line) current decay. Dotted lines show the maximum halo current for the case of PP with *45cm* toroidal length.

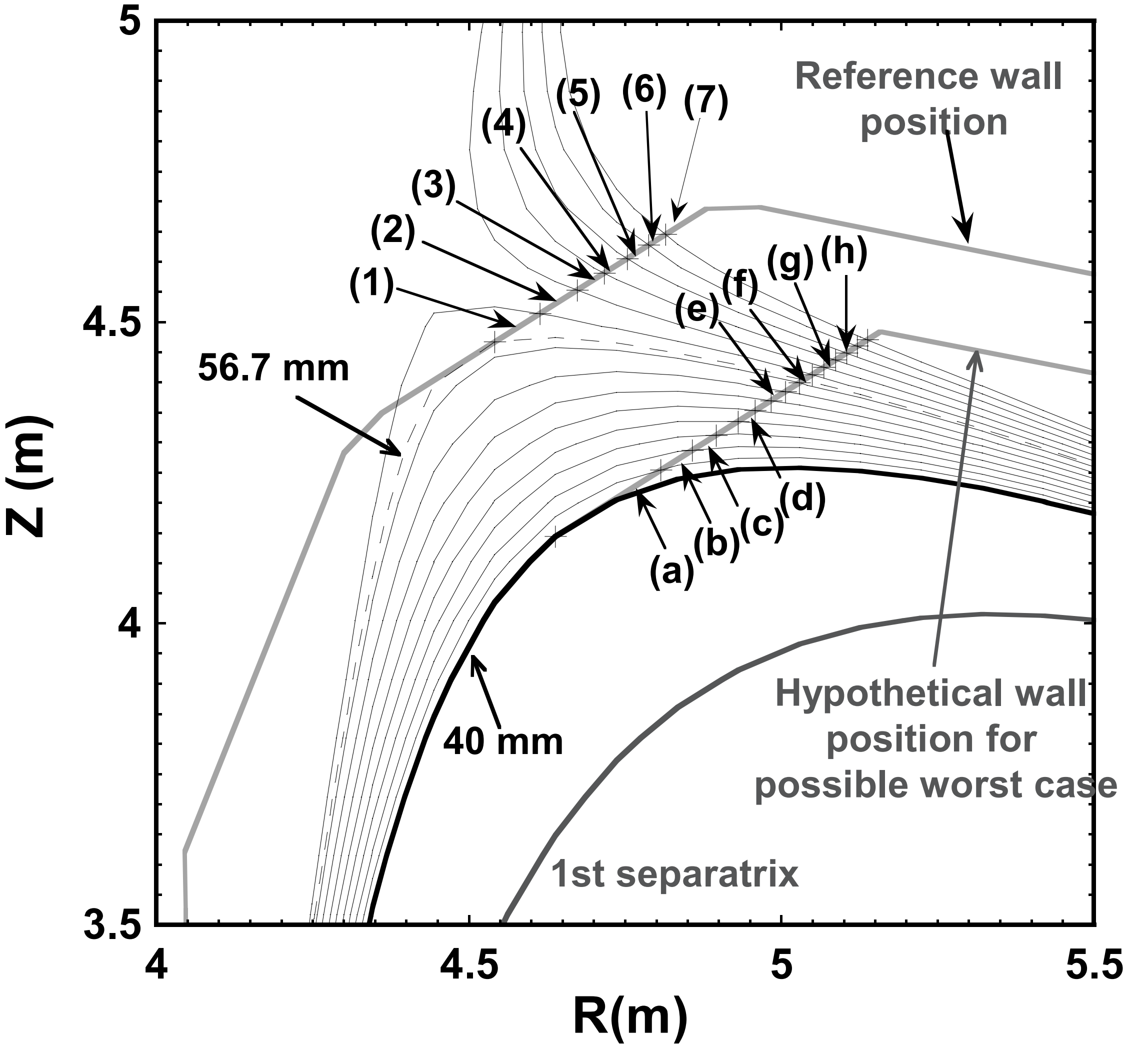

Figure 3.1
Flux surfaces near the upper wall from the equilibrium calculation for the case of the reference inductive scenario. Flux lines of every *2 mm* beyond *40 mm* from the first separatrix are depicted and the intersecting region with the upper wall are indicated as (1)-(7). Hypothetical wall position is also shown as a possible worst case. The intersecting regions of these flux surfaces with the hypothetical wall are indicated as (a)-(h).

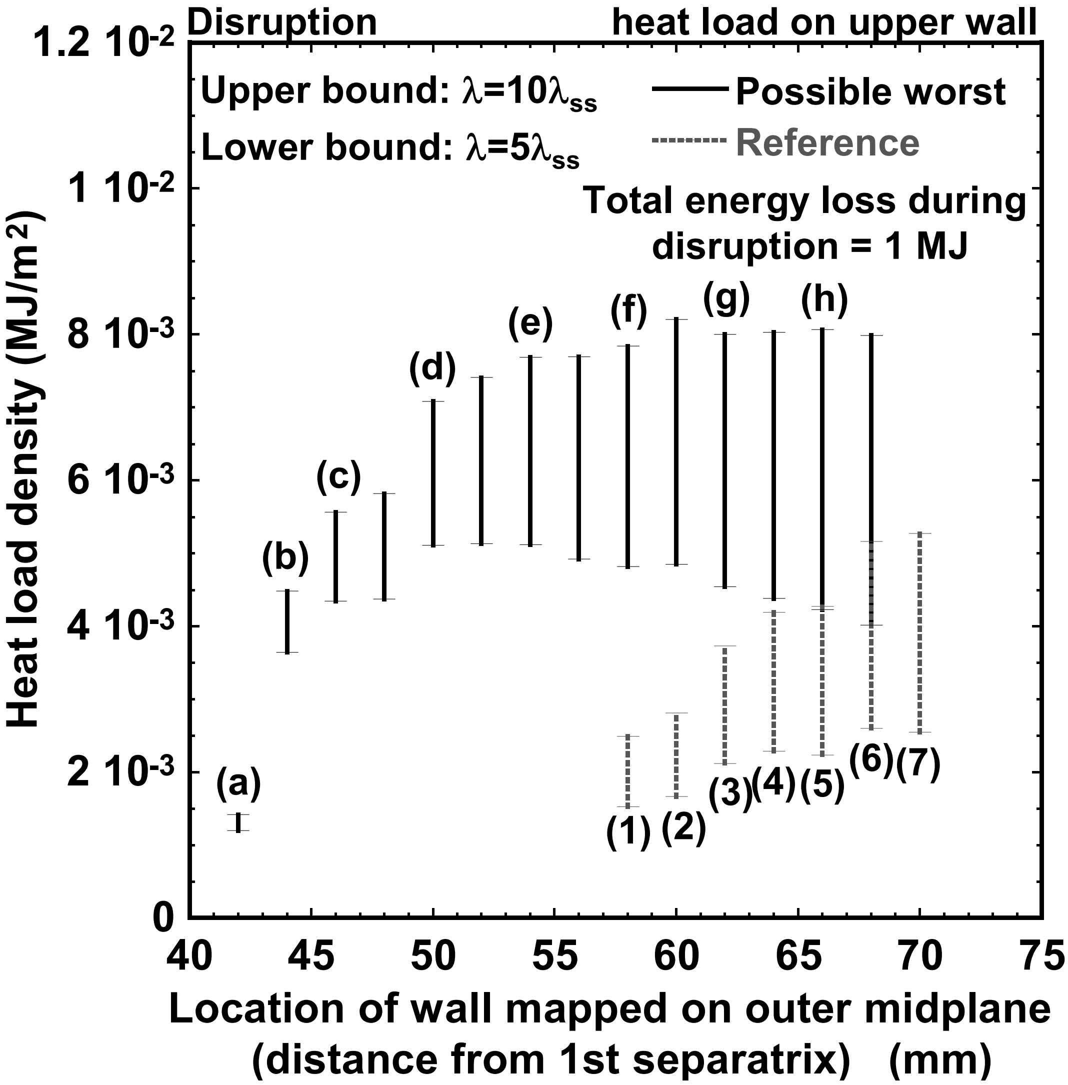

Figure 3.2
Range of heat load density on the upper wall during the TQ of MDs for the reference (dotted line) and the possible worst (solid line) equilibrium configurations (W_{peak} =1MJ and λss =5 mm are assumed). Upper and lower bound correspond to the expansion factor of λss (5 corresponds to lower and 10 to upper).

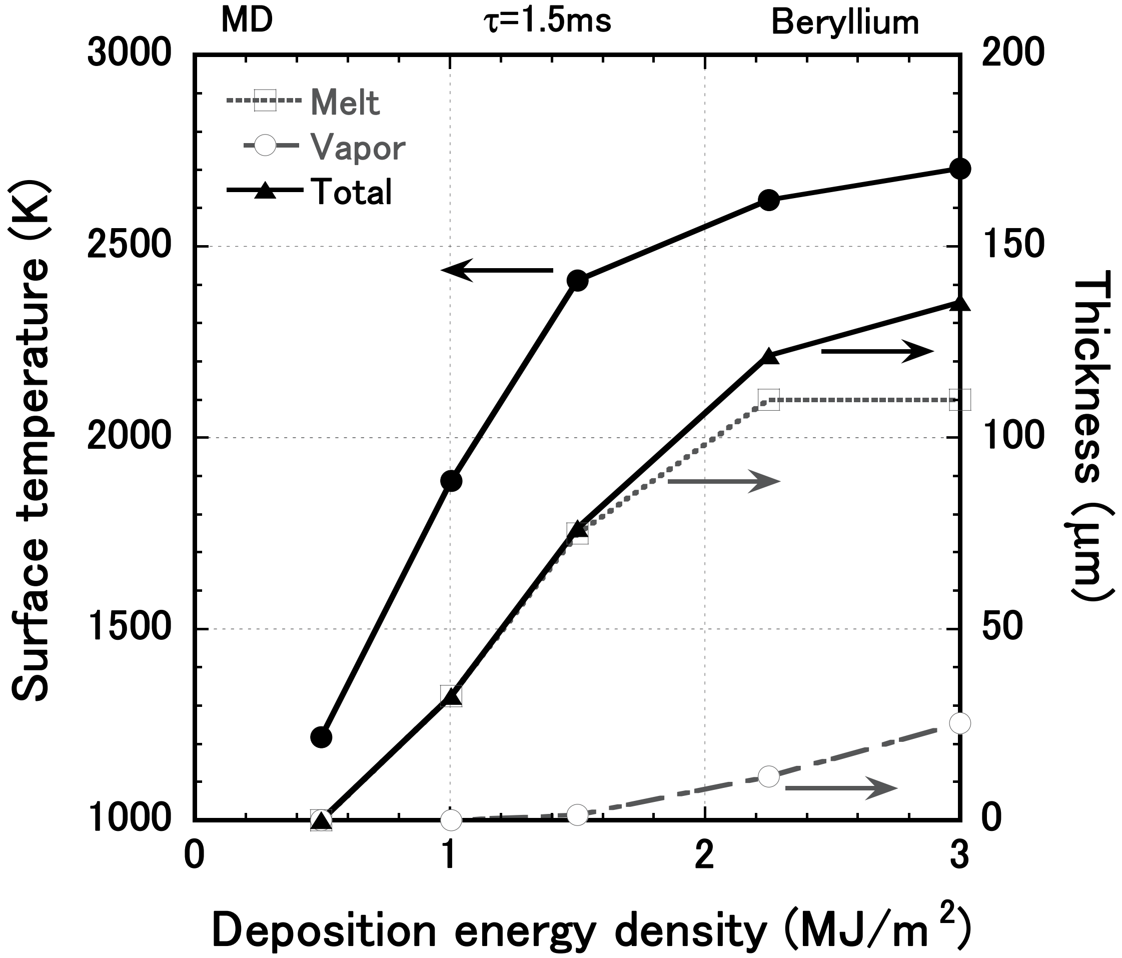

Figure 3.3
Maximum surface temperature (closed circles) and thicknesses of melt layer (open squares), vaporized layer (open circles) and total (closed triangles) as a function of deposition energy density on the upper first wall during the TQ of MDs calculated with 2D heat conduction code. Time duration of energy deposition is assumed *1.5 ms*.

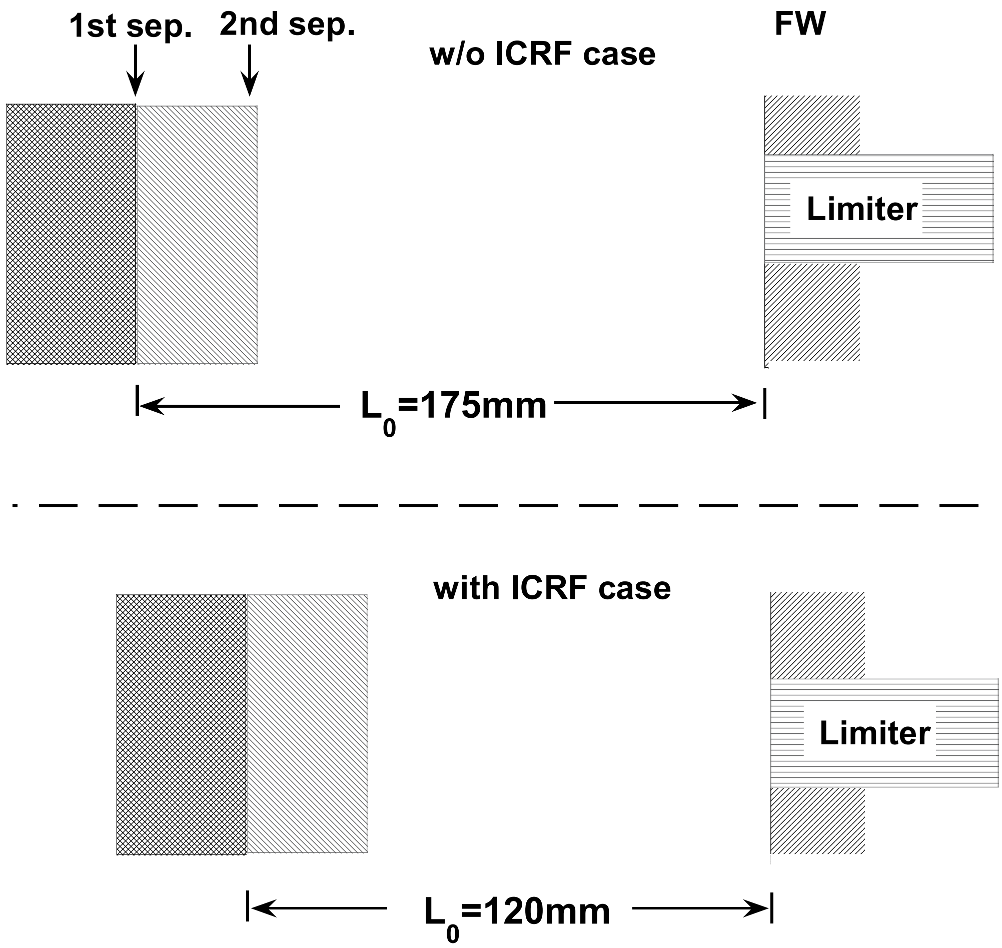

Figure 3.4
Location of 1st and 2nd separatixes and wall/limiter for with and w/o ICRF heating case. Distance between the 1st separatrix and the wall is expressed by L_0.

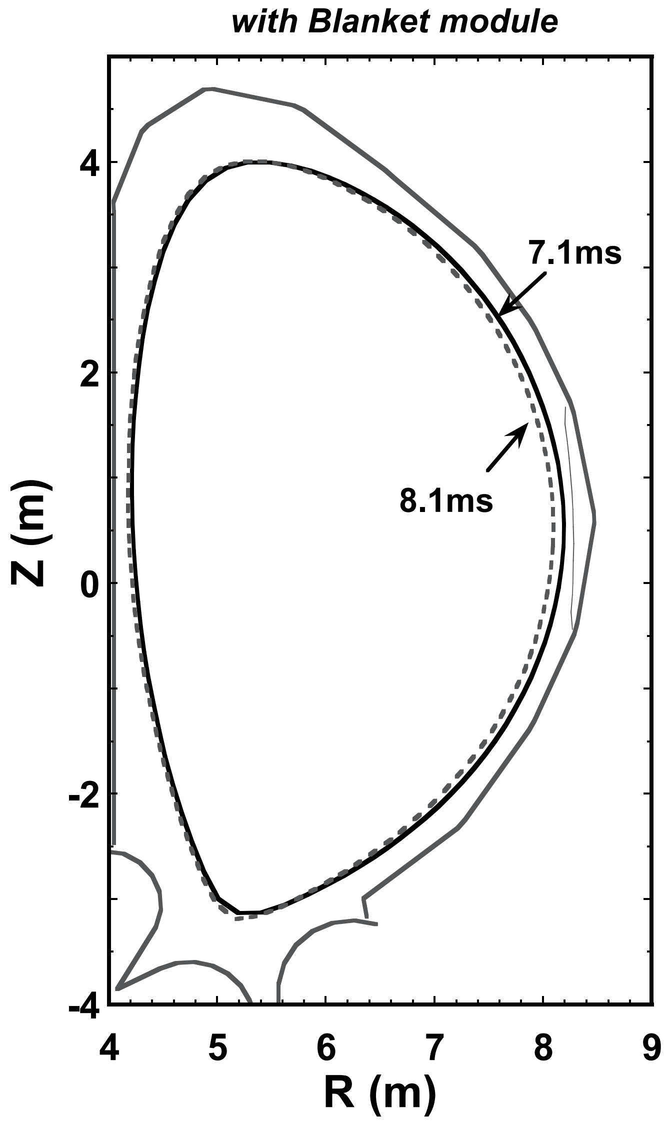

Figure 3.5
Position of separatrix just before (solid line; *7.1 ms*) and after (dotted line; *8.1 ms*) beta drop during TQ in MDs

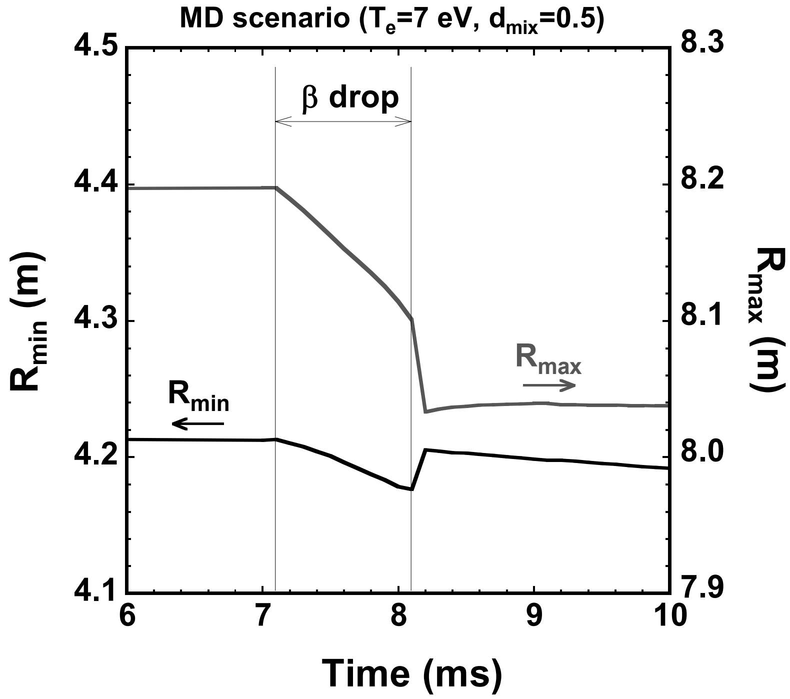

Figure 3.6
Time behavior of radial position of the outer-most (R_{max}) and inner-most (R_{min}) flux surfaces after the TQ in MDs

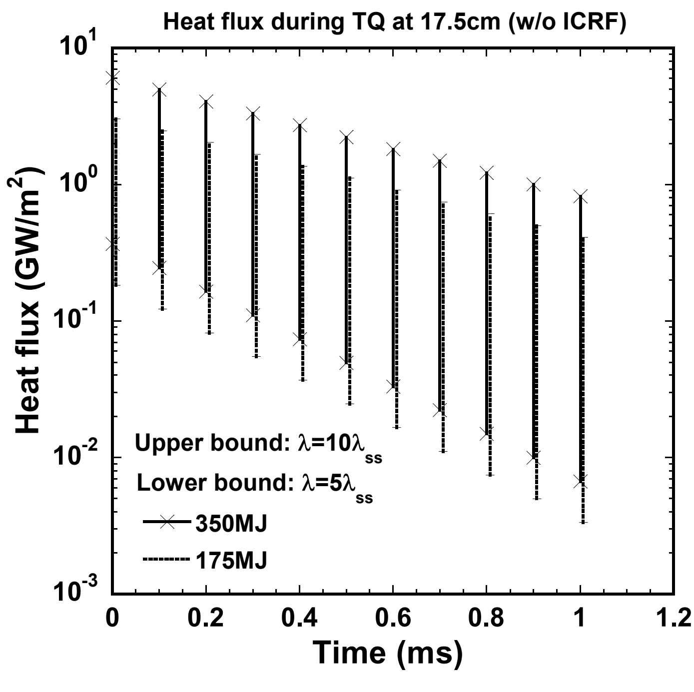

Figure 3.7
Time behavior of the heat flux along field line at *17.5 cm* from the first separatrix (w/o ICRF case) during the TQ in MDs for two cases of the total energy loss of *350 MJ* and *175 MJ*. Upper and lower bounds correspond to the expansion of the heat flux width (10 for upper and 5 for lower).

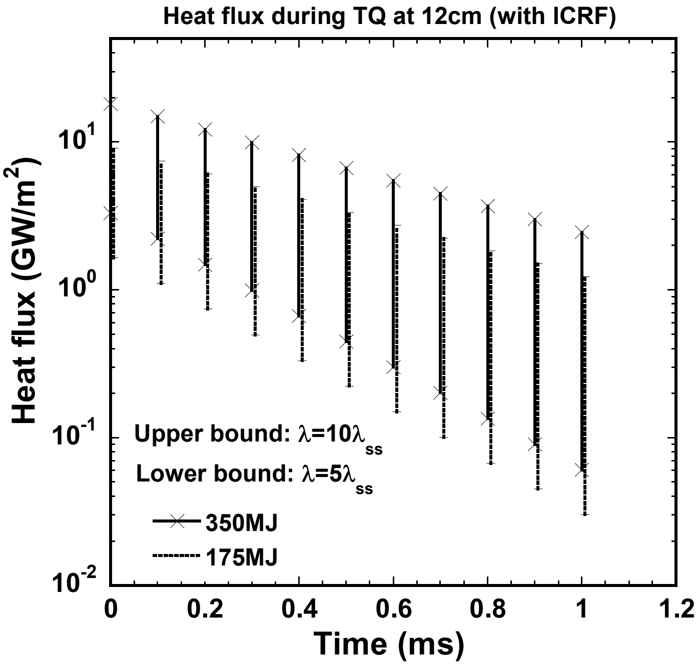

Figure 3.8
Time behavior of the heat flux along field line at *12 cm* from the first separatrix (with ICRF case) during the TQ in MDs for two cases of the total energy loss of *350 MJ* and *175 M*. Upper and lower bounds correspond to the expansion of the heat flux width (10 for upper and 5 for lower).

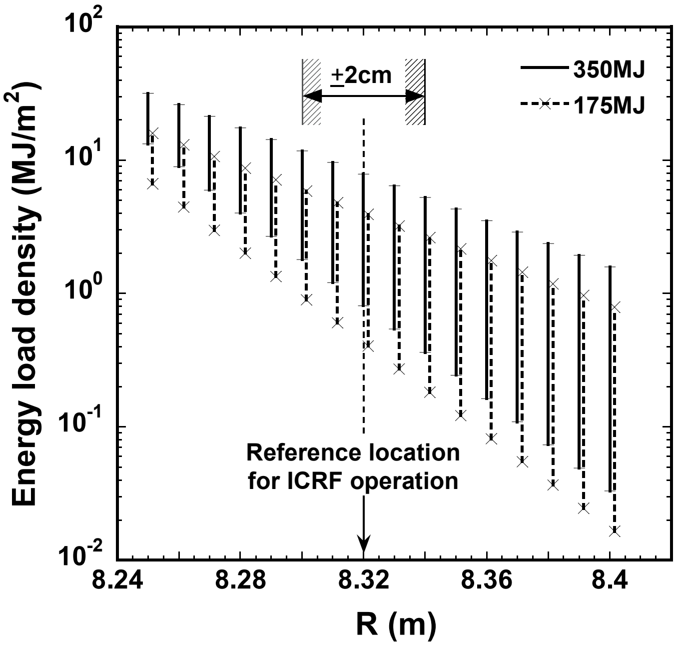

Figure 3.9
Total energy load density for various values of L_0 during energy deposition time (*1 ms*) obtained by integrating the heat flux (for the cases of L_0 =*17.5 cm* and *12 cm* provided in Figs 3.7 and 3.8).

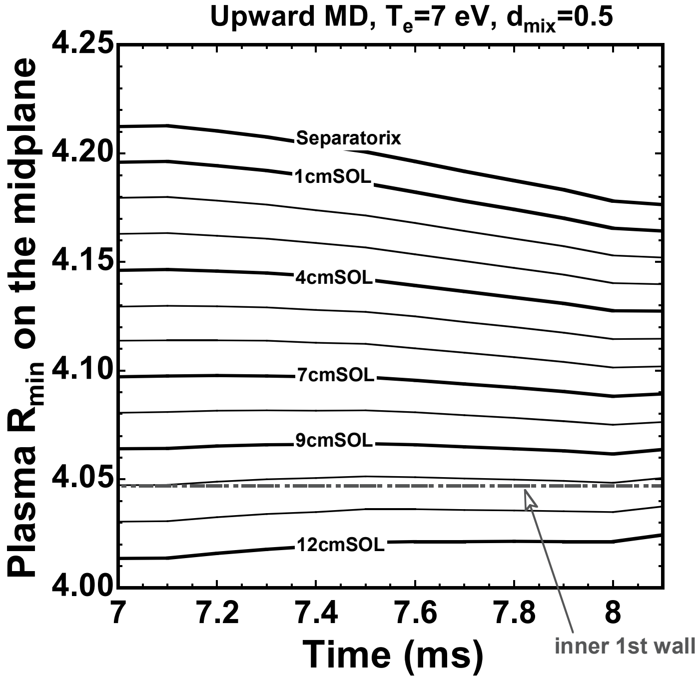

Figure 3.10
Movement of the corresponding flux surfaces at the inner region away from the separatrix by the specified distance in the figure at the outer mid-plane (if they are connected). For the flux surface disconnected by the second separatrix, movement of flux surfaces with the same Ψ_{pol} values are shown.

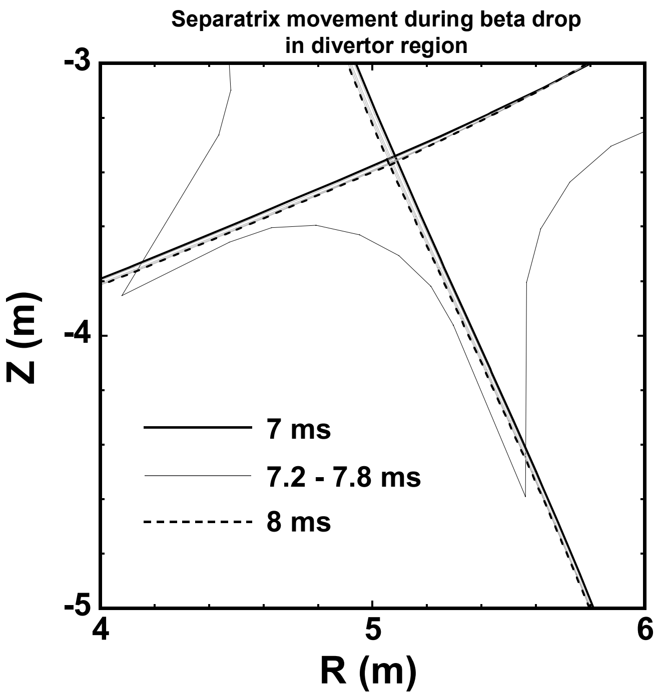

Figure 3.11
Movement of the strike point and separatrix surface during the beta drop

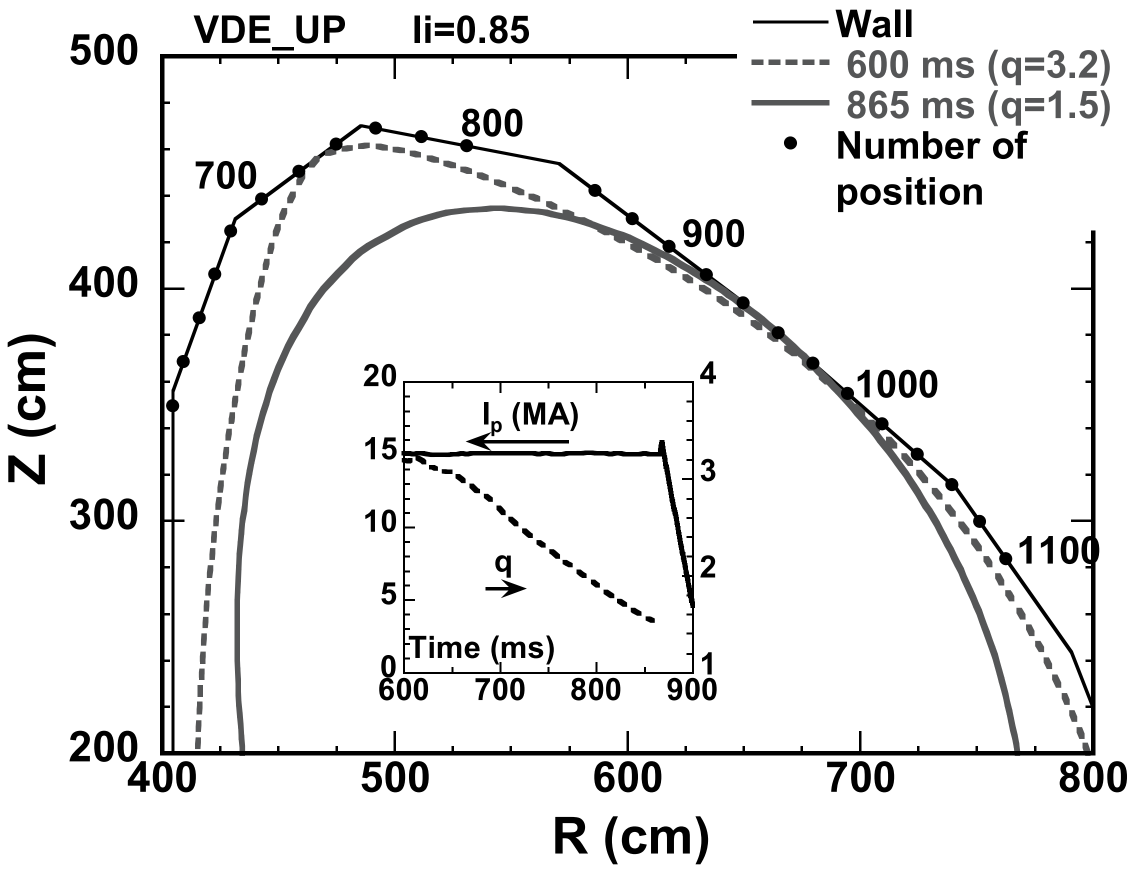

Figure 3.12
Equilibrium configurations at *600 ms* (early phase of plasma touching the upper wall) and at *865 ms* (just before the TQ at *q=1.5*) for the upward VDE (Fig. 1.4). Insert shows time evolution of plasma current and safety factor.

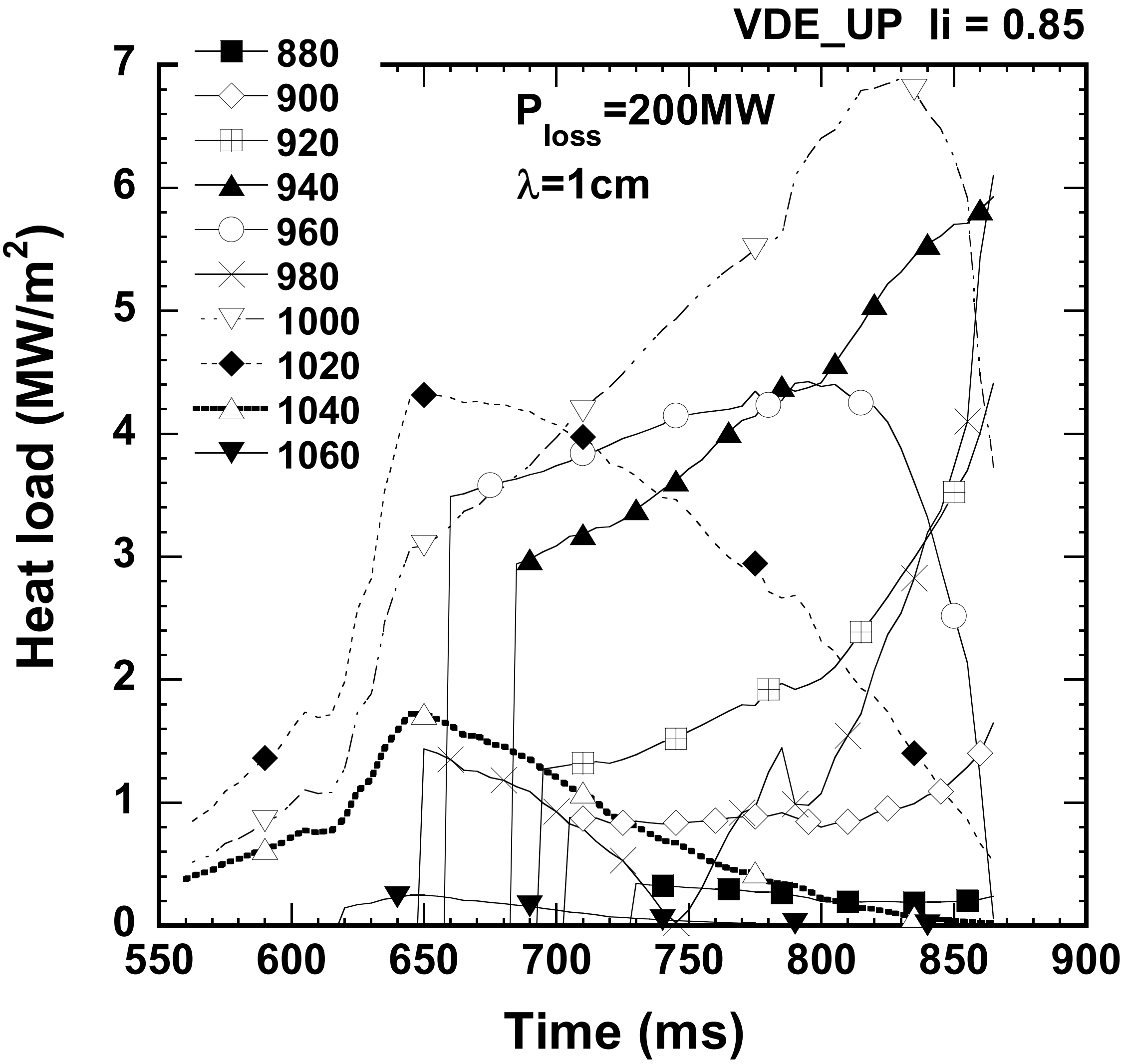

Figure 3.13
Time evolutions of the heat load (*MW/m²*) on the wall position (*880-1060*) during the vertical movement (*550-865 ms*) for the upward VDE (Fig. 1.4). Heat flow across the LCFS is *200 MW* and *λss ≈1 cm*.

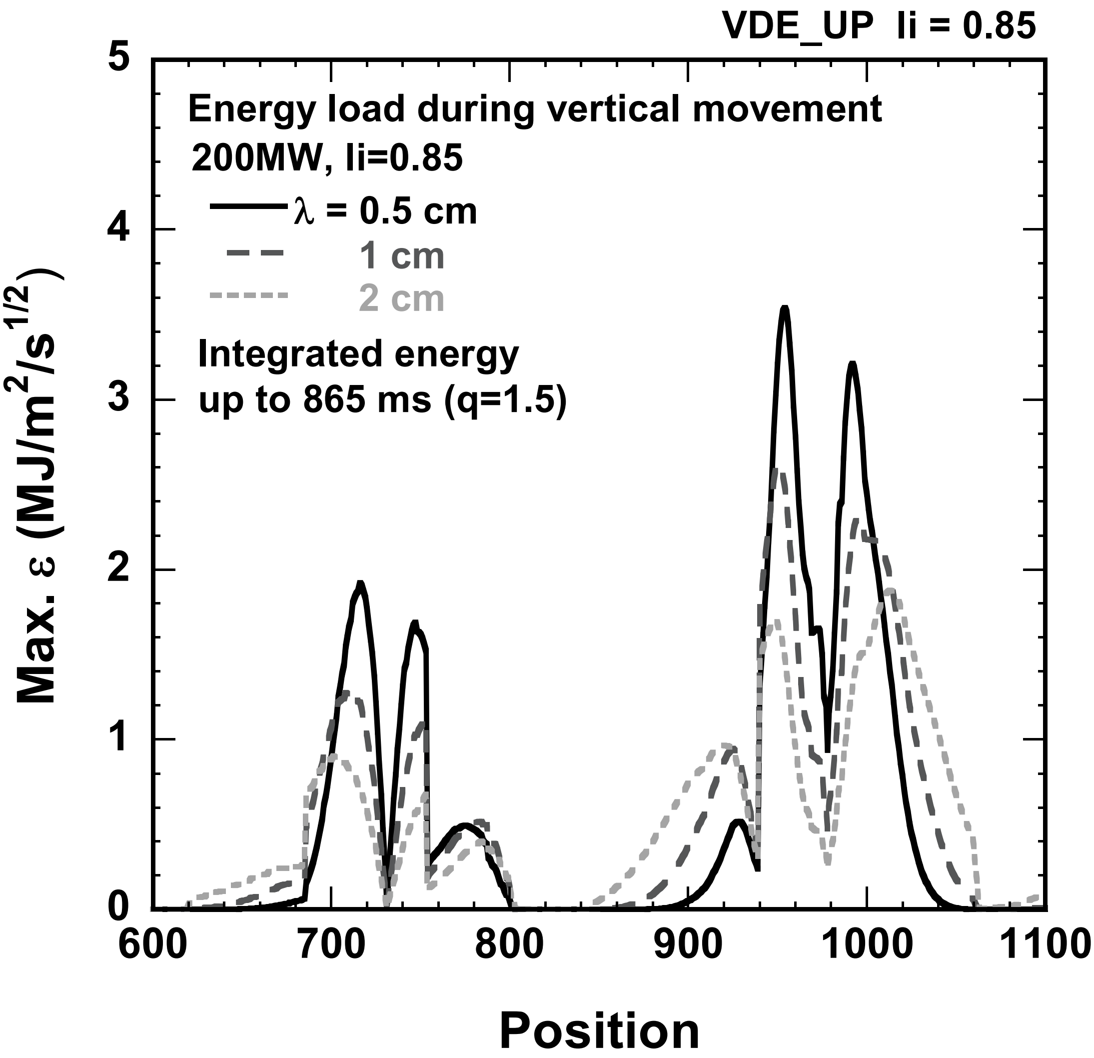

Figure 3.14
Maximum value of ε at each wall position during the vertical movement (*550-865 ms*) for three different λ*ss* (solid line for *0.5 cm*, dashed line for *1 cm* and dotted line for *2 cm*) for the upward VDE (Fig. 1.4)

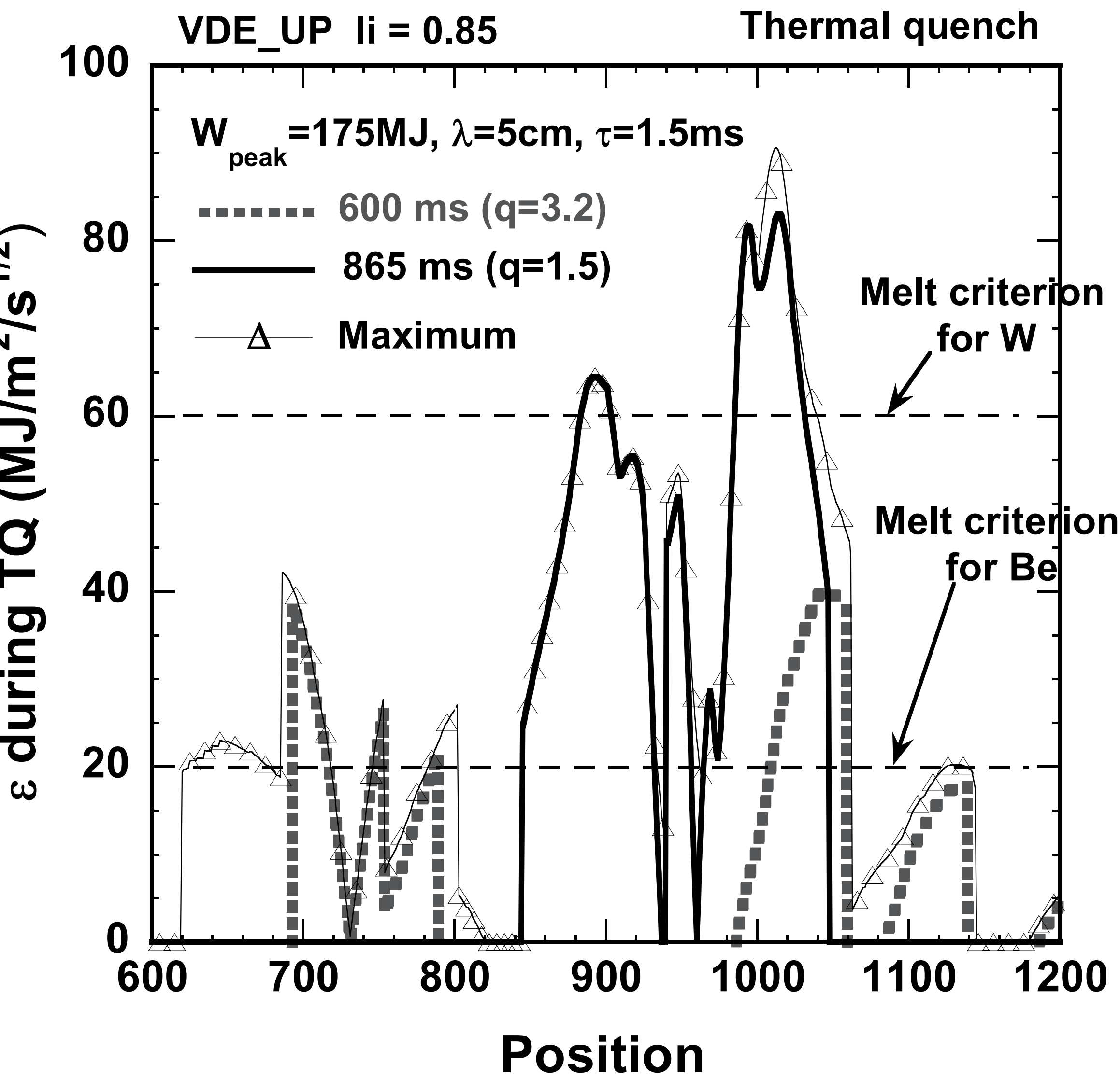

Figure 3.15

ε during the TQ at each wall position at two occurrence times of the TQ, i.e., *600 ms* (dotted line) and *865 ms* (solid line) for the upward VDE (Fig. 1.4). It is assumed that *175MJ* is released during the TQ with an energy deposition width of *5 cm* and a time duration of the energy deposition of *1.5 ms*. Triangles show the maximum values when the TQ occurs at an arbitrary time moment between *550 ms* and *865 ms*. Lower dotted horizontal line shows the critical value for melting of *Be*. The critical value for tungsten is also shown for comparison (upper dotted line; $\approx 60\ MJ/m^2/s^{1/2}$).

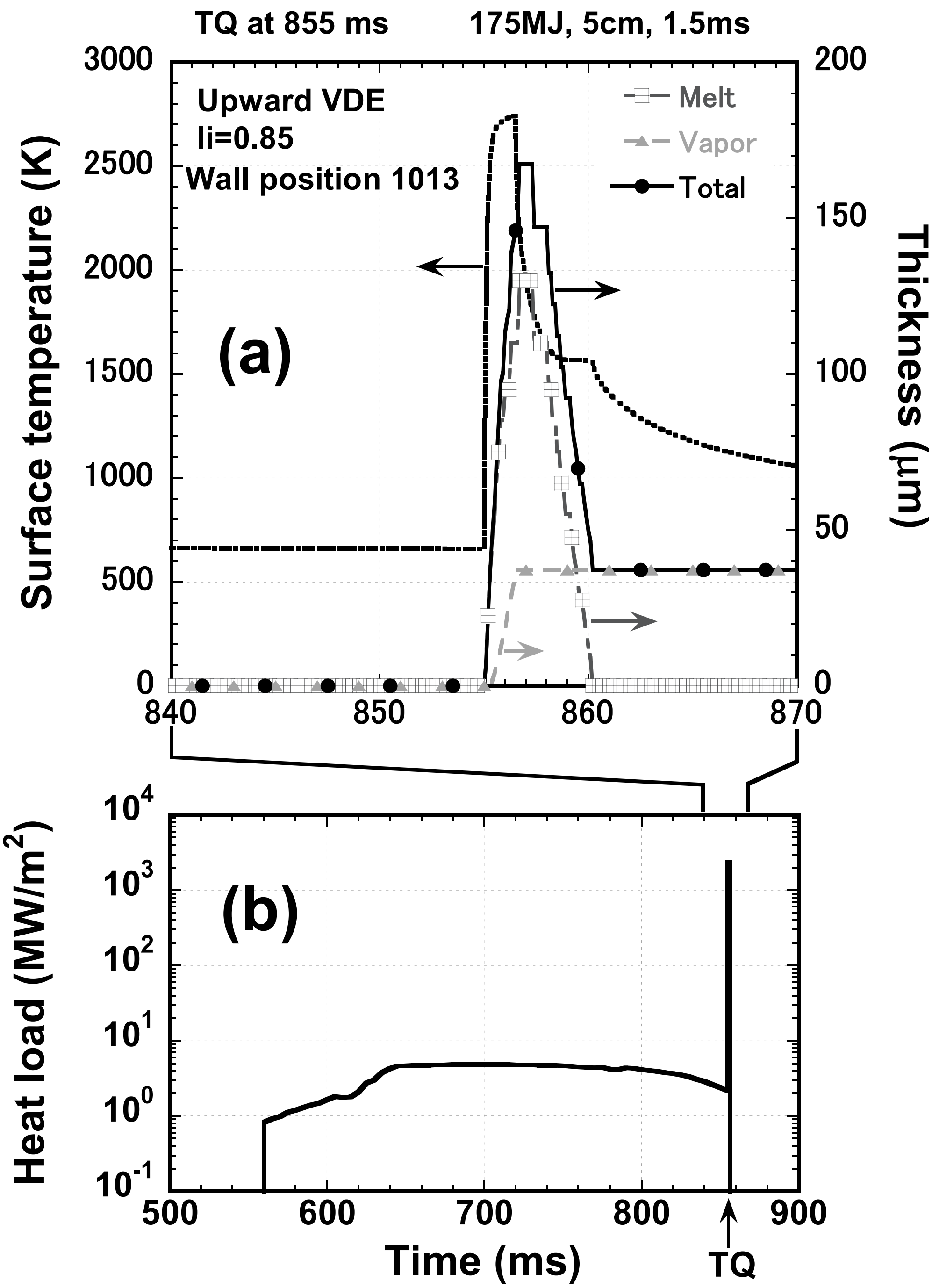

Figure 3.16 (a)
Time evolutions of the surface temperature and melting/vaporized thickness at wall position *1013* for the case of TQ occurrence time of *855 ms* for the upward VDE (Fig. 1.4). It is assumed that *175MJ* is released during the TQ with an energy deposition width of *5 cm* and a time duration of the energy deposition of *1.5 ms*.

Figure 3.16 (b)
Time evolutions of the heat load for the case of Fig. 3.16 (a).

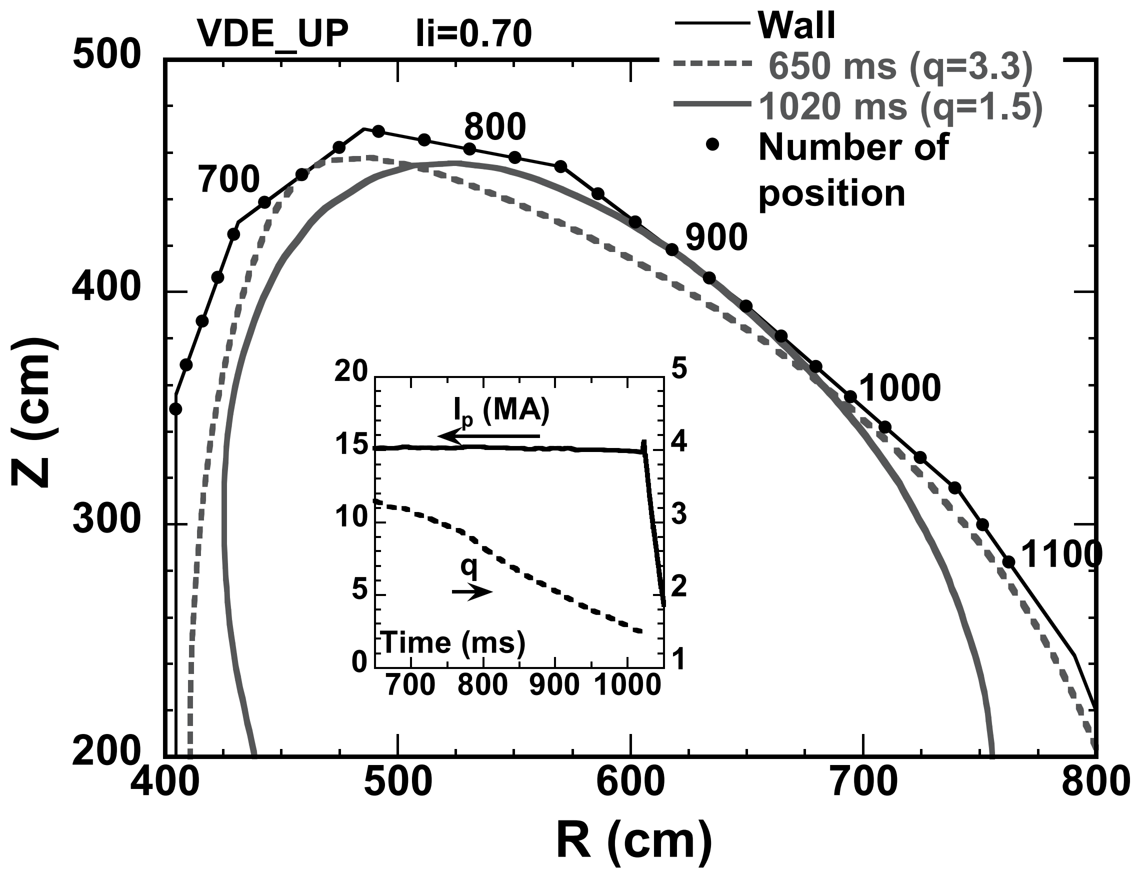

Figure 3.17
Equilibrium configurations at *650 ms* (early phase of plasma touching the upper wall) and at *1020 ms* (just before the TQ at *q=1.5*) for the upward VDE with l_i = *0.7*. Insert shows time evolution of plasma current and safety factor.

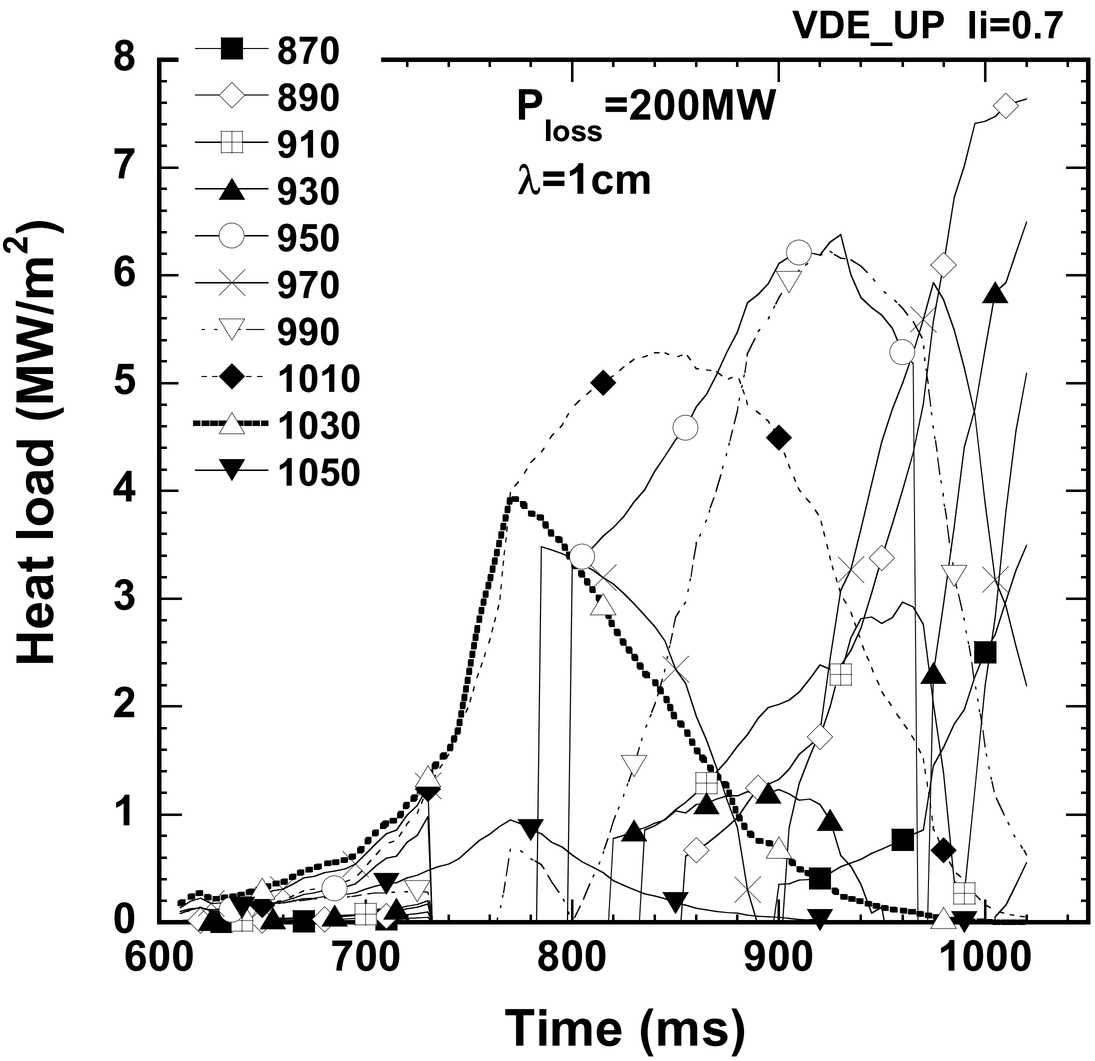

Figure 3.18
Time evolutions of the heat load (*MW/m^2*) on the wall position (*870-1050*) during the vertical movement (*620-1020 ms*) for the upward VDE with l_i = *0.7*. Heat flow across the LCFS is *200 MW* and *$\lambda ss \approx 1$ cm*.

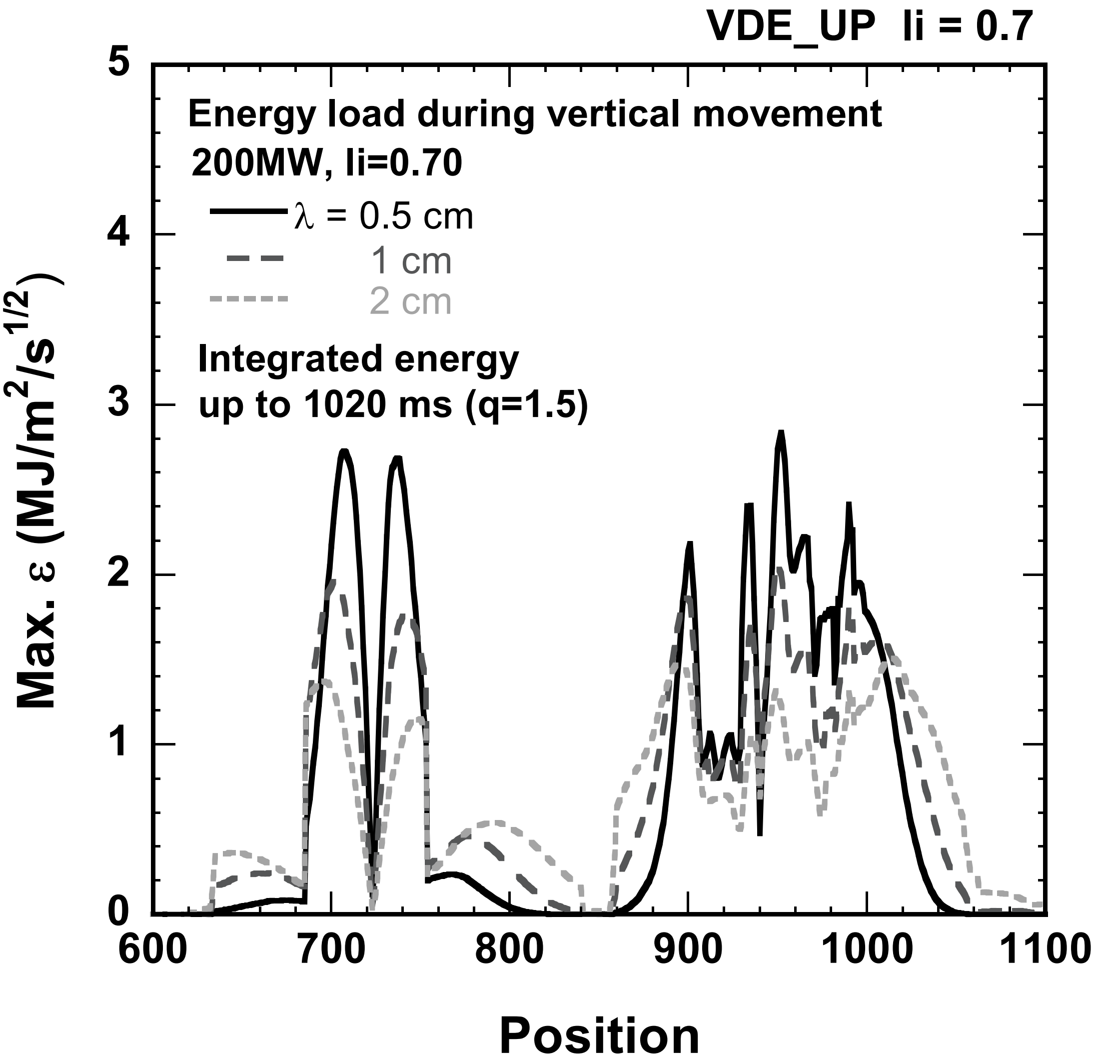

Figure 3.19
Maximum value of ε at each wall position during the vertical movement (*620-1020 ms*) for three different λss (solid line for *0.5 cm*, dashed line for *1 cm* and dotted line for *2 cm*) for the upward VDE with $l_i = 0.7$

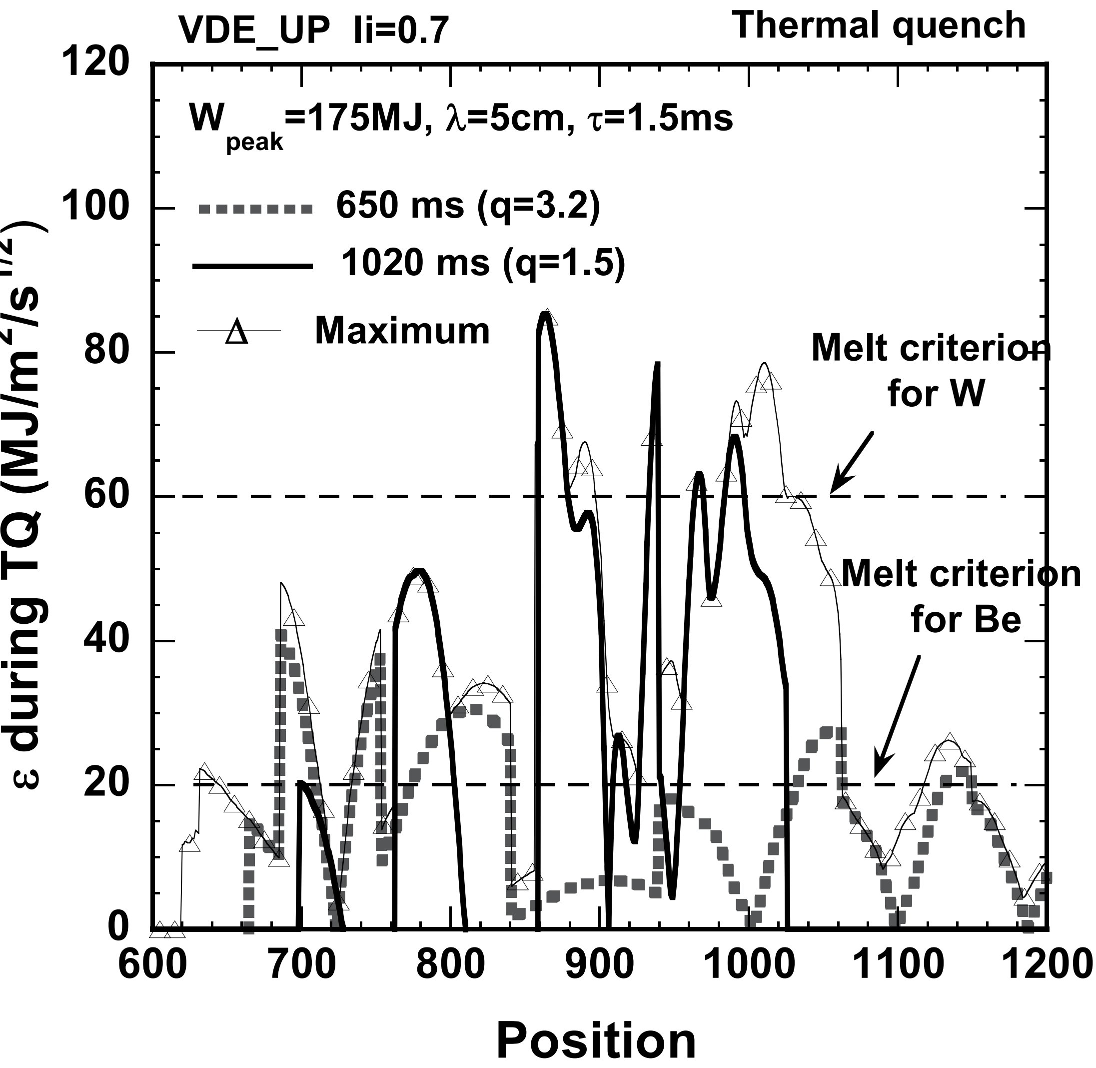

Figure 3.20

ε during the TQ at each wall position at two occurrence times of the TQ, i.e., *650 ms* (dotted line) and *1020 ms* (solid line) for the upward VDE with $l_i = 0.7$. It is assumed that *175MJ* is released during the TQ with an energy deposition width of *5 cm* and a time duration of the energy deposition of *1.5 ms*. Triangles show the maximum values when the TQ occurs at an arbitrary time moment between *620 ms* and *1020 ms*. Lower dotted horizontal line shows the critical value for melting of *Be*. The critical value for tungsten is also shown for comparison (upper dotted line; $\approx 60\ MJ/m^2/s^{1/2}$).

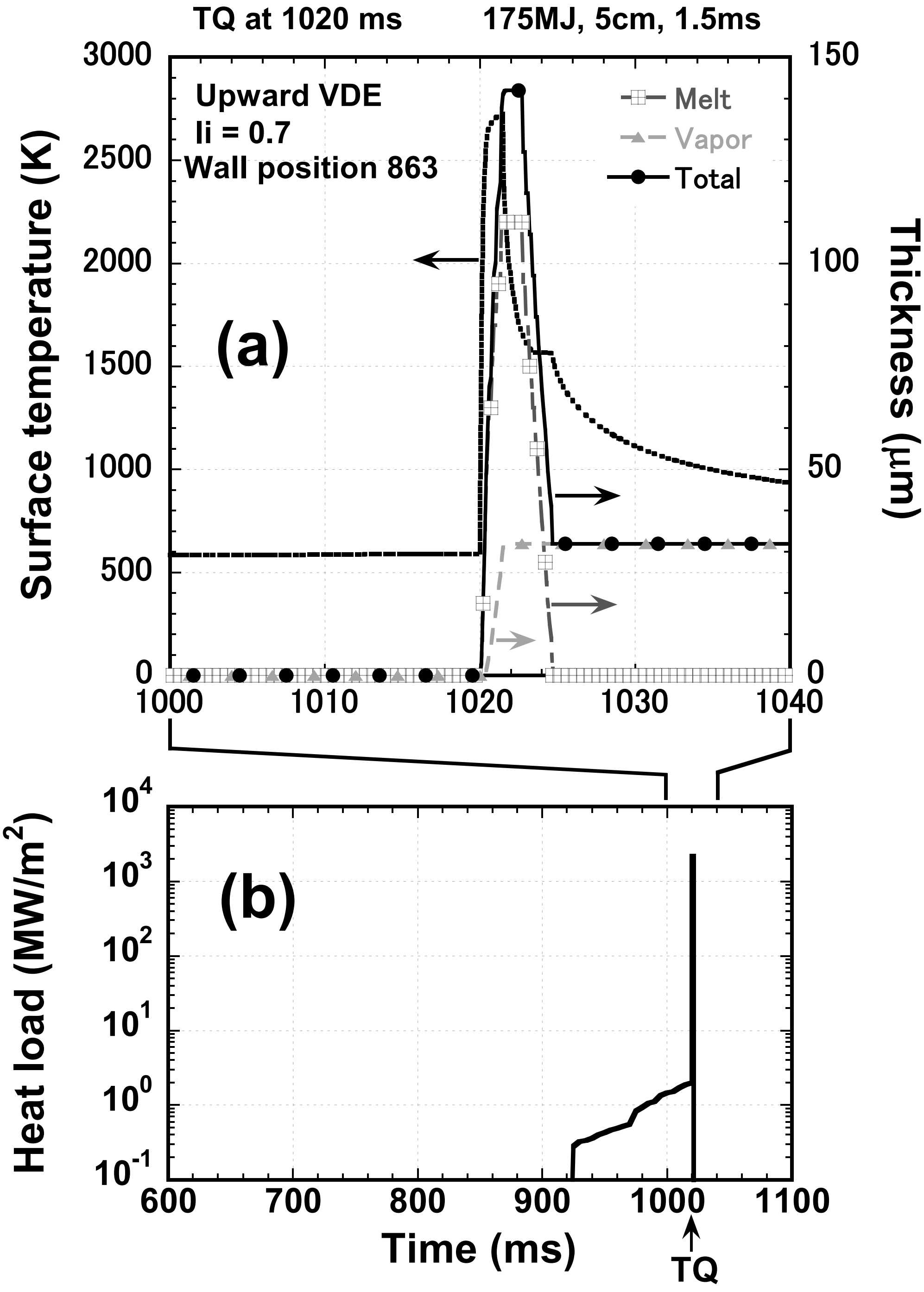

Figure 3.21 (a)
Time evolutions of the surface temperature and melting/vaporized thickness at wall position *863* for the case of TQ occurrence time of *1020 ms* for the upward VDE with l_i = *0.7*. It is assumed that *175MJ* is released during the TQ with an energy deposition width of *5 cm* and a time duration of the energy deposition of *1.5 ms*.

Figure 3.21 (b)
Time evolutions of the heat load for the case of Fig. 3.21 (a)

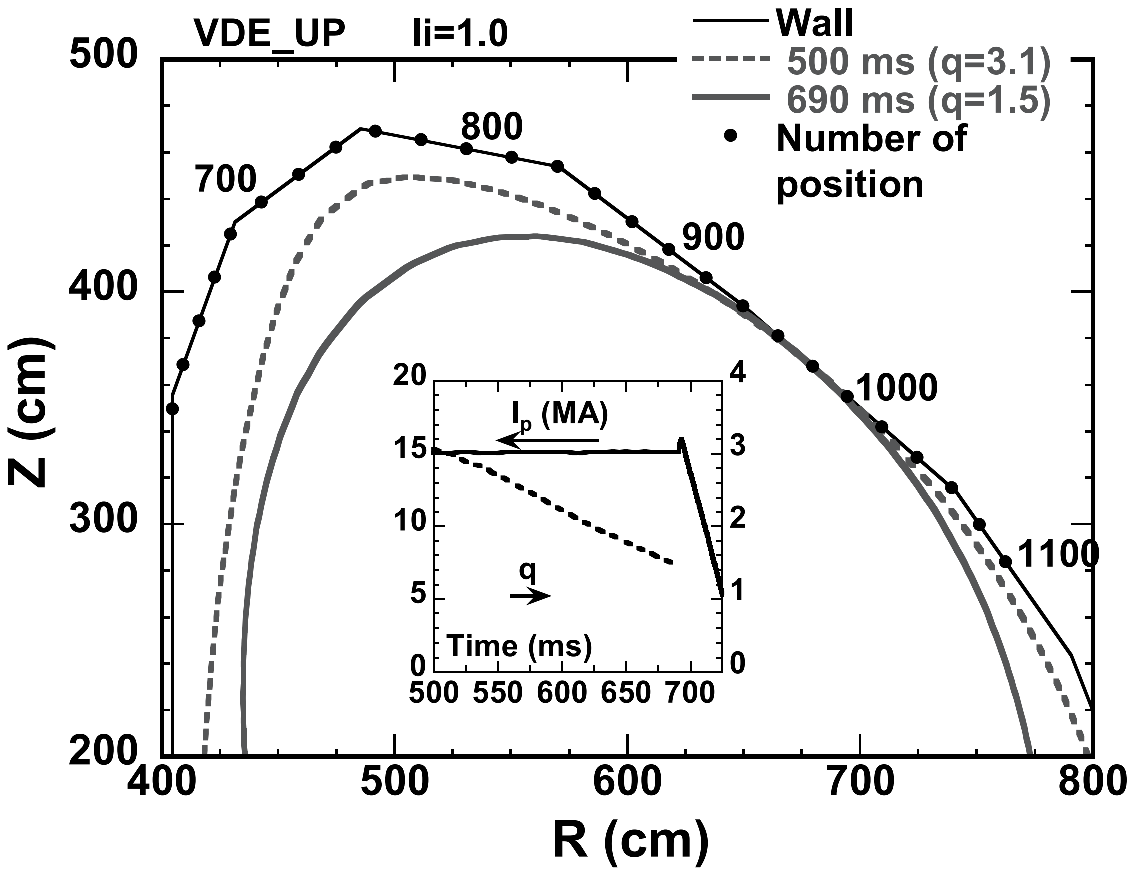

Figure 3.22
Equilibrium configurations at *500 ms* (early phase of plasma touching the upper wall) and at *690 ms* (just before the TQ at *q=1.5*) for the upward VDE with l_i = *1.0*. Insert shows time evolution of plasma current and safety factor.

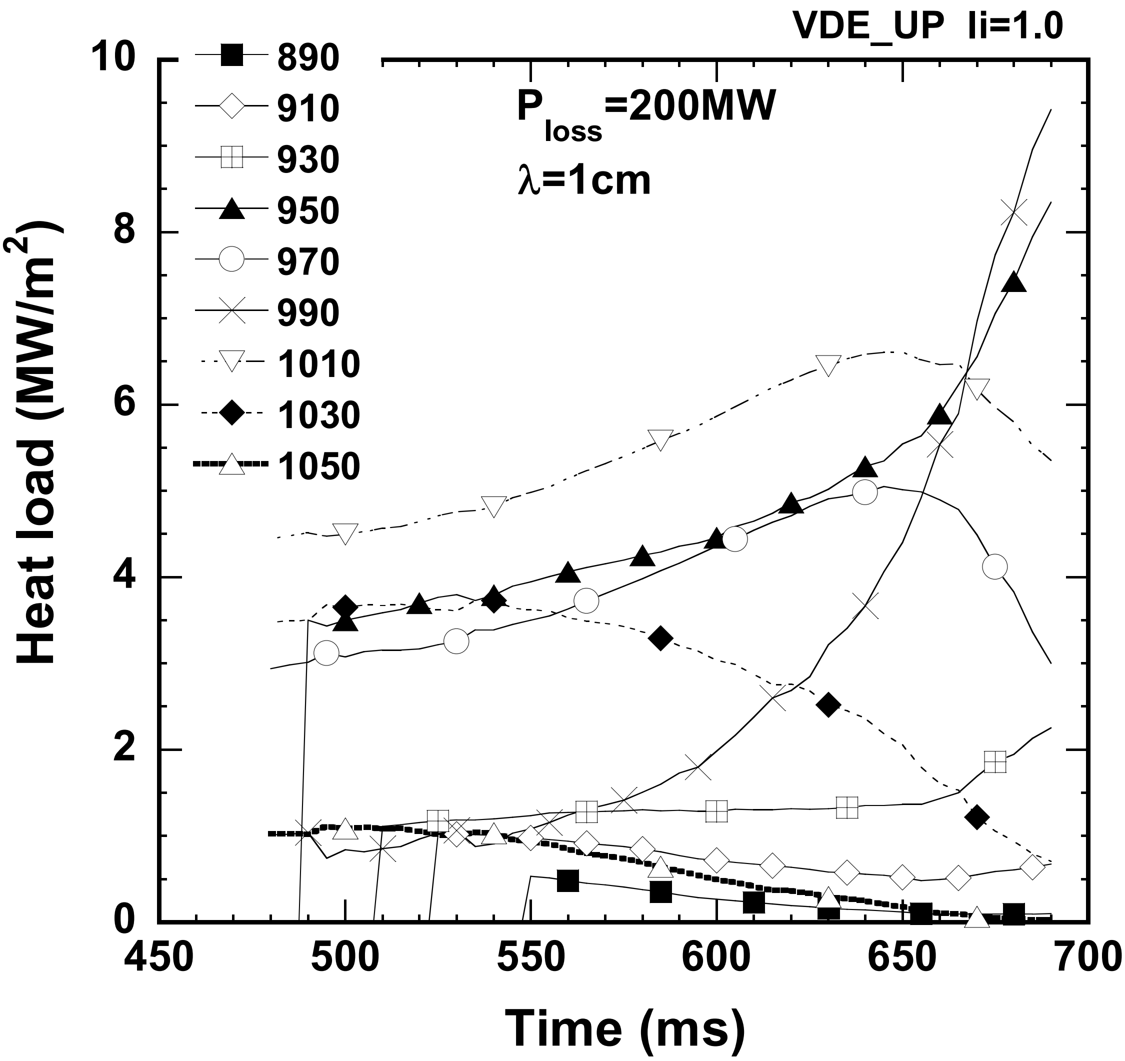

Figure 3.23
Time evolutions of the heat load (*MW/m^2*) on the wall position (*890-1050*) during the vertical movement (*480-690 ms*) for the upward VDE with *l_i = 1.0*. Heat flow across the LCFS is *200 MW* and *$\lambda ss \approx 1$ cm*.

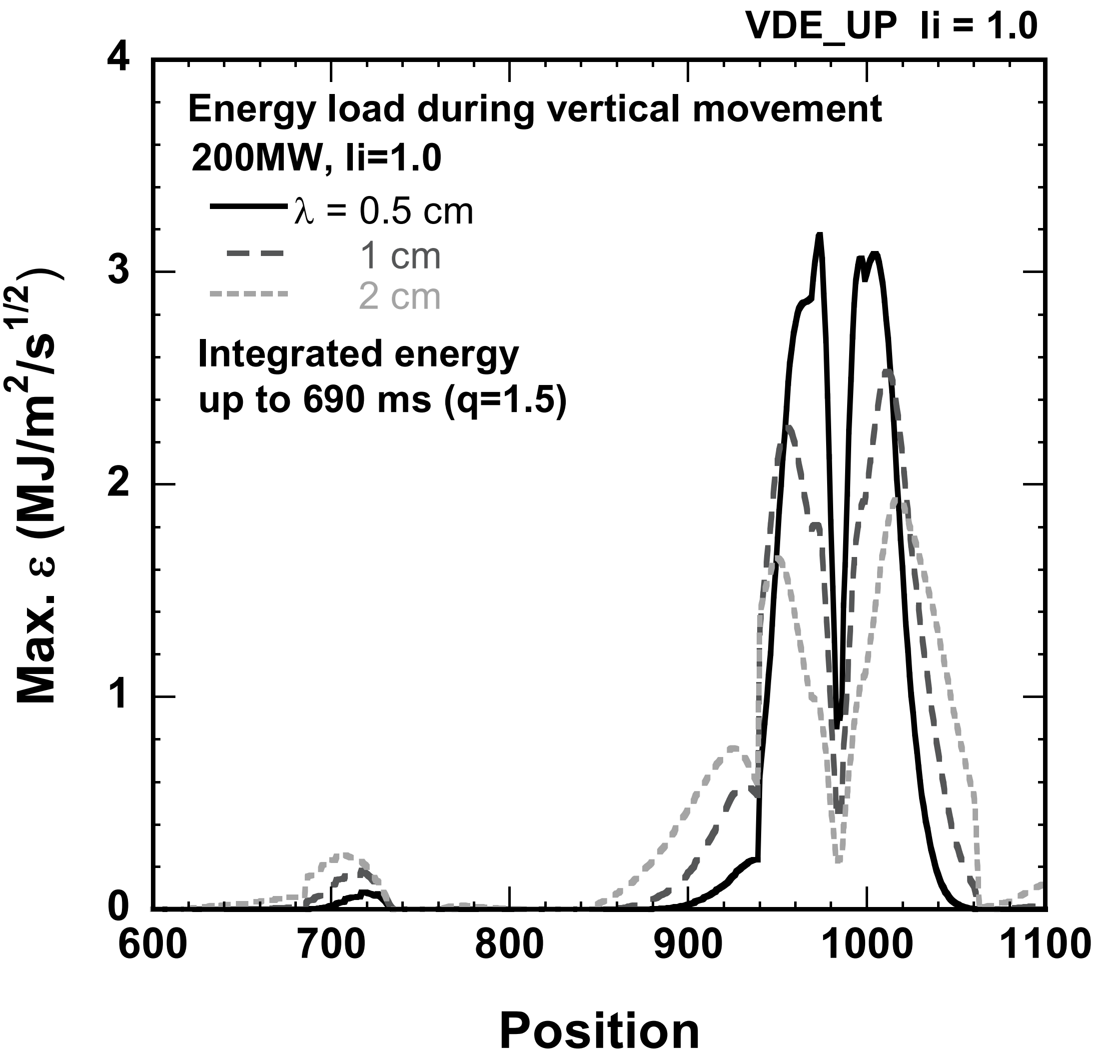

Figure 3.24
Maximum value of ε at each wall position during the vertical movement (*480-690 ms*) for three different λss (solid line for *0.5 cm*, dashed line for *1 cm* and dotted line for *2 cm*) for the upward VDE with $l_i = 1.0$

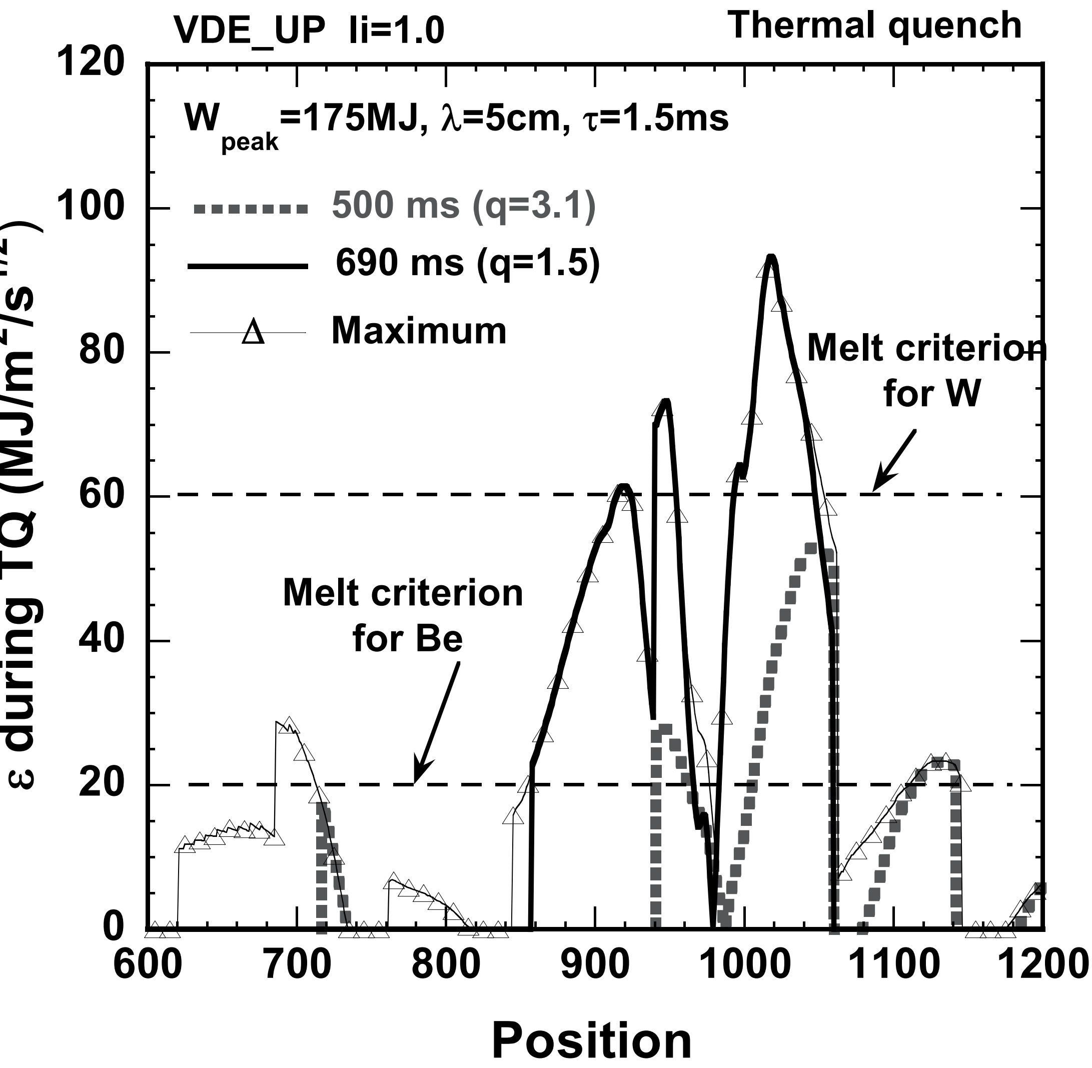

Figure 3.25
ε during the TQ at each wall position at two occurrence times of the TQ, i.e., *500 ms* (dotted line) and *690 ms* (solid line) for the upward VDE with $l_i = 1.0$. It is assumed that *175MJ* is released during the TQ with an energy deposition width of *5 cm* and a time duration of the energy deposition of *1.5 ms*. Triangles show the maximum values when the TQ occurs at an arbitrary time moment between *480 ms* and *690 ms*. Lower dotted horizontal line shows the critical value for melting of *Be*. The critical value for tungsten is also shown for comparison (upper dotted line; ≈ 60 $MJ/m^2/s^{1/2}$).

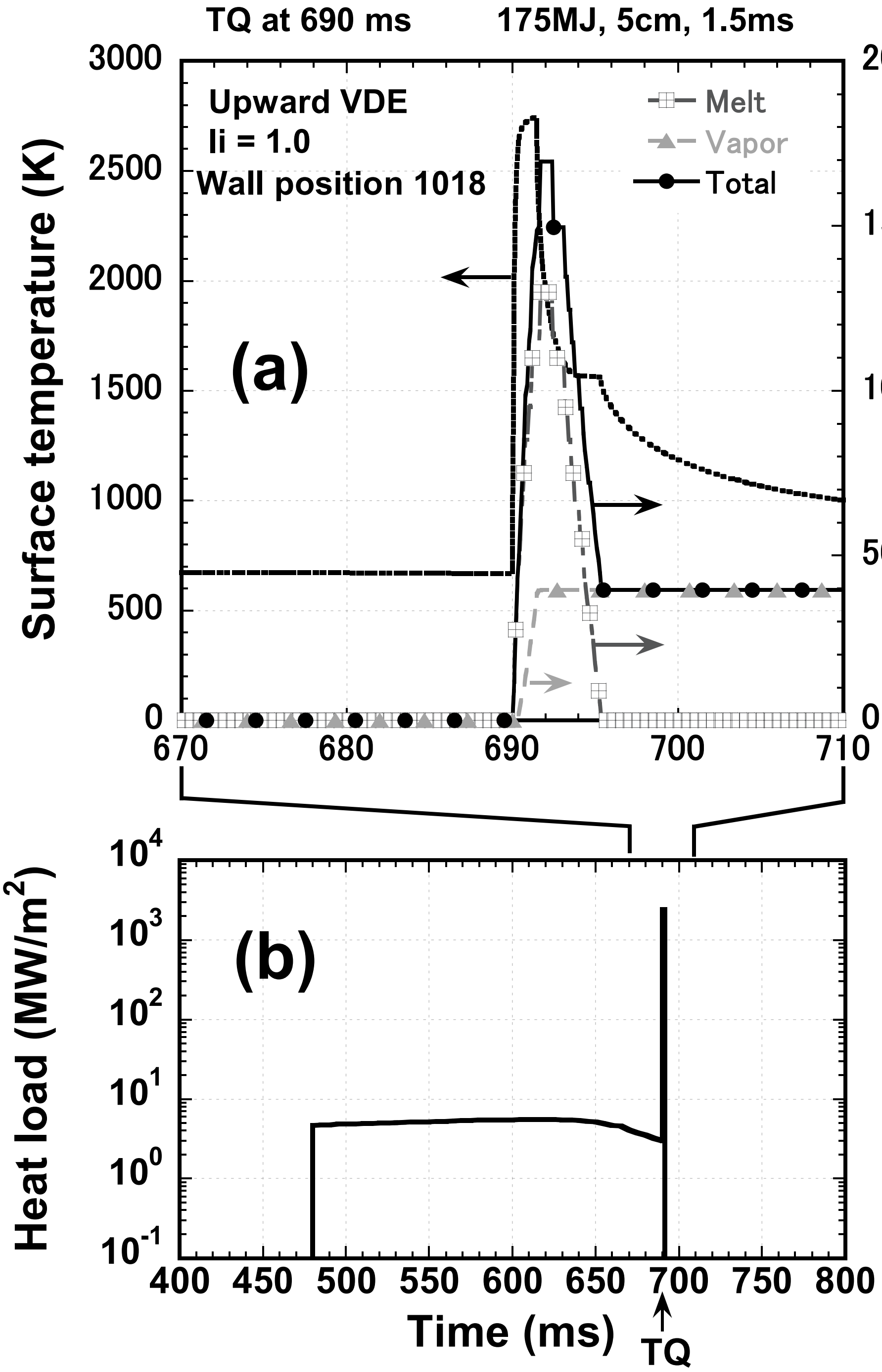

Figure 3.26 (a)
Time evolutions of the surface temperature and melting/vaporized thickness at wall position *1018* for the case of TQ occurrence time of *690 ms* for the upward VDE with l_i = *1.0*. It is assumed that *175MJ* is released during the TQ with an energy deposition width of *5 cm* and a time duration of the energy deposition of *1.5 ms*.

Figure 3.26 (b)
Time evolutions of the heat load for the case of Fig. 3.26 (a)

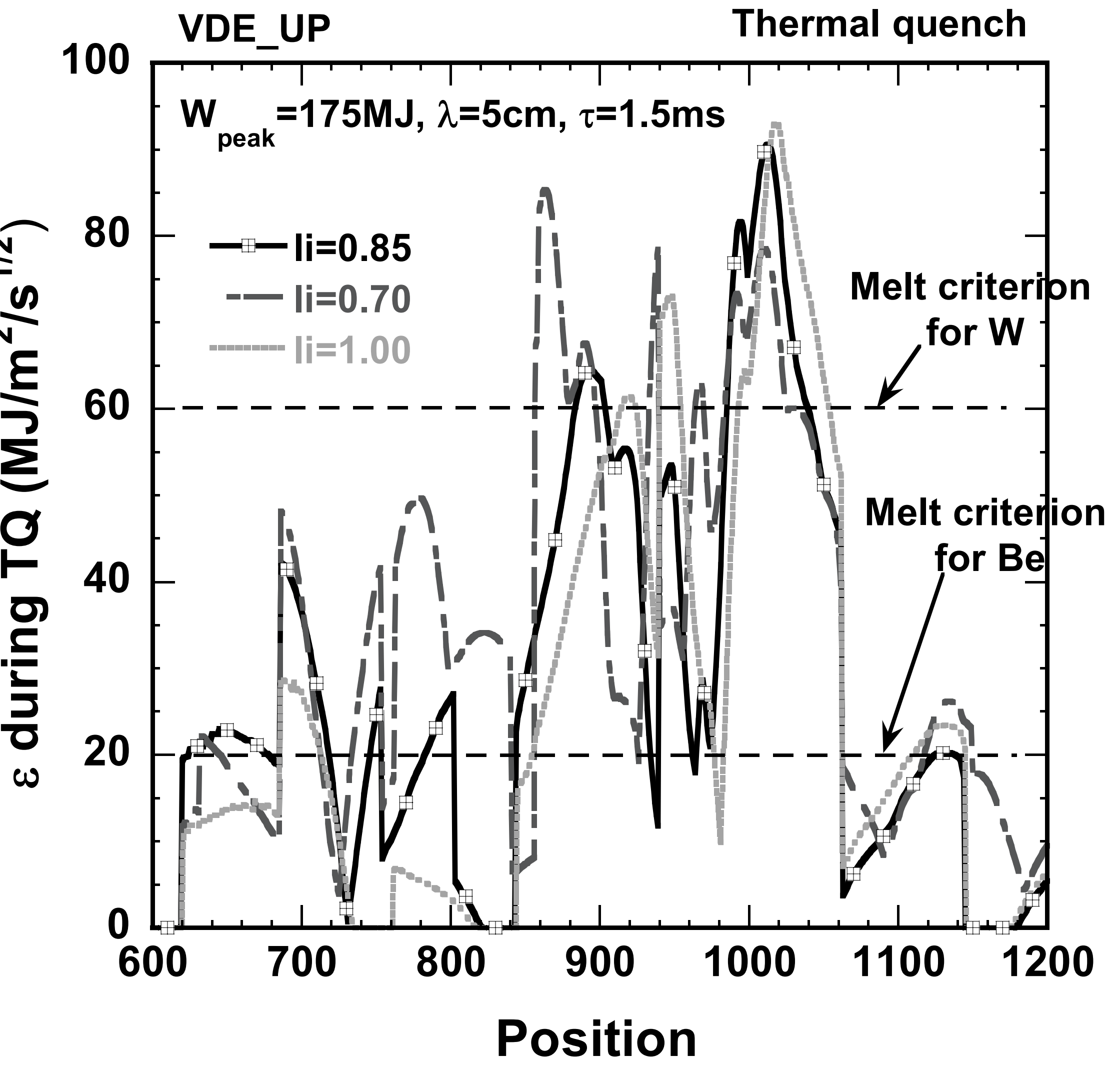

Figure 3.27
Comparison of ε during the TQ for two different internal inductances of the initial plasma, *0.7* (dashed line taken form open triangles in Fig. 3.20) and *1.0* (dotted line taken from open triangles in Fig. 3.25) with the reference case (solid line taken from open triangles in Fig. 3.15)

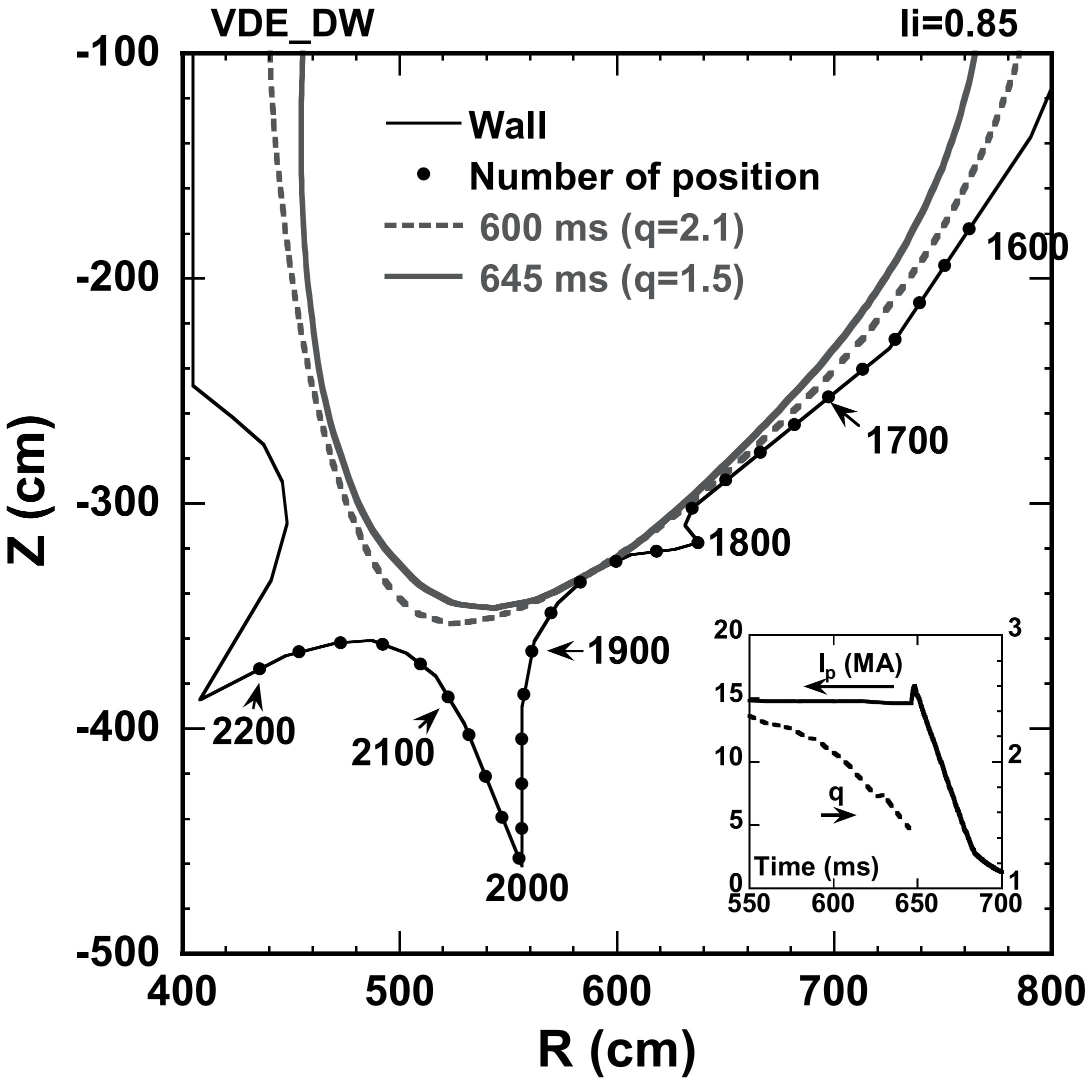

Figure 3.28
Equilibrium configurations at *600 ms* (*q=2.1*) and at *645 ms* (just before the TQ at *q=1.5*) for the downward VDE (Fig. 1.1). Insert shows time evolution of plasma current and safety factor.

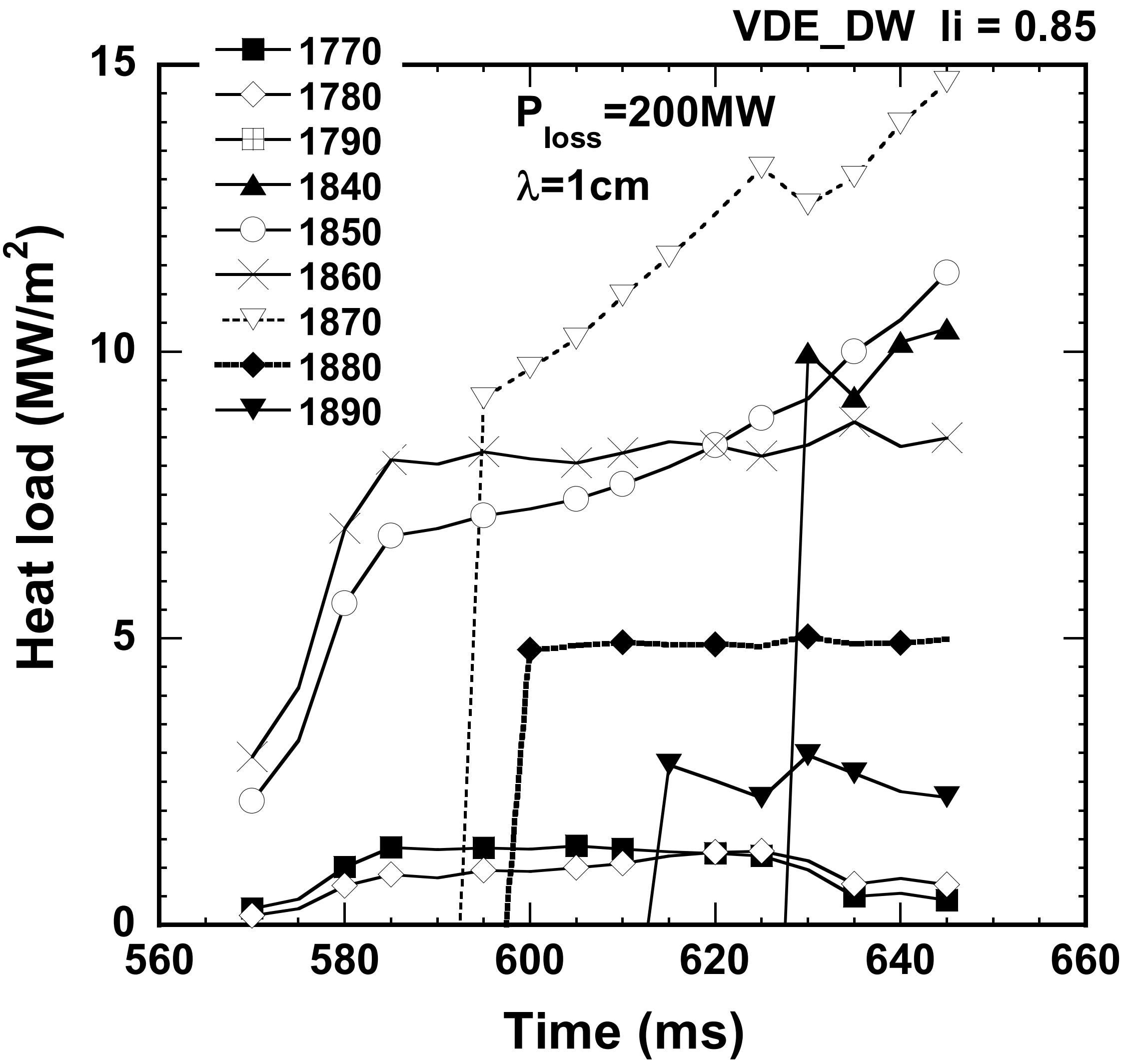

Figure 3.29
Time evolutions of the heat load (*MW/m^2*) on the wall position (*1770-1890*) during the vertical movement (*570-645 ms*) for the downward VDE (Fig. 1.1). Heat flow across the LCFS is *200 MW* and *$\lambda ss \approx 1$ cm*.

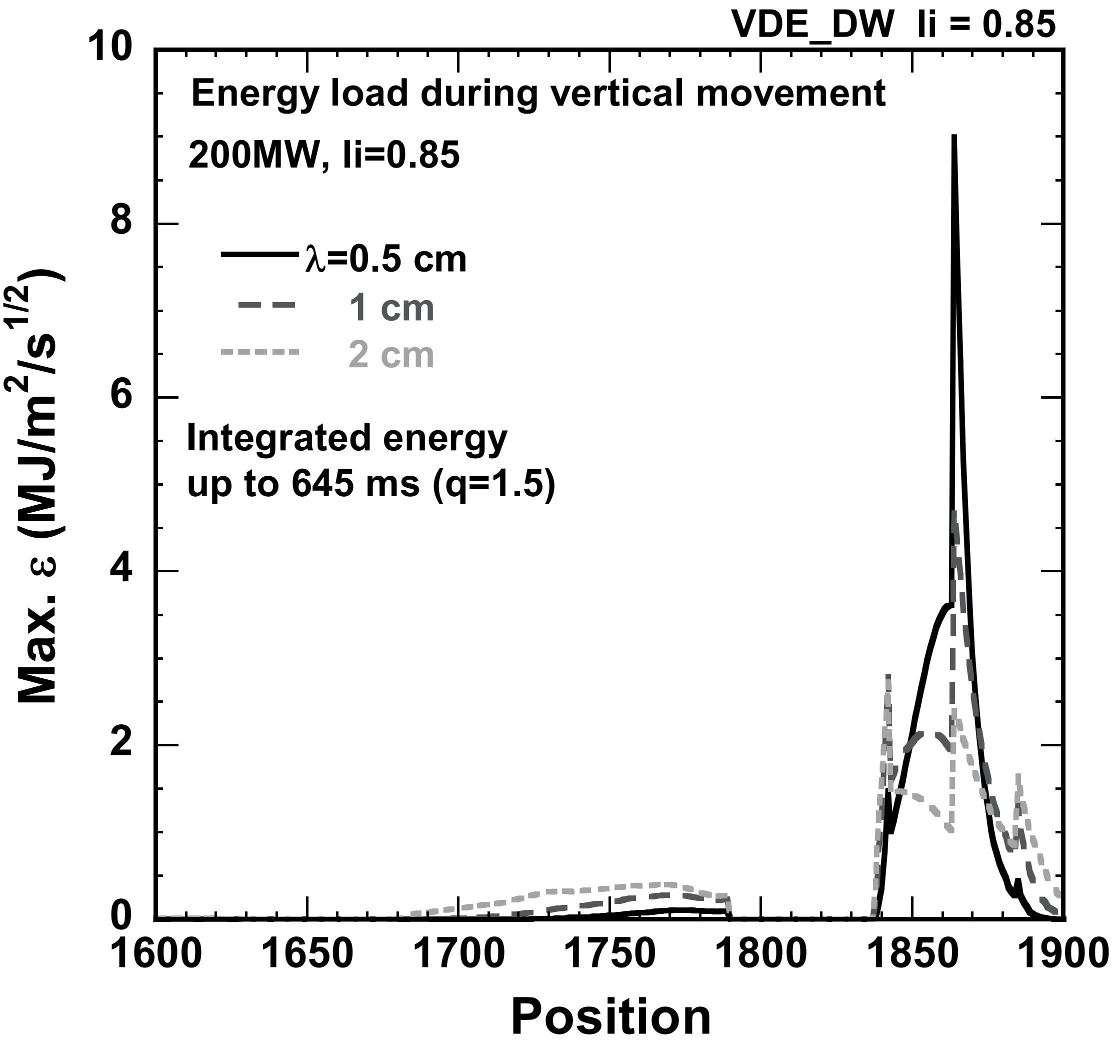

Figure 3.30
Maximum value of ε at each wall position during the vertical movement (*570-645 ms*) for three different *λss* (solid line for *0.5 cm,* dashed line for *1 cm* and dotted line for *2 cm*) for the downward VDE (Fig. 1.1)

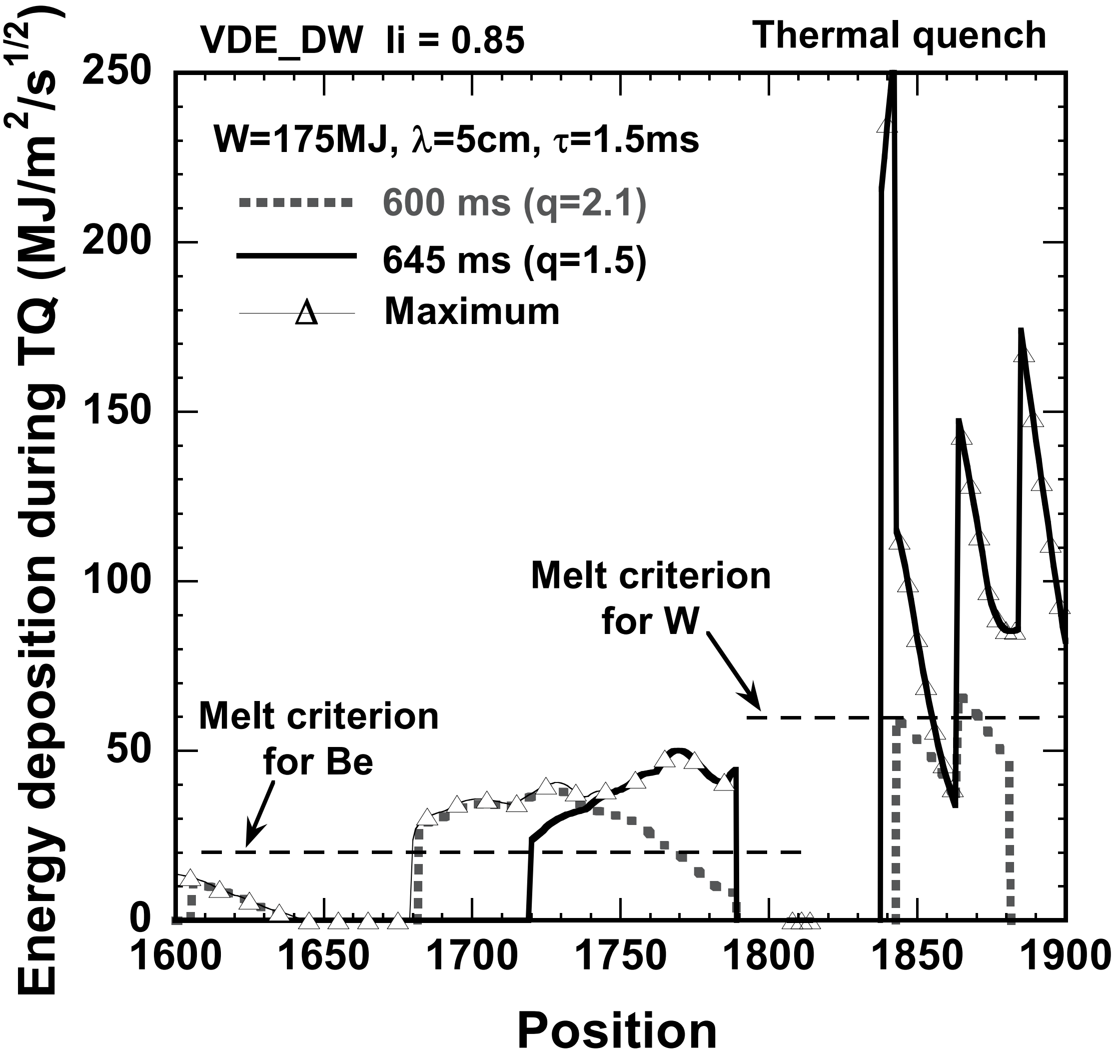

Figure 3.31

***ε* during the TQ at each wall position at two occurrence times of the TQ, i.e., *600 ms* (dotted line) and *645 ms* (solid line) for the downward VDE (Fig. 1.1). It is assumed that *175MJ* is released during the TQ with an energy deposition width of *5 cm* and a time duration of the energy deposition of *1.5 ms*. Triangles show the maximum values when the TQ occurs at an arbitrary time between *570 ms* and *645 ms*. Lower and upper dotted horizontal lines show the critical value for melting of *Be* and tungsten, respectively.**

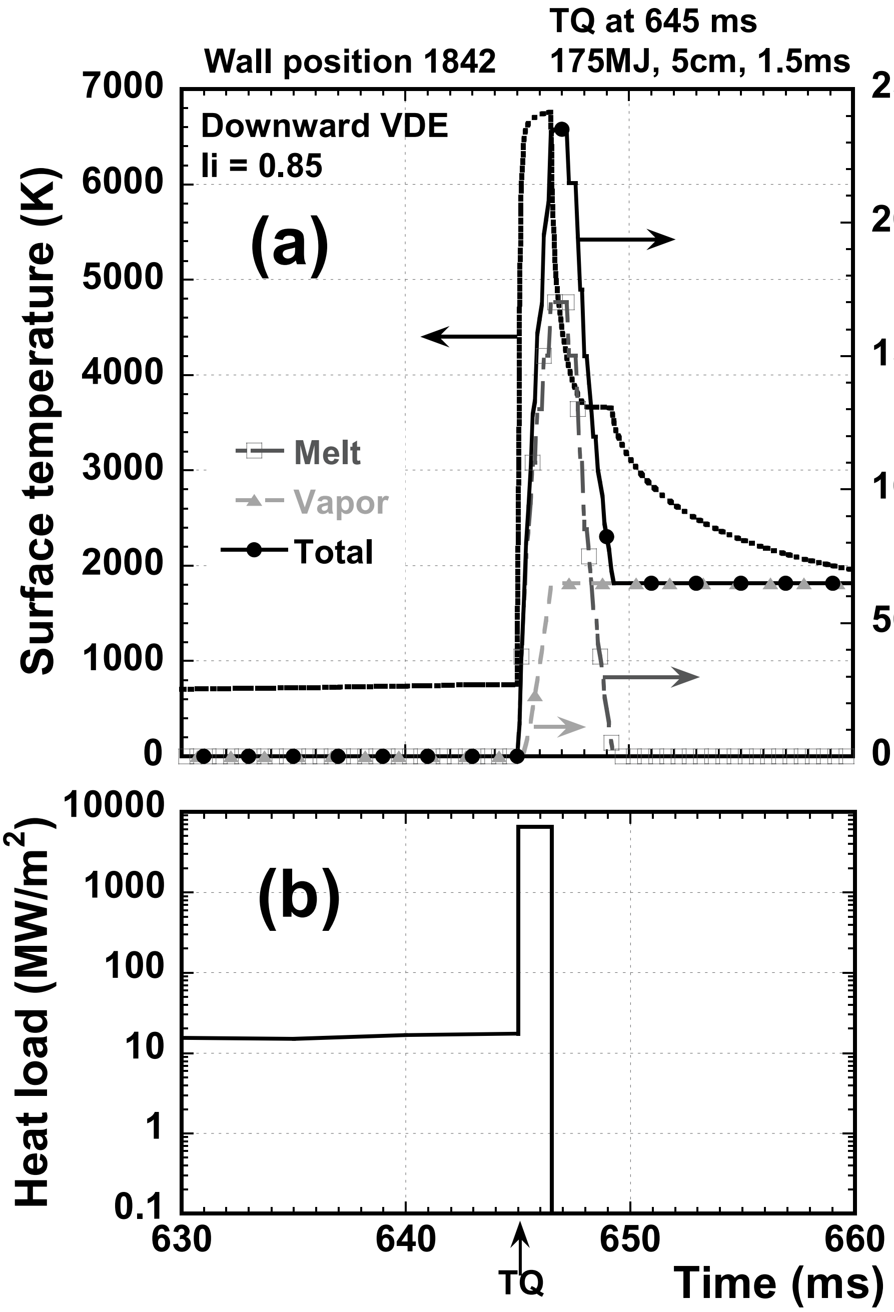

Figure 3.32 (a)
Time evolutions of the surface temperature and melting/vaporized thickness at wall position *1842* for the case of TQ occurrence time of *645 ms* for the downward VDE (Fig. 1.1). It is assumed that *175MJ* is released during the TQ with an energy deposition width of *5 cm* and a time duration of the energy deposition of *1.5 ms*.

Figure 3.32 (b)
Time evolutions of the heat load for the case of Fig. 3.32 (a).

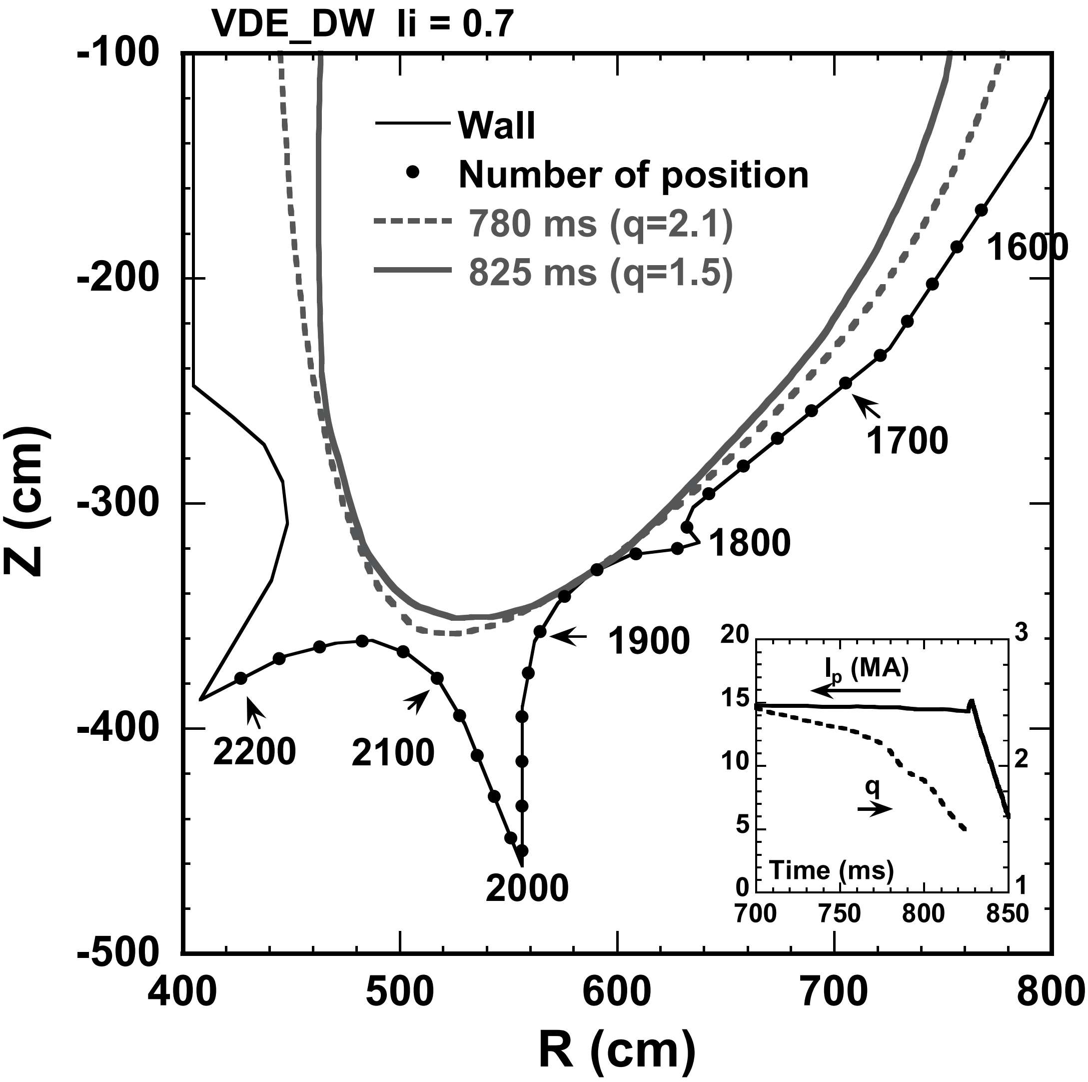

Figure 3.33
Equilibrium configurations at *780 ms* (*q=2.1*) and at *825 ms* (just before the TQ at *q=1.5*) for the downward VDE with $l_i = 0.7$. Insert shows time evolution of plasma current and safety factor.

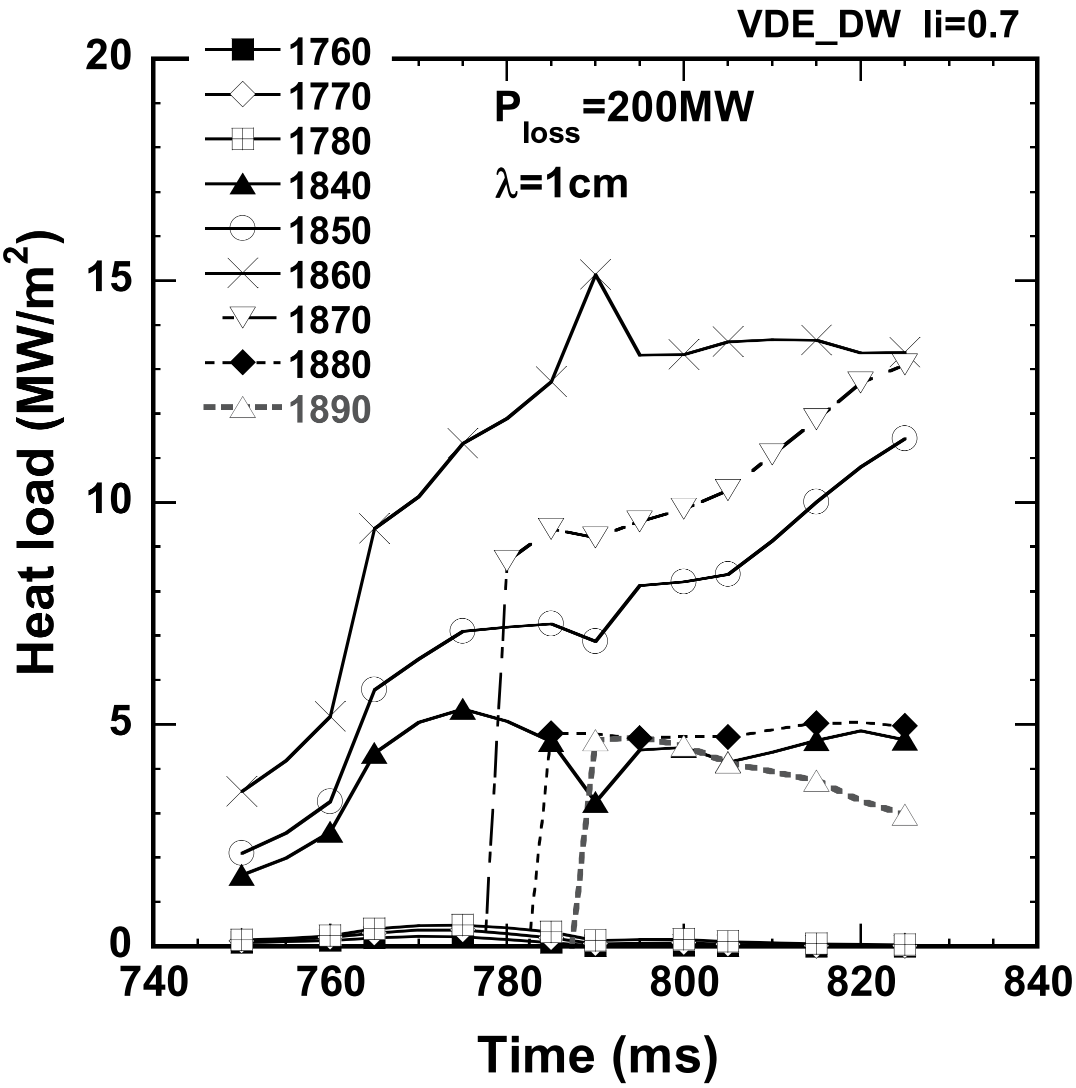

Figure 3.34
Time evolutions of the heat load (*MW/m^2*) on the wall position (*1760-1890*) during the vertical movement (*750-825 ms*) for the downward VDE with $l_i = 0.7$. Heat flow across the LCFS is *200 MW* and *$\lambda ss \approx 1$ cm*.

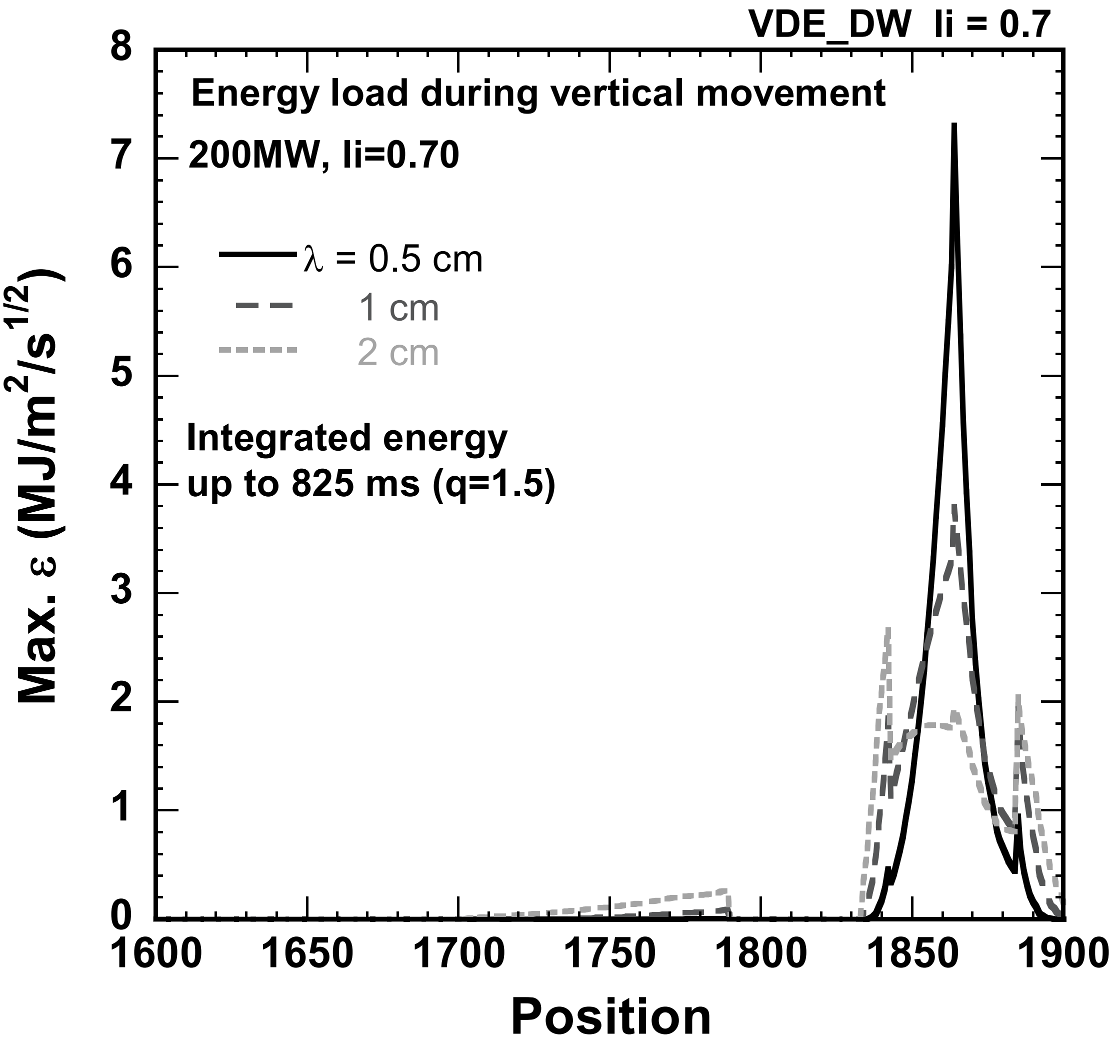

Figure 3.35

Maximum value of ε at each wall position during the vertical movement (*750-825 ms*) for three different *λss* (solid line for *0.5 cm,* dashed line for *1 cm* and dotted line for *2 cm*) for the downward VDE with l_i = *0.7*

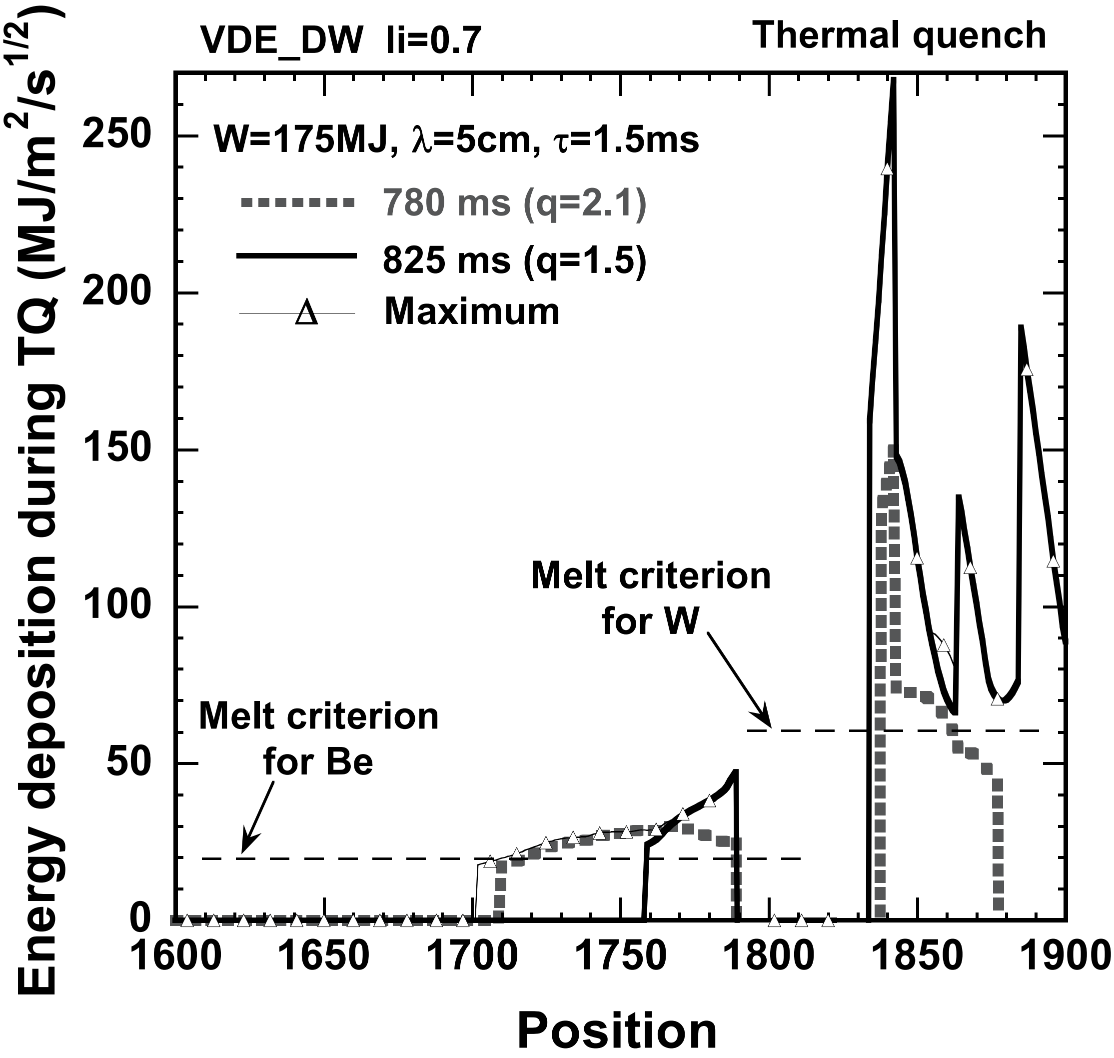

Figure 3.36

ε during the TQ at each wall position at two occurrence times of the TQ, i.e., *780 ms* (dotted line) and *825 ms* (solid line) for the downward VDE with $l_i = 0.7$. It is assumed that *175MJ* is released during the TQ with an energy deposition width of *5 cm* and a time duration of the energy deposition of *1.5 ms*. Triangles show the maximum values when the TQ occurs at an arbitrary time between *750 ms* and *825 ms*. Lower and upper dotted horizontal lines show the critical value for melting of *Be* and tungsten, respectively.

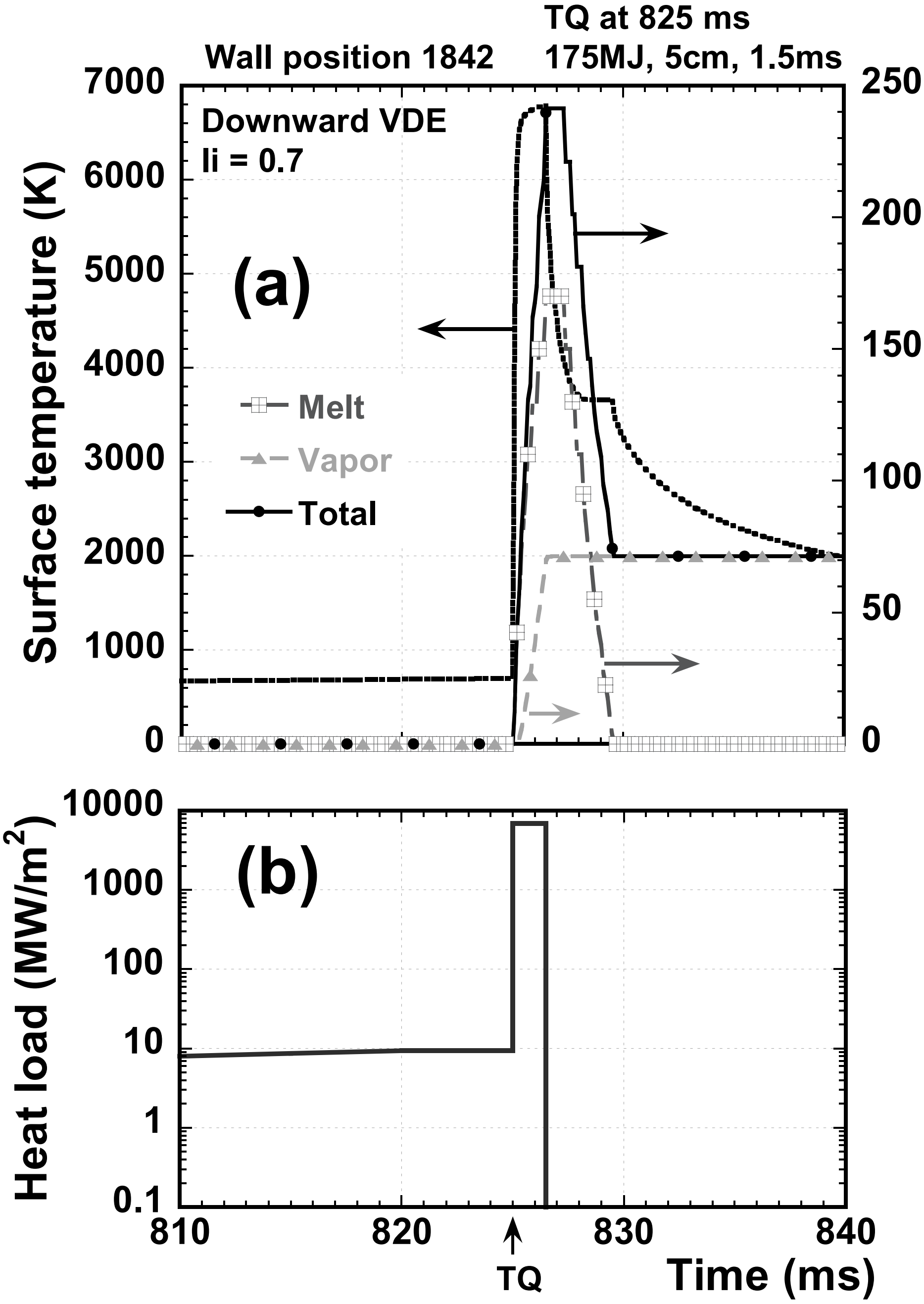

Figure 3.37 (a)
Time evolutions of the surface temperature and melting/vaporized thickness at wall position *1842* for the case of TQ occurrence time of *825 ms* for the downward VDE with $l_i = 0.7$. It is assumed that *175MJ* is released during the TQ with an energy deposition width of *5 cm* and a time duration of the energy deposition of *1.5 ms*.

Figure 3.37 (b)
Time evolutions of the heat load for the case of Fig. 3.37 (a)

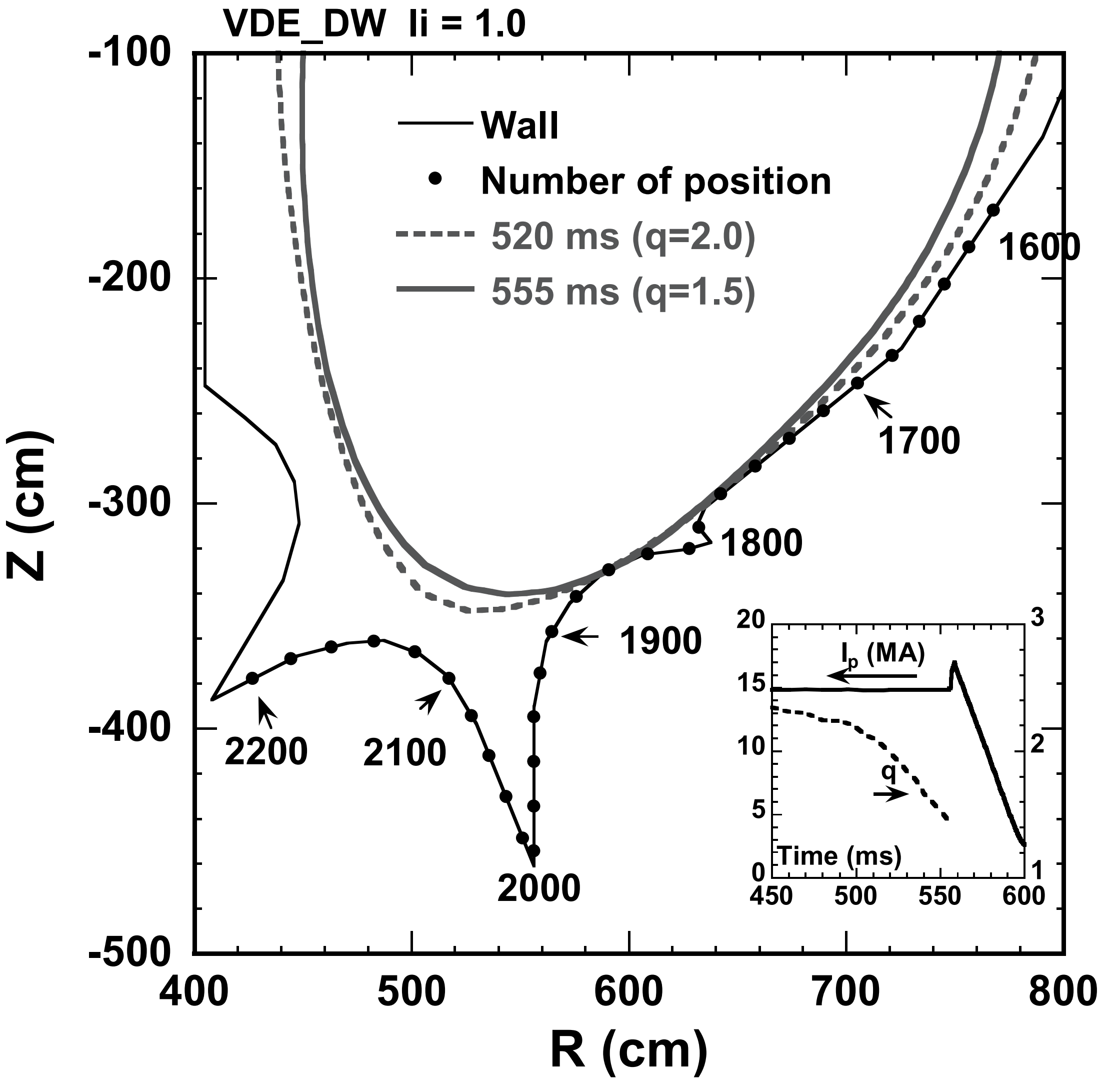

Figure 3.38
Equilibrium configurations at *520 ms* (*q=2.0*) and at *555 ms* (just before the TQ at *q=1.5*) for the downward VDE with l_i = *1.0*. Insert shows time evolution of plasma current and safety factor.

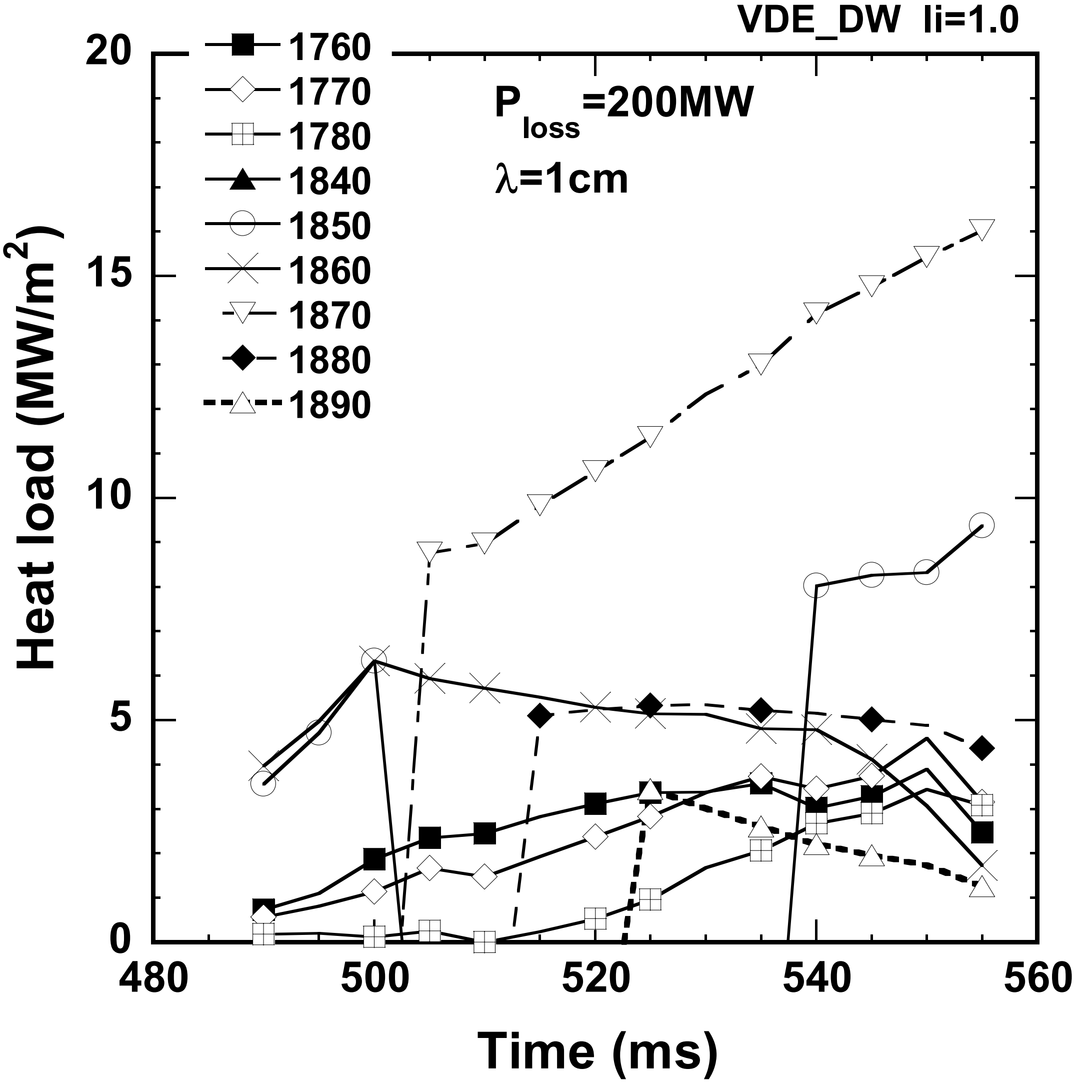

Figure 3.39
Time evolutions of the heat load (*MW/m^2*) on the wall position (*1760-1890*) during the vertical movement (*490-555 ms*) for the downward VDE with l_i = *1.0*. Heat flow across the LCFS is *200 MW* and *$\lambda ss \approx 1$ cm*.

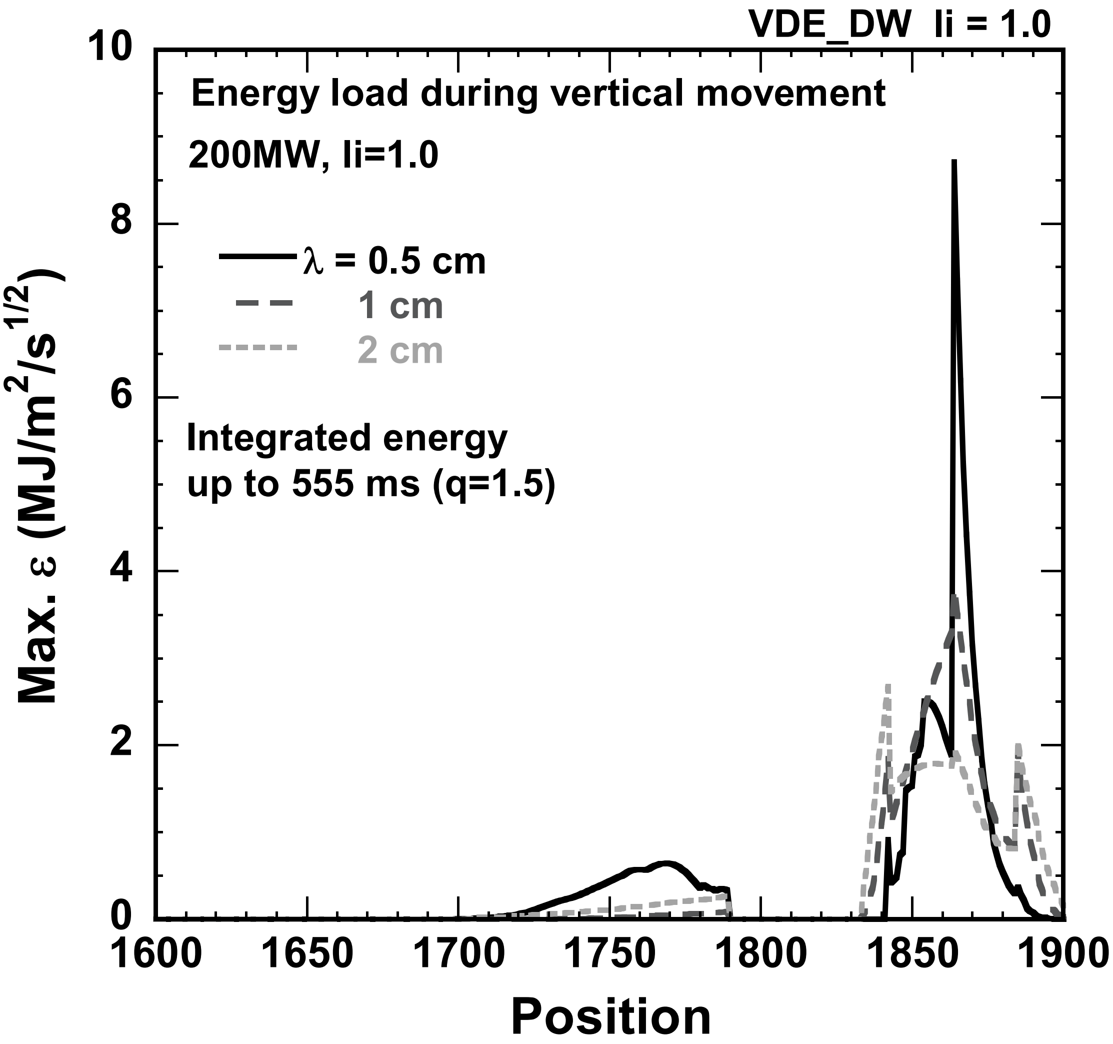

Figure 3.40
Maximum value of ε at each wall position during the vertical movement (*490-555 ms*) for three different λ*ss* (solid line for *0.5 cm,* dashed line for *1 cm* and dotted line for *2 cm*) for the downward VDE with l_i = *1.0*

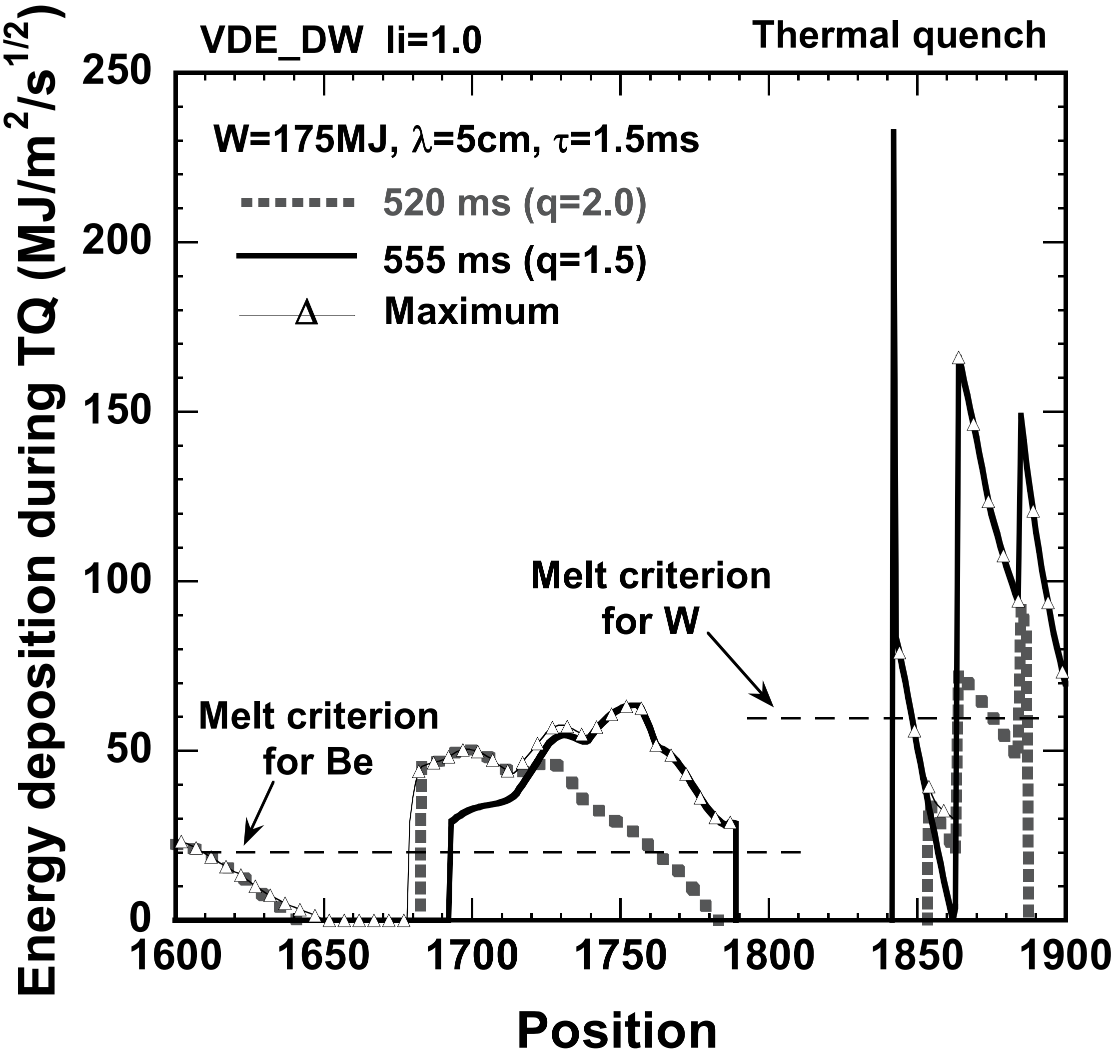

Figure 3.41

ε during the TQ at each wall position at two occurrence times of the TQ, i.e., *520 ms* (dotted line) and *555 ms* (solid line) for the downward VDE with $l_i = 1.0$. It is assumed that *175MJ* is released during the TQ with an energy deposition width of *5 cm* and a time duration of the energy deposition of *1.5 ms*. Triangles show the maximum values when the TQ occurs at an arbitrary time between *490 ms* and *555 ms*. Lower and upper dotted horizontal lines show the critical value for melting of *Be* and tungsten, respectively.

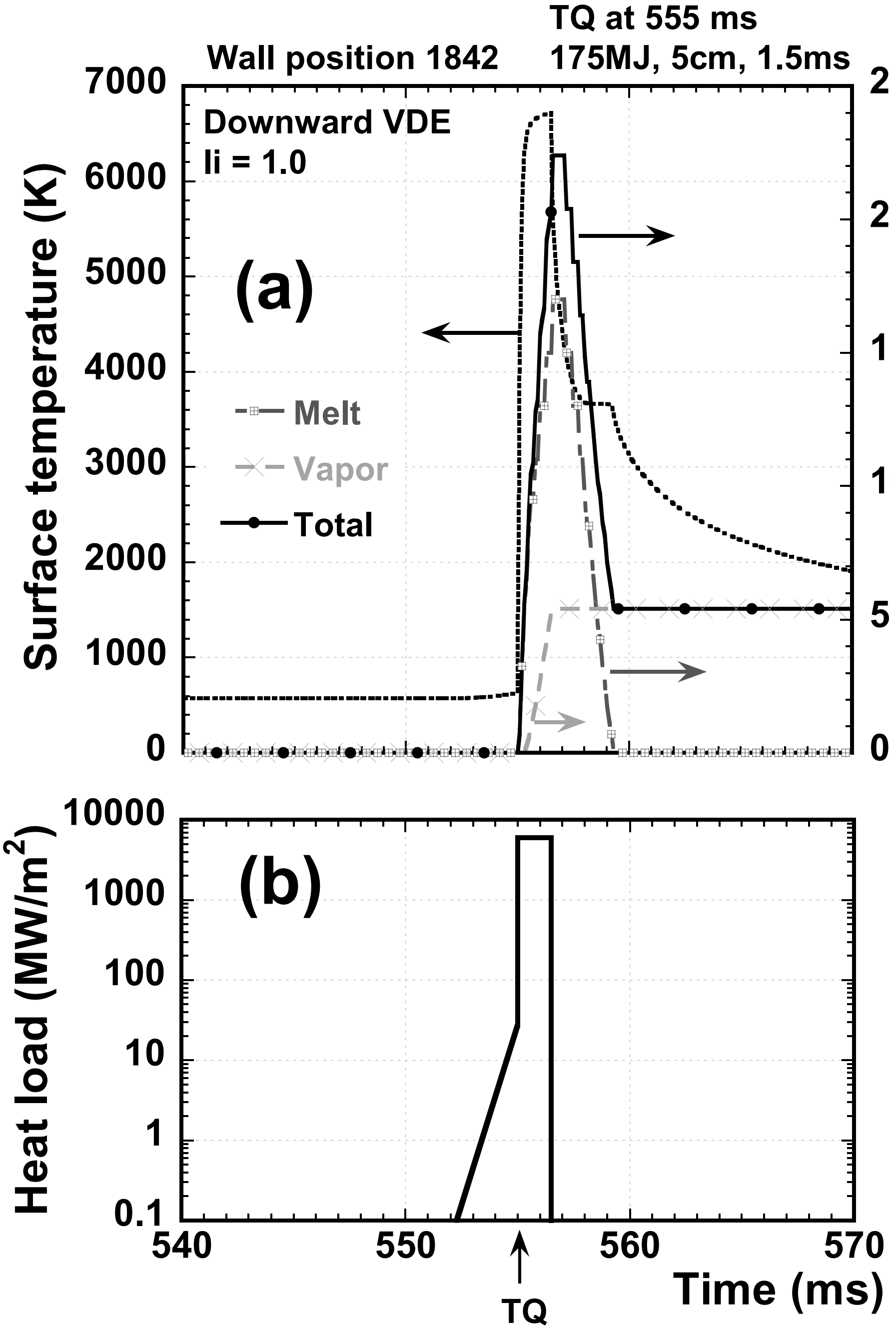

Figure 3.42 (a)
Time evolutions of the surface temperature and melting/vaporized thickness at wall position *1842* for the case of TQ occurrence time of *555 ms* for the downward VDE with $l_i = 1.0$. It is assumed that *175MJ* is released during the TQ with an energy deposition width of *5 cm* and a time duration of the energy deposition of *1.5 ms*.

Figure 3.42 (b)
Time evolutions of the heat load for the case of Fig. 3.42 (a)

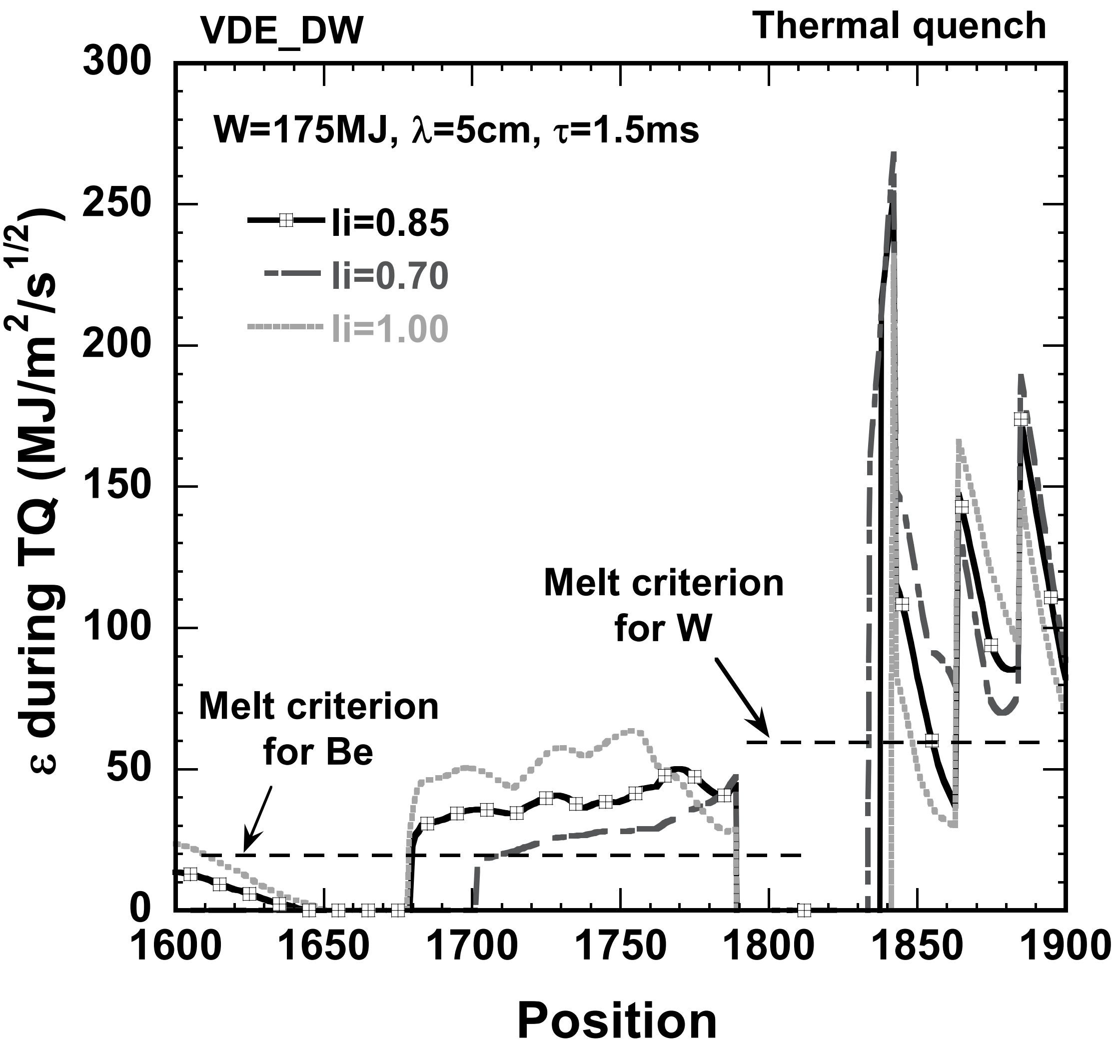

Figure 3.43
Comparison of ε during the TQ for two different internal inductances of the initial plasma, *0.7* (dashed line taken from open triangles in Fig. 3.36) and *1.0* (dotted line taken from open triangles in Fig. 3.41) with the reference case (solid line taken from open triangles in Fig. 3.31)

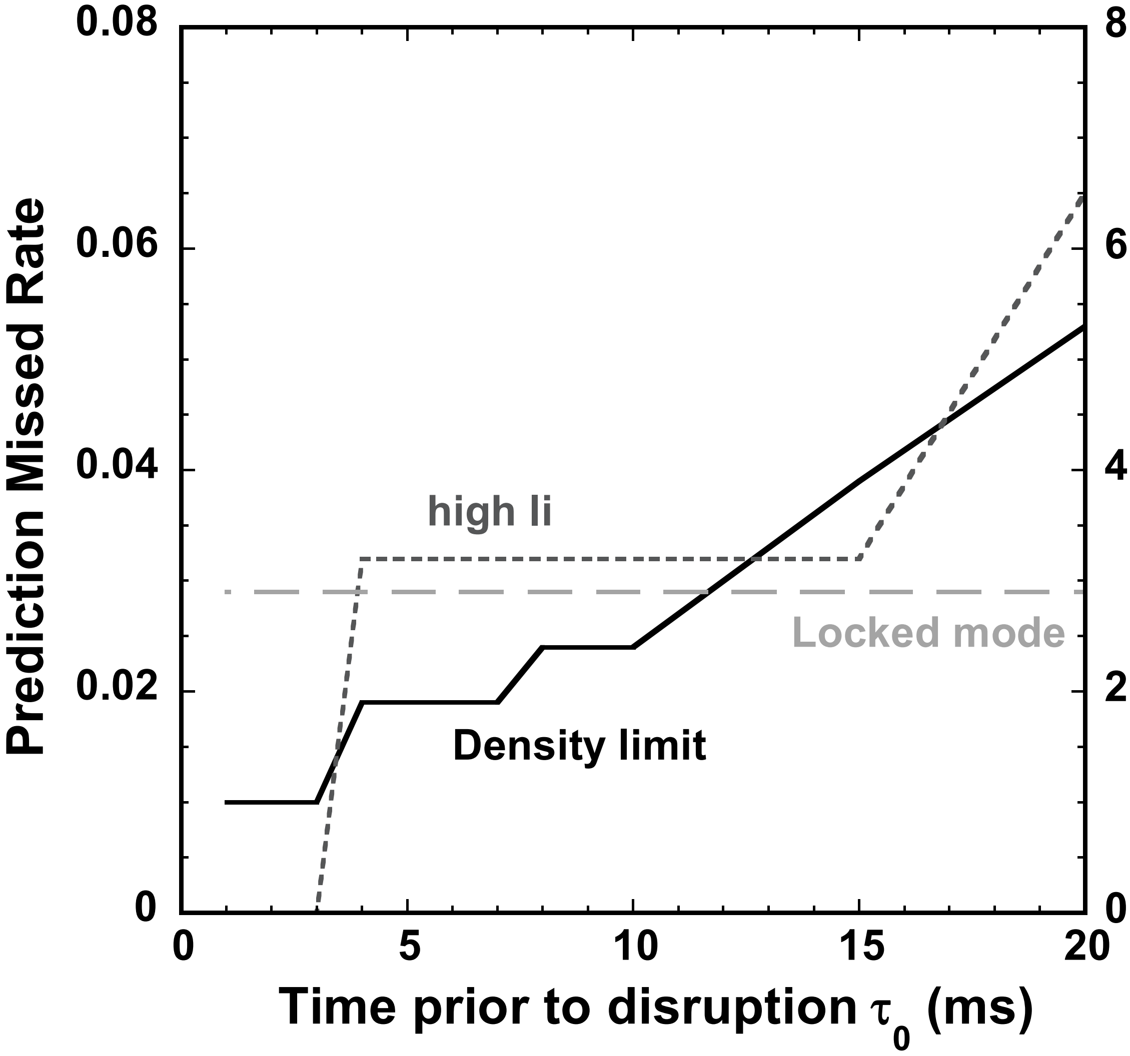

Figure 4.1
Prediction missed rate (1-success rate) as a function of the time prior to disruption τ_0 for density limit (solid line), locked mode (dashed line) and high internal inductance (dotted line) disruptions evaluated from the data provided in Ref. [22].

(a)

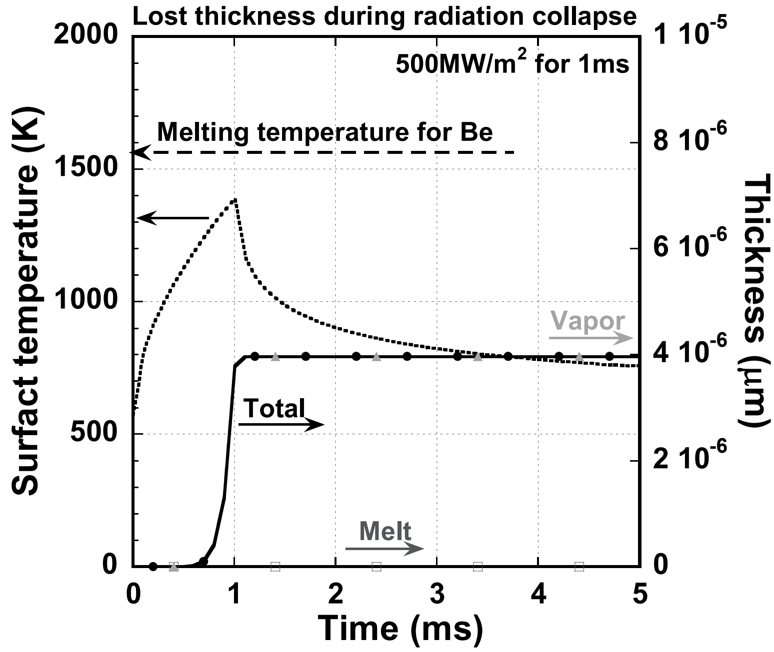

(b)

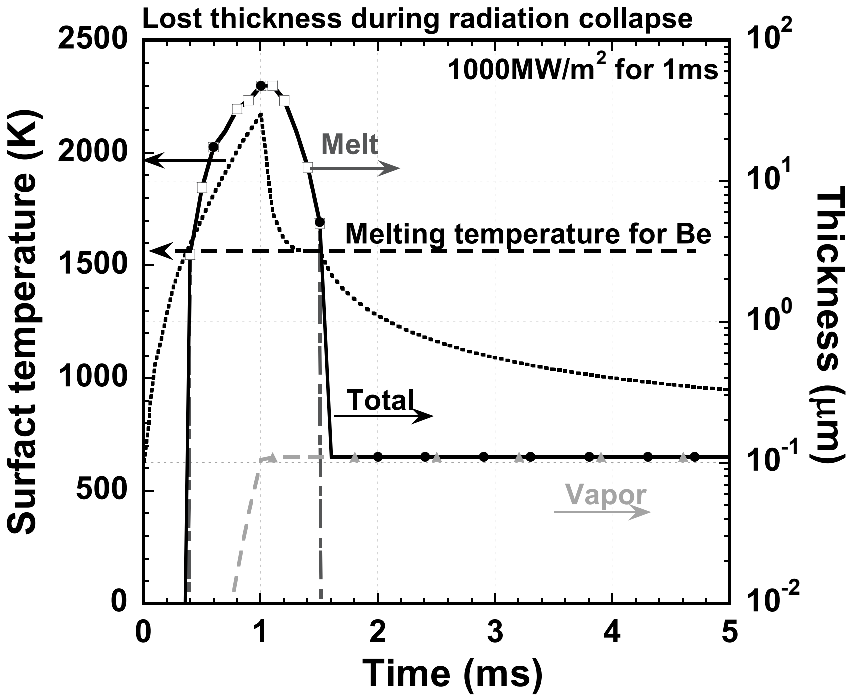

Figure 4.2
Time evolutions of the surface temperature and melting/vaporized thickness during the radiation collapse after gas injection for the cases with (a) toroidally and poloidally uniform distribution and (b) a factor of 2 peaking. Total energy released during the TQ is *350 MJ* and time duration of the radiation collapse is *1 ms*.

Appendix: Post Processing Programs

Several post processor programs have been developed to utilize the simulation results of DINA code more effectively.

1. Program for creating plasma and halo boundary to plot them by KaleidaGraph

The program to create data for plasma and halo boundary in KaleidaGraph format from simulation results of DINA code is developed.

1.1 Input files

The following files (more than at least one) must be installed under the executing directory.

a) plasma_boundary.dat
b) halo_boundary.dat
c) sol_boundary.dat
d) toroidal_currents.dat
e) poloidal_fields.dat

1.2 Execution

The following command must be typed.

"DINA_post"

1.3 Output files

The boundary data of each time moment is produced under the executing directory (e.g. "00008.00_plasma"; data of the plasma boundary at *8 ms*, "00013.10_halo"; data of the halo boundary at *13.1 ms*).

Example is shown in Figure A1, in which the plasma boundary, the halo boundary and the toroidal current distribution during the downward VDE are depicted.

2. Program for calculating PF coil current after the current termination in disruptions

Numerical code to evaluate the change of poloidal coil currents (including the induced eddy current on the vacuum vessel and blanket modules) after the plasma current termination in disruption is developed.

2.1 Input files

The following files must be installed under the executing directory.

a) f_ves.dat

b) induct_pf

c) pf_index.dat

d) ves_ind.dat

e) klim_vv_bm

f) delta_res.dat

g) fluxd, fluxde

h) psi_data

i) toroidal_currents.dat

2.2 Execution

The following command must be typed.

@eddy

Then the following message will appear on the screen:

```
=================================================
  enter I_cntl
    =1 : calculation of Ivv & Ipf (Ip=0 --> noEDDY)
    =3 : calculation of Ivv & Ipf (T.Q. --> Ip=0MA)
=================================================
```

• I_cntl=1:

Induced eddy current on the surrounding structures (specified in the input file of the DINA “klim_vv_bm”) and PF coils are calculated.

The following message will appear on the screen:

```
==============================
 ENTER time_step and delta_time
  * time_tot      : number of cal.step
                        < 0 :    till Ivv < 0.0 kA
  * delta_time : time step
                        < 0 :    =1ms
==============================
```

time_tot: Specify the total step of calculation. If this is specified below 0, calculation continues to the time point, at which the total induced current on the surrounding structures becomes 0.

delta_time: Specify the time step for calculation of current. If this is specified below 0, time step is automatically set to 1 ms.

• I_cntl=3: For check

Trace the induced currents on PF coils and surrounding structures calculated with the DINA code. Trace is performed from the onset of the thermal quench to the end of the DINA calculation. Induced eddy currents on the surrounding structures are calculated by the circuit equations using the currents on the structures and PF coils just before the thermal quench.

2.3 Output files

The following file is created. Calculation results with the DINA code are used for the induced currents from the initial plasma condition to the end of the DINA calculation.

a) @eddy.dat

- Time (ms): Time at calculation
- tpl (kA): Plasma current (this value is calculated from the output file "toroidal_currents.dat", and thus, some difference will appear from the value in "plasma.dat")
- Ivv_tot (kA): Total induced currents in the surrounding structure
- CS3U−PF6 (kA): Currents on each PF coils
- V001−V*** (kA): Currents on each surrounding structure（Corresponding to #1PS - #152PS in Figure A2）

As an example, time evolutions of the eddy currents induced on the PF coil system and the in-vessel structures after the plasma current termination have been calculated for the downward VDE for the linear quench waveform with *36 ms* current quench time.

Figure A3 shows time evolutions of the plasma current, the vertical position and the poloidal halo current. Figure A4 shows time evolutions of plasma current and the total induced current on the surrounding structures. Figures A5 and A6 show current patterns of CS and PF coils until the induced currents become zero.

3. Program for smoothing the "halo.dat" file

Numerical code to smooth the value of halo currents in “halo.dat”, which is the result of DINA calculation, is developed.

3.1 Input files

The following file must be installed under the executing directory.

a) halo.dat

3.2 Execution

The following command must be typed.

@halo_smooth

3.3 Output files

The following files are created.

a) halo.dat_smooth: “halo.dat” file after smoothing (a format same as “halo.dat” file)

b) halo.dat_each_flux

- Time (ms): Time at calculation
- halo_smooth (kA): Total poloidal halo current after smoothing
- c1_sm (kA): Halo current in the #1 (*1) flux tube after smoothing
  - : :
- c10_sm (kA): Halo current in the #10 (*1) flux tube after smoothing
- halo_org (kA): Total poloidal halo current before smoothing
- c1 (kA): Halo current in the #1 (*1) flux tube before smoothing
  - : :
- c10 (kA): Halo current in the #10 (*1) flux tube before smoothing

(*1) #1-#10 denote the ordering number of the magnetic flux tube between plasma boundary and halo boundary when it is divided into *10* flux tubes (#1 represents inner-most tube and #10 outer–most tube). Example for the magnetic flux tube is shown in Figure A7.

4. Program for creating data of halo currents on each in-vessel component

The program to create data for the poloidal halo currents flowing in and out from each in-vessel component (blanket module and divertor) as a function of time is developed. The module names used in this program are shown in Figure A8.

4.1 Input files

The following files must be installed under the executing directory.

a) halo.dat

b) psi_data

c) module_no.dat

4.2 Execution

The following command must be typed.

@dina_halo

Then the following message will appear on the screen:

```
==================================================
  enter time [ms]
    =-999 : read all time data
==================================================
```

Specify the time step for calculation. If you specify "-999", the calculation is performed all time.

4.3 Output files

The following files are created.

a) @halo.info_time

- Time (ms): Time at calculation
- ihalo(DINA) (kA): Total halo current calculated by DINA code
- ihalo (kA): Total halo current calculated by this program
- Module#1(cw) (kA): Halo current flowing into module name #1 (CW side)

  : :

- Module#1(ccw) (kA): Halo current flowing into module name #1 (CCW side)

  : :

b) @halo.dens_time

- Time (ms): Time at calculation
- ih_tot (kA): Total halo current calculated by DINA code
- d10-d01 (kA/m^2): Halo current density at the magnetic flux tube from #10 to #1 (see Fig. A7)

Example for time evolutions of the poloidal halo current flowing into each in-vessel component is shown in Figure A9. In Figure A10, example for time evolutions of the poloidal halo current density on the in-vessel module is shown.

5. Program for calculating the heat load on the first wall

The program to calculate the heat load on various parts of the blanket modules and divertor both during the vertical movement in VDEs and during beta drop in the TQ is developed. By using this result, erosion thickness (melting/vapor) of each PFC (Plasma Facing Component) can be calculated with a 2D heat conduction code (DREAM code [42]).

5.1 Input files

The following files must be installed under the executing directory.

a) plasma.dat

b) psi_data

5.2 Execution

The following command must be typed.

@heat

Then the following message will appear on the screen:

```
**********************************************
  enter LAMDA (def. 2.0 cm)
    LOAD = exp (-x/LAMDA)
              ----------------------------------------------------------------
              Specify the heat load width during vertical movement
              and thermal quench.
**********************************************
  enter heat (Q) from plasma (MW)
              --------------------------------------------------------------
              Specify the heat flow across the LCFS (Last Closed
              Flux Surface) at the L- mode.
**********************************************
  enter time data [ms]
   = time : Appoint the time from L-mode to T.Q.
   = -999 : All time is calculated.
```

Specify the time step for calculation.

5.3 Output files

The following files are created.

a) @heat.est_no: Heat load (MW/m^2) at each wall position

b) @heat.est_time1: Time evolution of the heat load (MW/m^2) on the wall position: 1-500

c) @heat.est_time2: Time evolution of the heat load (MW/m^2) on the wall position: 501-1450

d) @heat.est_time3: Time evolution of the heat load (MW/m^2) on the wall position: 1451-final

e) @heat.est_time1_inte: Time evolution of the energy deposition density divided by square root of deposition duration time: ε ($MJ/m^2/s^{1/2}$) on the wall position: 1-500

f) @heat.est_time2_inte: Time evolution of ε on the wall position: 501-1450

g) @heat.est_time3_inte: Time evolution of ε on the wall position: 1451-final

h) @heat.est_q_max: Maximum value of ε on each wall position

b) – d) can also be used to evaluate the ε during the thermal quench on each wall position. For this purpose, $Q=W_{peak}/\tau$ (W_{peak}: energy loss through separatrix, τ: time duration of the TQ). LAMDA must also be specified to the appropriate value during the TQ (*5-10 cm*). When the calculated results are multiplied with $\sqrt{\tau}$, ε can be obtained.

6. Program for calculating the vertical force on Vacuum Vessel

The program to calculate the time evolutions of the vertical force on the VV due to halo and eddy currents (induced eddy current on the VV also contributes to the vertical force of the VV to some extent) is developed.

6.1 Input files

The following files must be installed under the executing directory.

a) toroidal_currents.dat

b) psi_data

c) halo.dat

6.2 Execution

The following command must be typed.

@vv_fv

6.3 Output files

The following file is created.

a) @vv_fv.dat

- Time (ms): Time at calculation
- FV_by_eddy (N): Vertical force on the VV due to eddy current
- FV_by_halo (N): Vertical force on the VV due to halo current
- Total_FV (N): Total vertical force on the VV

Example for the time evolutions of the vertical forces due to halo and eddy currents as well as the total force is shown in Figure A11.

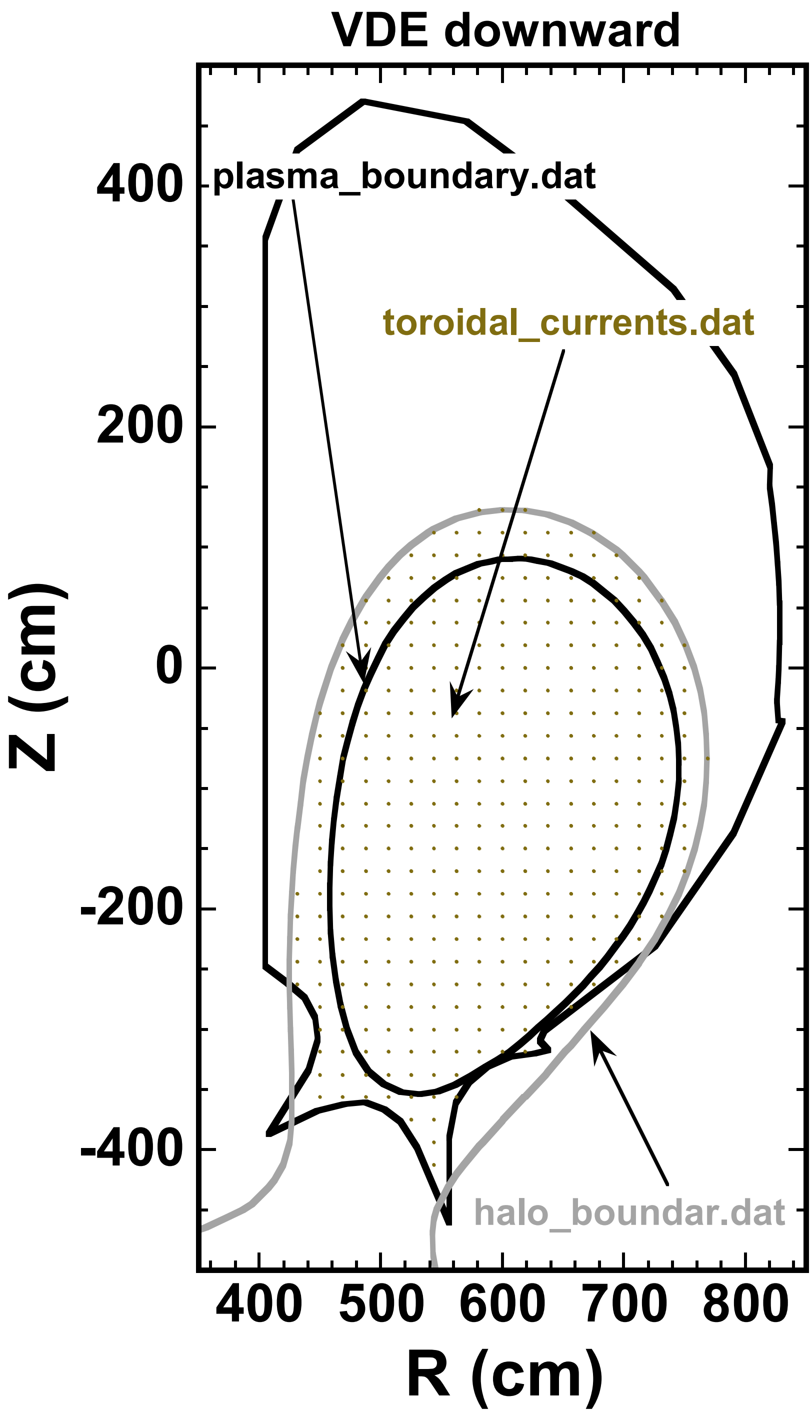

Figure A1
Plasma boundary, halo boundary and toroidal current distribution for the downward VDE created by "@DINA_post" code

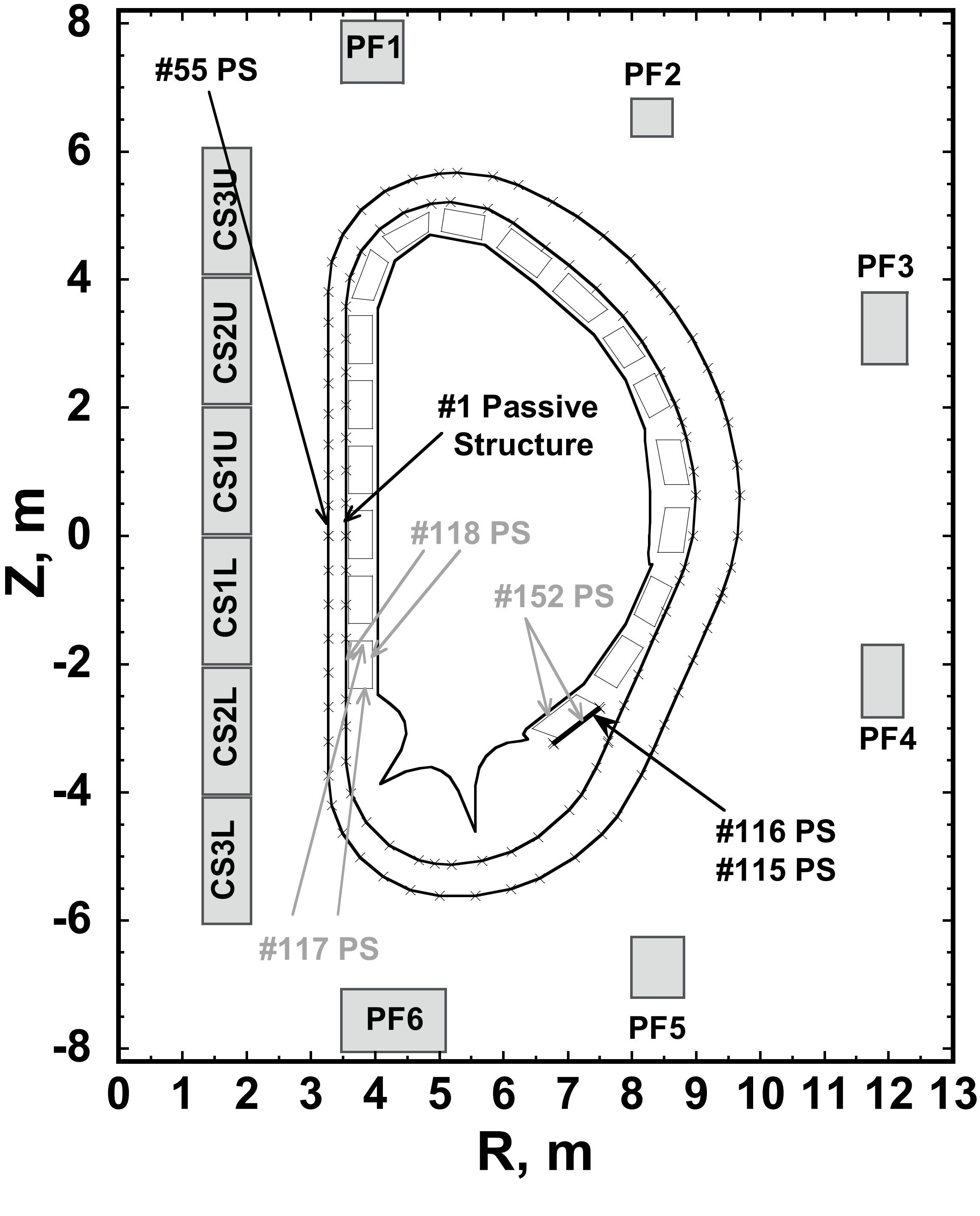

Figure A2
PF coils and surrounding structures used in the DINA code

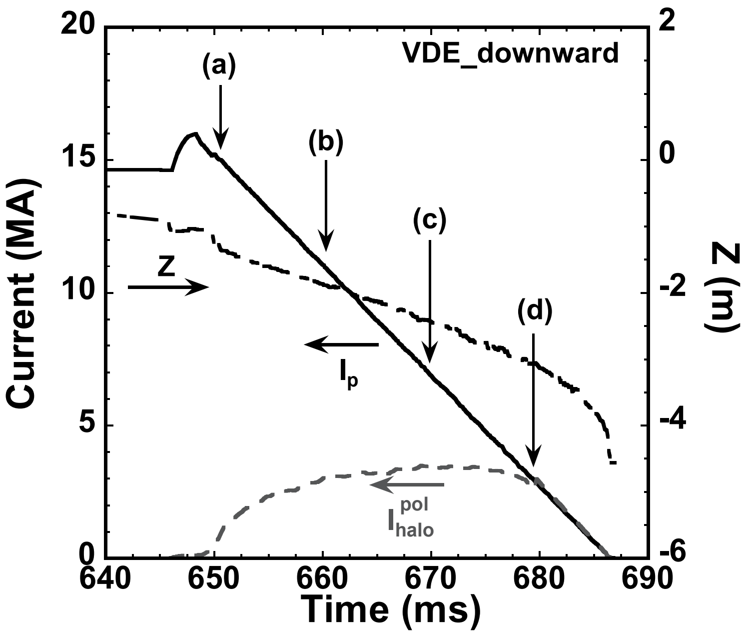

Figure A3
Time evolutions of the plasma current, the vertical position and the poloidal halo current for downward VDE for the linear quench waveform with *36 ms* current quench time simulated with the DINA code

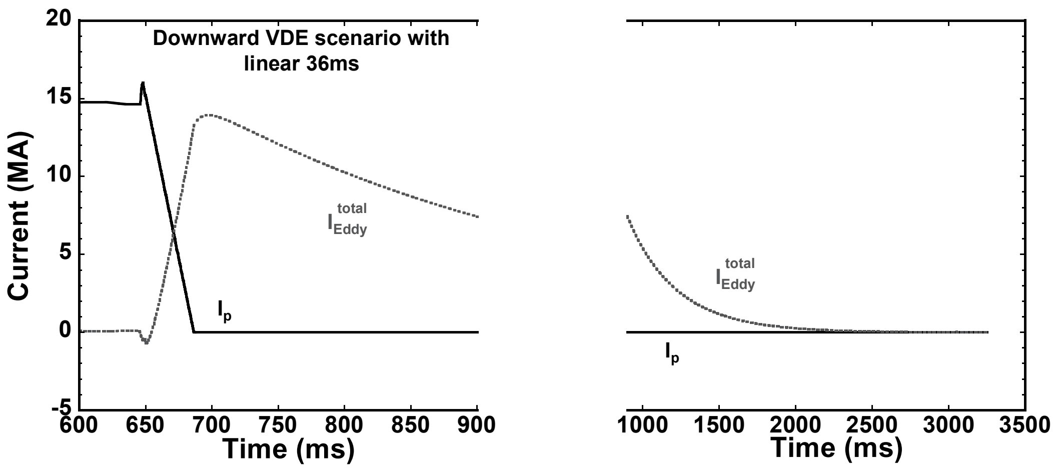

Figure A4
Time evolutions of the plasma current and the total induced current on the surrounding structures in the case of downward VDE (until total induced current becomes zero) obtained by "@eddy" code

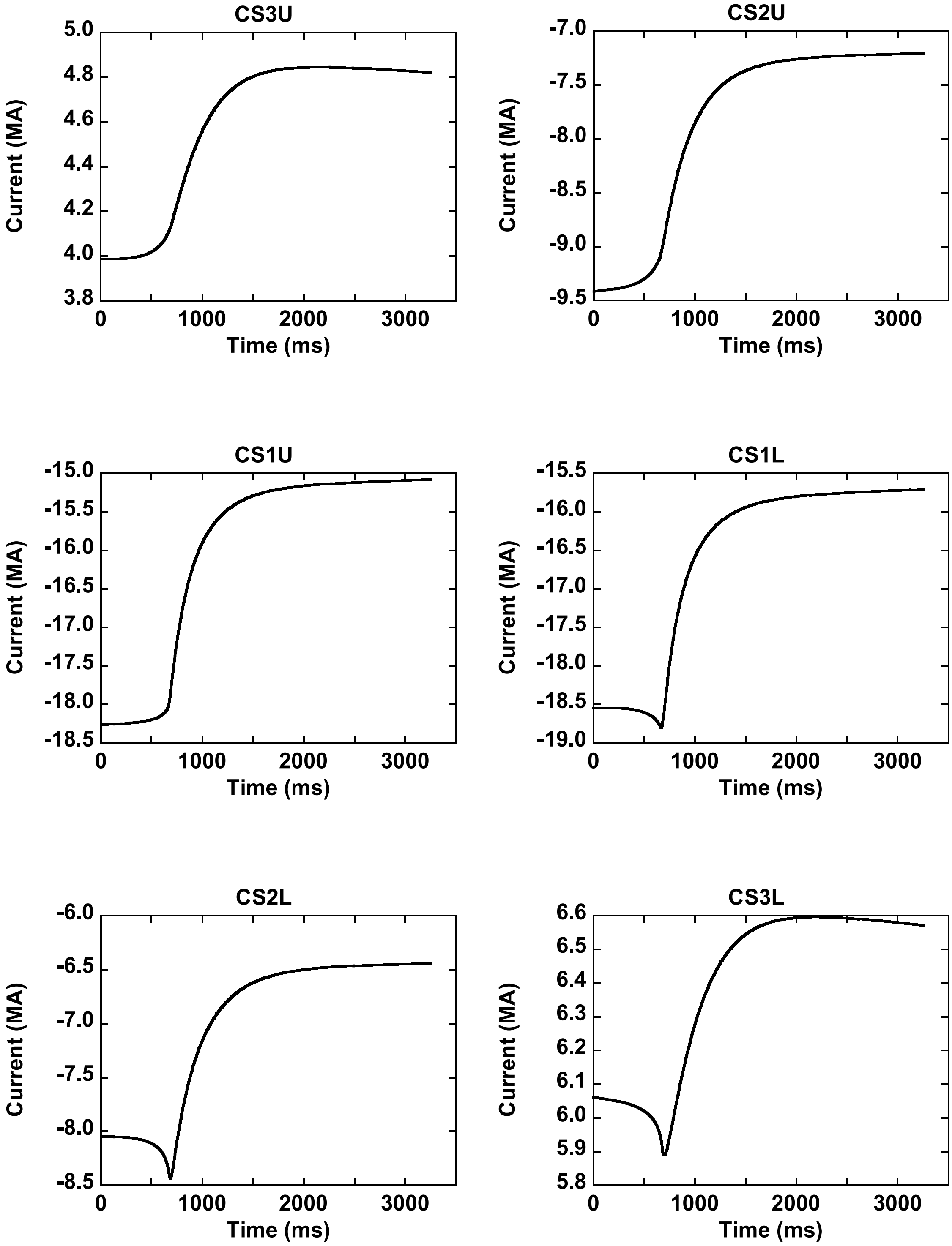

Figure A5
Current patterns of CS coils (CS3U, CS2U, CS1U, CS1L, CS2L and CS3L) until the induced currents become zero in the case of downward VDE obtained by "@eddy" code

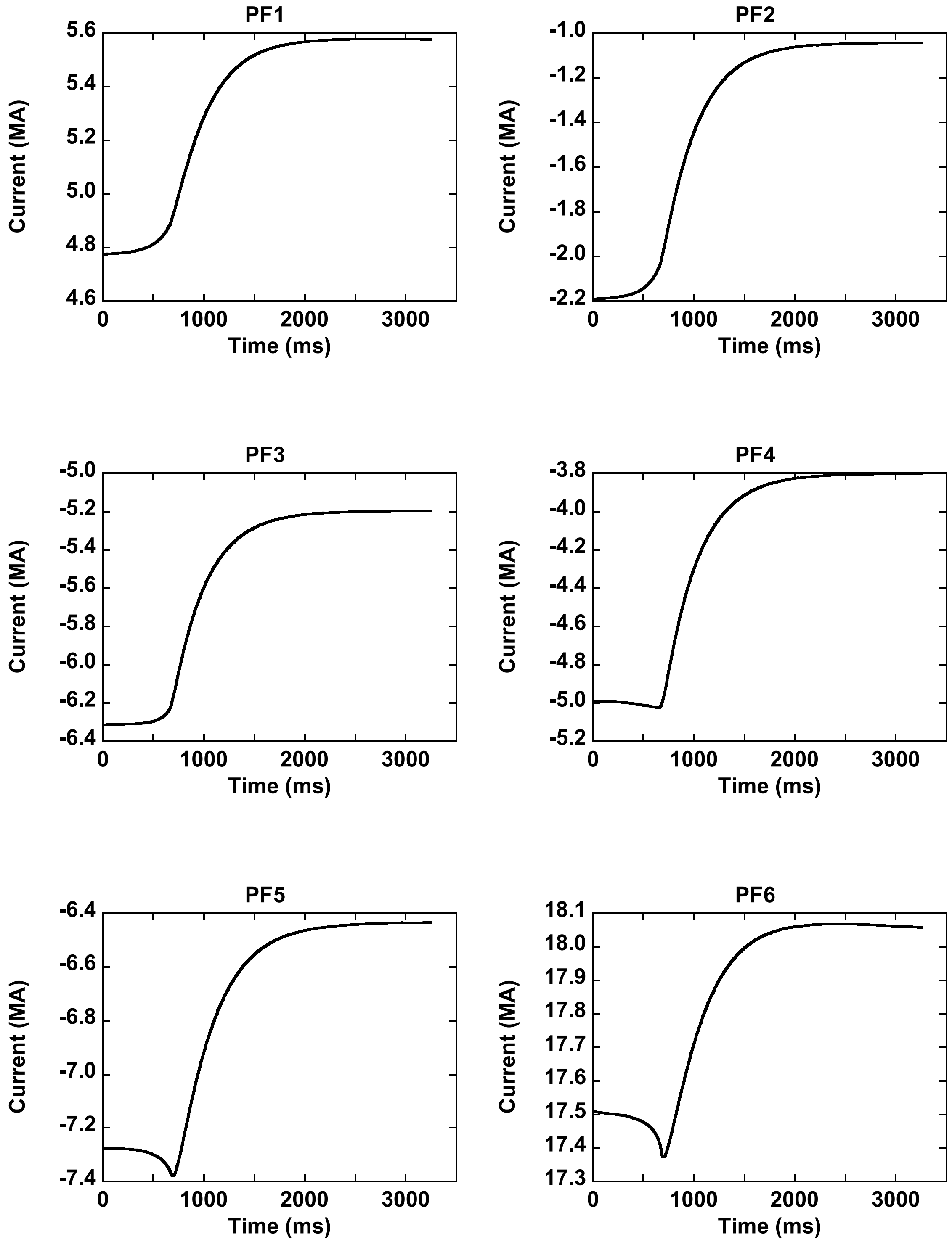

Figure A6
Current patterns of PF coils (PF1-PF6) until the induced currents become zero in the case of downward VDE obtained by "@eddy" code

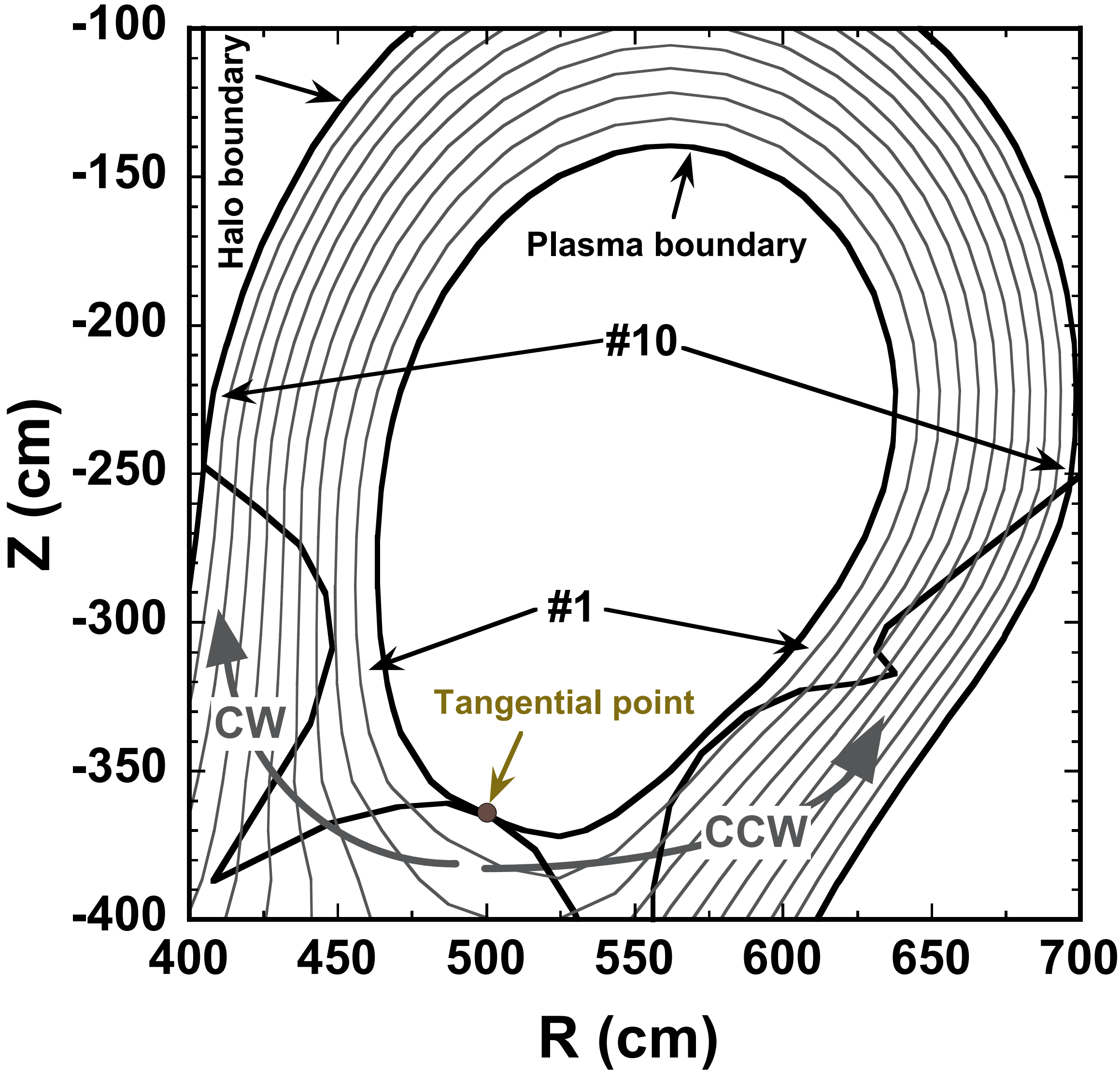

Figure A7
Example for the magnetic flux tube between plasma boundary and halo boundary when it is divided into 10 flux tubes

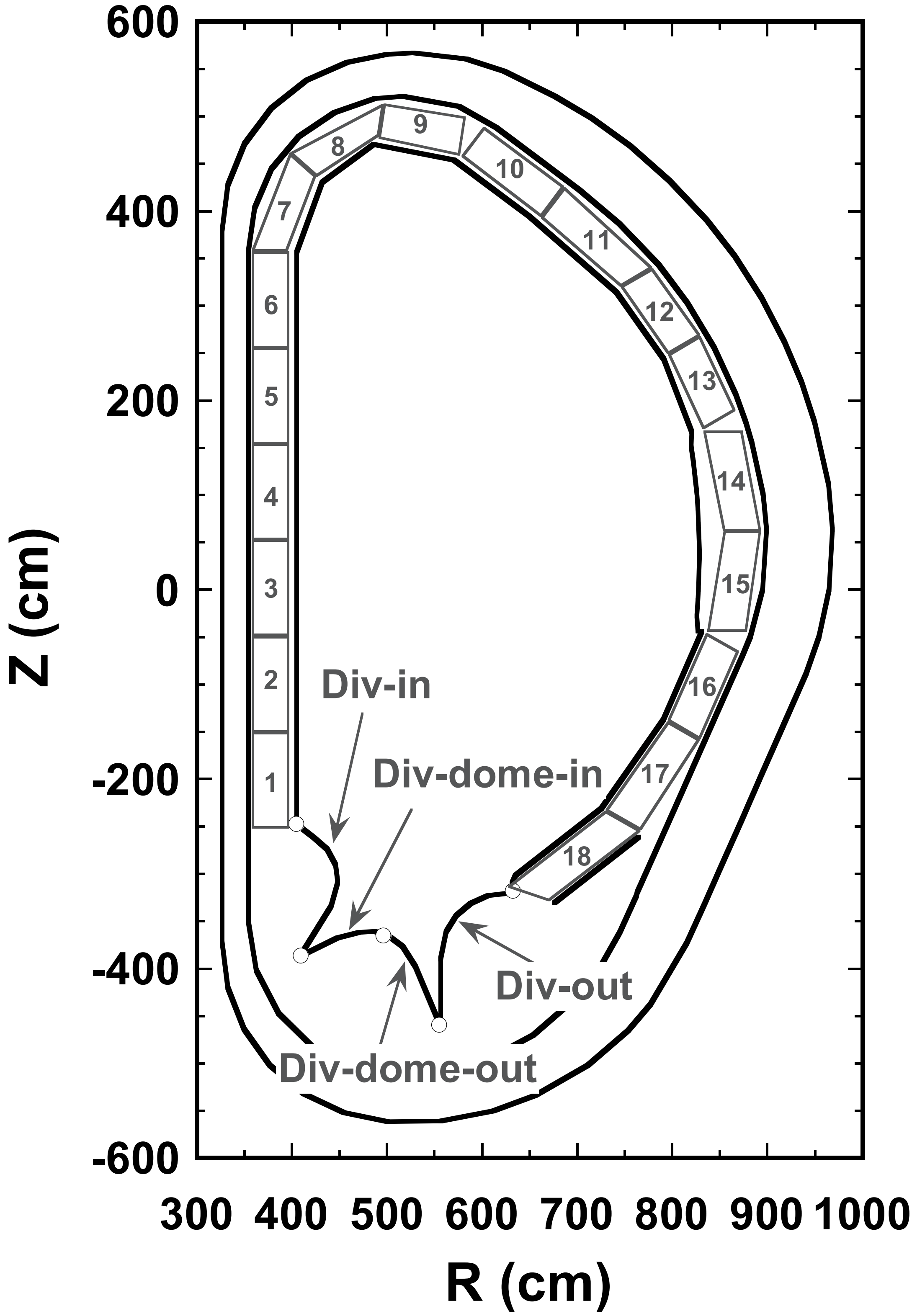

Figure A8
Module names of in-vessel components used in “@DINA_halo” code

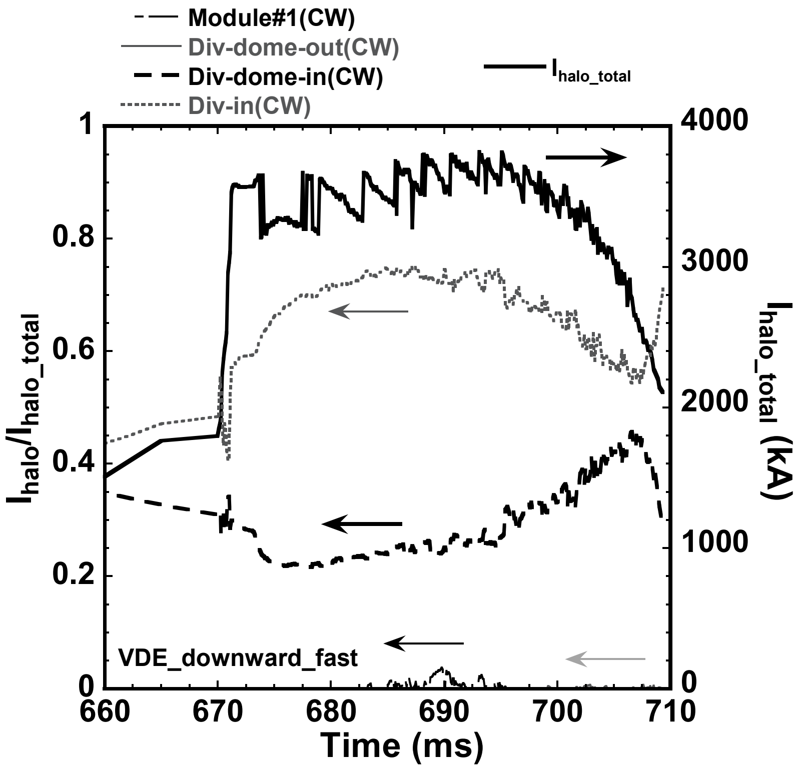

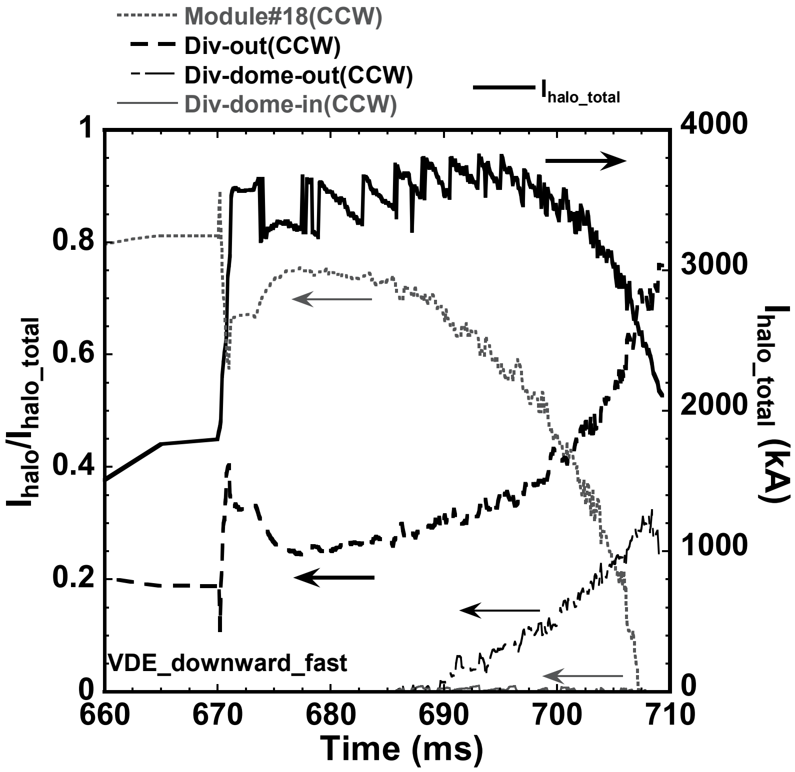

Figure A9
Time evolutions of the poloidal halo current flowing into each in-vessel component in CW (top) and CCW (bottom) directions from tangential point obtained by "@DINA_halo" code

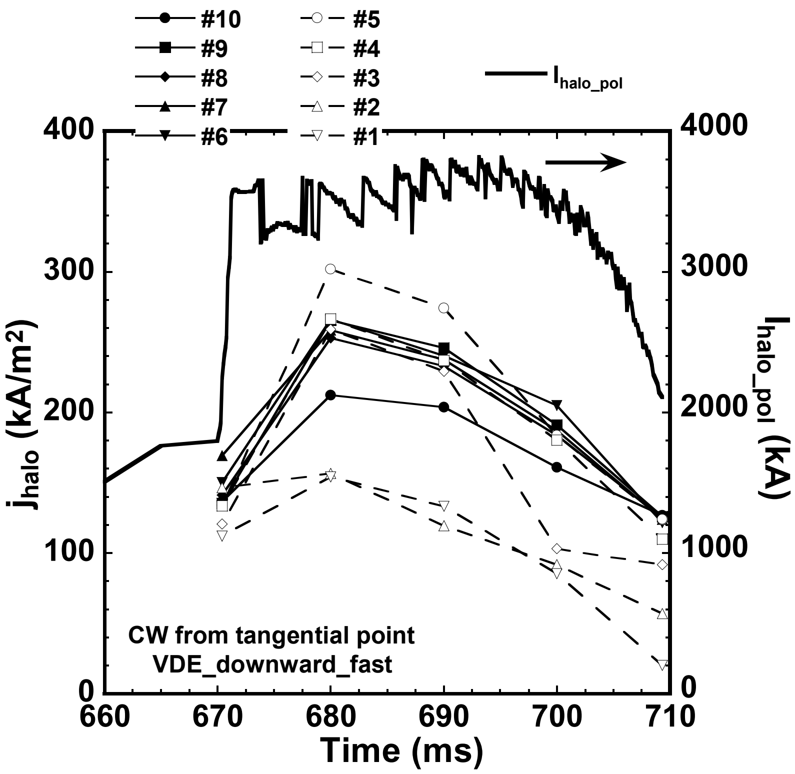

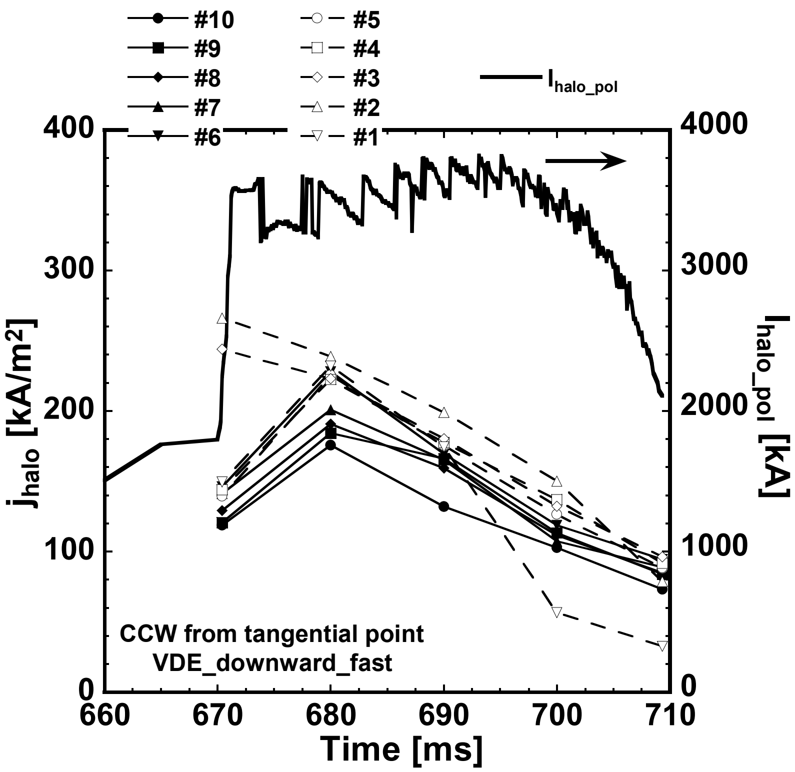

Figure A10
Time evolutions of the poloidal halo current density on the in-vessel component in CW (top) and CCW (bottom) directions from tangential point obtained by "@DINA_halo" code

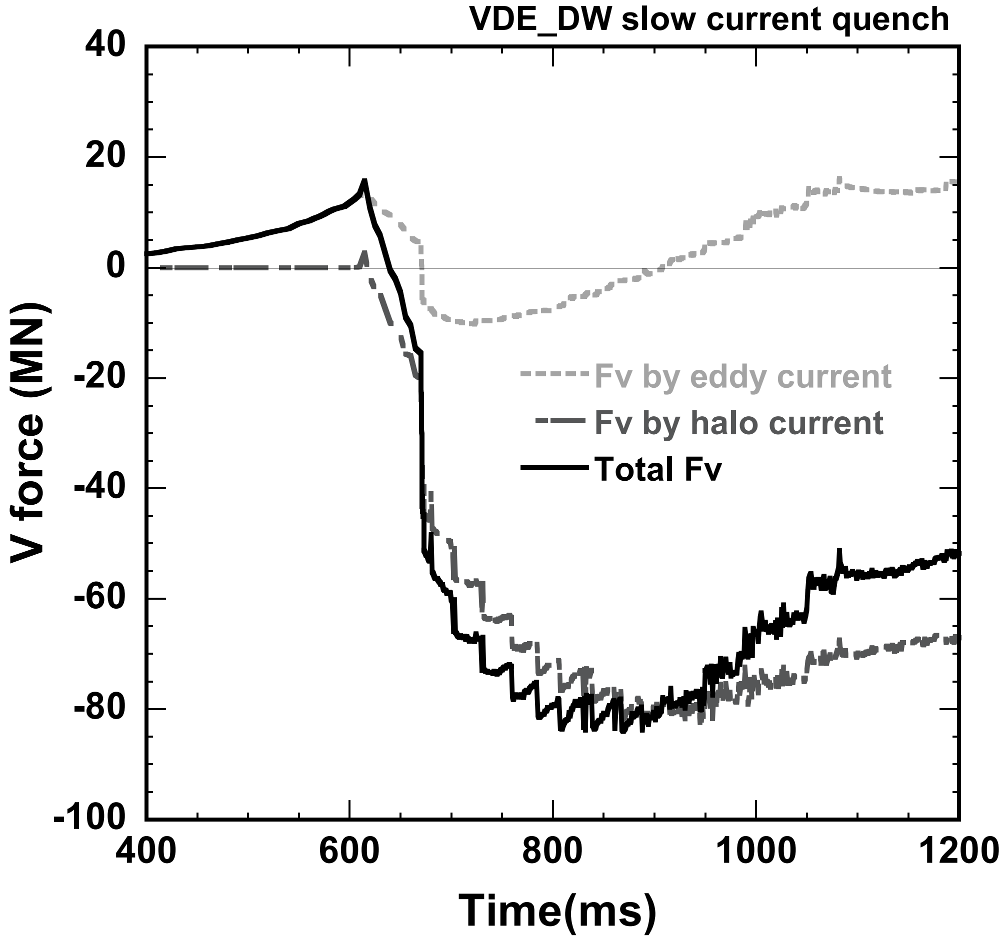

Figure A11
Time evolutions of the vertical forces on the VV due to halo (dashed line) and eddy (dotted line) currents as well as the total force (solid line) for the case of downward VDE obtained by "@vv_fv" code

国際単位系（SI）

表１．SI 基本単位

基本量	SI 基本単位	
	名称	記号
長さ	メートル	m
質量	キログラム	kg
時間	秒	s
電流	アンペア	A
熱力学温度	ケルビン	K
物質量	モル	mol
光度	カンデラ	cd

表２．基本単位を用いて表されるSI組立単位の例

組立量	SI 基本単位	
	名称	記号
面積	平方メートル	m^2
体積	立法メートル	m^3
速さ，速度	メートル毎秒	m/s
加速度	メートル毎秒毎秒	m/s^2
波数	毎メートル	m-1
密度（質量密度）	キログラム毎立法メートル	kg/m^3
質量体積（比体積）	立法メートル毎キログラム	m^3/kg
電流密度	アンペア毎平方メートル	A/m^2
磁界の強さ	アンペア毎メートル	A/m
（物質量の）濃度	モル毎立方メートル	mol/m^3
輝度	カンデラ毎平方メートル	cd/m^2
屈折率	（数の）１	1

表５．SI 接頭語

乗数	接頭語	記号	乗数	接頭語	記号
10^{24}	ヨタ	Y	10^{-1}	デシ	d
10^{21}	ゼタ	Z	10^{-2}	センチ	c
10^{18}	エクサ	E	10^{-3}	ミリ	m
10^{15}	ペタ	P	10^{-6}	マイクロ	μ
10^{12}	テラ	T	10^{-9}	ナノ	n
10^{9}	ギガ	G	10^{-12}	ピコ	p
10^{6}	メガ	M	10^{-15}	フェムト	f
10^{3}	キロ	k	10^{-18}	アト	a
10^{2}	ヘクト	h	10^{-21}	ゼプト	z
10^{1}	デカ	da	10^{-24}	ヨクト	y

表３．固有の名称とその独自の記号で表されるSI組立単位

組立量	SI 組立単位			
	名称	記号	他のSI単位による表し方	SI基本単位による表し方
平面角	ラジアン (a)	rad		$m \cdot m^{-1}=1$ (b)
立体角	ステラジアン (a)	sr (c)		$m^2 \cdot m^{-2}=1$ (b)
周波数	ヘルツ	Hz		s^{-1}
力	ニュートン	N		$m \cdot kg \cdot s^{-2}$
圧力，応力	パスカル	Pa	N/m^2	$m^{-1} \cdot kg \cdot s^{-2}$
エネルギー，仕事，熱量	ジュール	J	N・m	$m^2 \cdot kg \cdot s^{-2}$
工率，放射束	ワット	W	J/s	$m^2 \cdot kg \cdot s^{-3}$
電荷，電気量	クーロン	C		s・A
電位差（電圧），起電力	ボルト	V	W/A	$m^2 \cdot kg \cdot s^{-3} \cdot A^{-1}$
静電容量	ファラド	F	C/V	$m^{-2} \cdot kg^{-1} \cdot s^4 \cdot A^2$
電気抵抗	オーム	Ω	V/A	$m^2 \cdot kg \cdot s^{-3} \cdot A^{-2}$
コンダクタンス	ジーメンス	S	A/V	$m^{-2} \cdot kg^{-1} \cdot s^3 \cdot A^2$
磁束	ウエーバ	Wb	V・s	$m^2 \cdot kg \cdot s^{-2} \cdot A^{-1}$
磁束密度	テスラ	T	Wb/m^2	$kg \cdot s^{-2} \cdot A^{-1}$
インダクタンス	ヘンリー	H	Wb/A	$m^2 \cdot kg \cdot s^{-2} \cdot A^{-2}$
セルシウス温度	セルシウス度 (d)	℃		K
光束	ルーメン	lm	cd・sr (c)	$m^2 \cdot m^{-2} \cdot cd=cd$
照度	ルクス	lx	lm/m^2	$m^2 \cdot m^{-4} \cdot cd=m^{-2} \cdot cd$
（放射性核種の）放射能	ベクレル	Bq		s^{-1}
吸収線量，質量エネルギー分与，カーマ	グレイ	Gy	J/kg	$m^2 \cdot s^{-2}$
線量当量，周辺線量当量，方向性線量当量，個人線量当量，組織線量当	シーベルト	Sv	J/kg	$m^2 \cdot s^{-2}$

(a) ラジアン及びステラジアンの使用は、同じ次元であっても異なった性質をもった量を区別するときの組立単位の表し方として利点がある。組立単位を形作るときのいくつかの用例は表４に示されている。
(b) 実際には、使用する時には記号rad及びsrが用いられるが、習慣として組立単位としての記号“１”は明示されない。
(c) 測光学では、ステラジアンの名称と記号srを単位の表し方の中にそのまま維持している。
(d) この単位は、例としてミリセルシウス度m℃のようにSI接頭語を伴って用いても良い。

表４．単位の中に固有の名称とその独自の記号を含むSI組立単位の例

組立量	SI 組立単位		
	名称	記号	SI 基本単位による表し方
粘度	パスカル秒	Pa・s	$m^{-1} \cdot kg \cdot s^{-1}$
力のモーメント	ニュートンメートル	N・m	$m^2 \cdot kg \cdot s^{-2}$
表面張力	ニュートン毎メートル	N/m	$kg \cdot s^{-2}$
角速度	ラジアン毎秒	rad/s	$m \cdot m^{-1} \cdot s^{-1}=s^{-1}$
角加速度	ラジアン毎平方秒	rad/s^2	$m \cdot m^{-1} \cdot s^{-2}=s^{-2}$
熱流密度，放射照度	ワット毎平方メートル	W/m^2	$kg \cdot s^{-3}$
熱容量，エントロピー	ジュール毎ケルビン	J/K	$m^2 \cdot kg \cdot s^{-2} \cdot K^{-1}$
質量熱容量（比熱容量），質量エントロピー	ジュール毎キログラム毎ケルビン	J/(kg・K)	$m^2 \cdot s^{-2} \cdot K^{-1}$
質量エネルギー（比エネルギー）	ジュール毎キログラム	J/kg	$m^2 \cdot s^{-2} \cdot K^{-1}$
熱伝導率	ワット毎メートル毎ケルビン	W/(m・K)	$m \cdot kg \cdot s^{-3} \cdot K^{-1}$
体積エネルギー	ジュール毎立方メートル	J/m^3	$m^{-1} \cdot kg \cdot s^{-2}$
電界の強さ	ボルト毎メートル	V/m	$m \cdot kg \cdot s^{-3} \cdot A^{-1}$
体積電荷	クーロン毎立方メートル	C/m^3	$m^{-3} \cdot s \cdot A$
電気変位	クーロン毎平方メートル	C/m^2	$m^{-2} \cdot s \cdot A$
誘電率	ファラド毎メートル	F/m	$m^{-3} \cdot kg^{-1} \cdot s^4 \cdot A^2$
透磁率	ヘンリー毎メートル	H/m	$m \cdot kg \cdot s^{-2} \cdot A^{-2}$
モルエネルギー	ジュール毎モル	J/mol	$m^2 \cdot kg \cdot s^{-2} \cdot mol^{-1}$
モルエントロピー，モル熱容量	ジュール毎モル毎ケルビン	J/(mol・K)	$m^2 \cdot kg \cdot s^{-2} \cdot K^{-1} \cdot mol^{-1}$
照射線量（Ｘ線及びγ線）	クーロン毎キログラム	C/kg	$kg^{-1} \cdot s \cdot A$
吸収線量率	グレイ毎秒	Gy/s	$m^2 \cdot s^{-3}$
放射強度	ワット毎ステラジアン	W/sr	$m^4 \cdot m^{-2} \cdot kg \cdot s^{-3}=m^2 \cdot kg \cdot s^{-3}$
放射輝度	ワット毎平方メートル毎ステラジアン	$W/(m^2 \cdot sr)$	$m^2 \cdot m^{-2} \cdot kg \cdot s^{-3}=kg \cdot s^{-3}$

表６．国際単位系と併用されるが国際単位系に属さない単位

名称	記号	SI 単位による値
分	min	1 min=60s
時	h	1h =60 min=3600 s
日	d	1 d=24 h=86400 s
度	°	1° =(π/180) rad
分	’	1’ =(1/60)° =(π/10800) rad
秒	”	1” =(1/60)’ =(π/648000) rad
リットル	l、L	$1l=1\ dm^3=10^{-3}m^3$
トン	t	$1t=10^3$ kg
ネーパ	Np	1Np=1
ベル	B	1B=(1/2)ln10(Np)

表７．国際単位系と併用されこれに属さない単位でSI単位で表される数値が実験的に得られるもの

名称	記号	SI 単位であらわされる数値
電子ボルト	eV	$1eV=1.60217733(49)\times10^{-19}J$
統一原子質量単位	u	$1u=1.6605402(10)\times10^{-27}kg$
天文単位	ua	$1ua=1.49597870691(30)\times10^{11}m$

表８．国際単位系に属さないが国際単位系と併用されるその他の単位

名称	記号	SI 単位であらわされる数値
海里		1海里=1852m
ノット		1ノット=1海里毎時=(1852/3600)m/s
アール	a	$1\ a=1\ dam^2=10^2m^2$
ヘクタール	ha	$1\ ha=1\ hm^2=10^4m^2$
バール	bar	$1\ bar=0.1MPa=100kPa=1000hPa=10^5Pa$
オングストローム	Å	1 Å$=0.1nm=10^{-10}m$
バーン	b	$1\ b=100fm^2=10^{-28}m^2$

表９．固有の名称を含むCGS組立単位

名称	記号	SI 単位であらわされる数値
エルグ	erg	$1\ erg=10^{-7}$ J
ダイン	dyn	$1\ dyn=10^{-5}N$
ポアズ	P	$1\ P=1\ dyn \cdot s/cm^2=0.1Pa \cdot s$
ストークス	St	$1\ St=1cm^2/s=10^{-4}m^2/s$
ガウス	G	1 G ˆ10^{-4}T
エルステッド	Oe	1 Oe ˆ(1000/4π)A/m
マクスウェル	Mx	1 Mx ˆ10^{-8}Wb
スチルブ	sb	$1\ sb=1cd/cm^2=10^4cd/m^2$
ホト	ph	$1\ ph=10^4lx$
ガル	Gal	$1\ Gal=1cm/s^2=10^{-2}m/s^2$

表10．国際単位に属さないその他の単位の例

名称	記号	SI 単位であらわされる数値
キュリー	Ci	$1\ Ci=3.7\times10^{10}Bq$
レントゲン	R	$1\ R = 2.58\times10^{-4}C/kg$
ラド	rad	$1\ rad=1cGy=10^{-2}Gy$
レム	rem	$1\ rem=1\ cSv=10^{-2}Sv$
X線単位		$1X\ unit=1.002\times10^{-4}nm$
ガンマ	γ	$1\gamma=1\ nT=10^{-9}T$
ジャンスキー	Jy	$1\ Jy=10^{-26}W \cdot m^{-2} \cdot Hz^{-1}$
フェルミ		$1\ fermi=1\ fm=10^{-15}m$
メートル系カラット		$1\ metric\ carat = 200\ mg = 2\times10^{-4}kg$
トル	Torr	1 Torr = (101 325/760) Pa
標準大気圧	atm	1 atm = 101 325 Pa
カロリー	cal	
ミクロン	μ	$1\ \mu=1\mu m=10^{-6}m$

（第７版，1998年改訂）

R100

古紙配合率100%
白色度70%再生紙を使用しています。